

Department of Physics and Astronomy

Heidelberg University

Master thesis

in Physics

submitted by

B.Sc. Ruben Kolb

born in Ludwigshafen

2023

**Disentangling the Diffusive Part of the
Drift-Dominated Signal Generation in a
High-Ohmic Run2021v2 HV-MAPS Prototype**

This Master thesis has been carried out by Ruben Kolb

at the

Physikalisches Institut

under the supervision of

Prof. André Schöning

Abstract:

Modern particle physics experiments have an ever-growing demand for silicon pixel detectors with more precise spatial and time resolution, combined with a high rate capability and low power consumption. These requirements drive the development of pixel detectors like the High-Voltage Monolithic Active Pixel Sensor (HV-MAPS). It combines active detector volume and readout in one entity. The Run2021v2 is an HV-MAPS prototype that includes an in-pixel CMOS amplifier and comparator.

The charge collection process in this sensor is investigated with emphasis on the contribution of diffusion to the signal generation, to improve future HV-MAPS designs. The moving charge carriers induce a voltage signal in the pixel readout electronics. The properties of this signal are studied for various sources (electrons, photons, charge injection), depending on the applied reverse bias voltage and the sensor thickness. Observed sensor-to-sensor variations necessitate the development of a calibration to allow for a precise comparison. A calibration method utilizing the 5.9 keV photon of the ^{55}Fe decay is implemented and presented. Overall, a significant increase of the collected charge of up to 50% was measured for diffusion, compared to the signal generated by drift only. For small depleted volumes an increase of collected charge of up to 50%, caused by the additional charge collection via diffusion, is measured.

Zusammenfassung:

Moderne Experimente in der Teilchenphysik benötigen immer bessere hochratenfähige Silizium-Pixeldetektoren, welche sowohl eine präzise Orts- als auch Zeitauflösung aufweisen. Diese Anforderungen treiben die Entwicklung von neuartigen Pixeldetektoren wie beispielsweise Hochspannungsgetriebene Monolithische Aktive Pixel Sensoren (HV-MAPS) voran. Diese vereinen aktives Detektormaterial und Ausleselektronik in einem Sensor. Der Run2021v2 ist ein HV-MAPS Prototyp, in dem ein CMOS Verstärker und Komparator in den Pixel integriert sind.

Der Ladungssammelungsprozess in diesem Sensor wird untersucht, wobei der Schwerpunkt auf dem Beitrag durch Diffusion liegt, um zukünftige HV-MAPS Entwürfe zu verbessern. Die bewegten Ladungsträger induzieren ein Spannungssignal in der Ausleselektronik des Pixels. Die Signal Eigenschaften werden für unterschiedliche Signal Quellen (Elektronen, Photonen, Ladungsinjektion) in Abhängigkeit von der Hochspannung untersucht. Hierbei werden Sensor zu Sensor Variationen beobachtet, welche eine Kalibration notwendig machen. Eine Kalibration, welche die ^{55}Fe Quelle nutzt, wird implementiert und vorgestellt. Für kleine Verarmungsvolumina wird eine zusätzliche Ladungssammlung von bis zu 50% mehr Ladung gemessen.

Contents

I	Introduction	1
1	Introduction	3
2	Particle Detection	5
2.1	Photons	5
2.2	Charged Particles	6
3	Semiconductor Physics	9
3.1	Semiconductors	9
3.2	Doping	10
3.3	The pn-junction Diode	10
3.4	Diffusion in Semiconductors	12
3.5	Charge Collection	12
3.6	Signal Generation	13
3.7	MOSFET	14
II	HV-CMOS Sensors	17
4	Pixel Detectors	19
4.1	Hybrid Pixel Detectors	19
4.2	Monolithic Active Pixel Sensors (MAPS)	19
4.3	HV-MAPS	19
4.4	The Run 2021 V2 Sensor	21
4.5	The Injection Circuit	24
5	Measurement Setup	27
5.1	Motherboard PCB	27
5.2	Insert PCB	28
5.3	FPGA Interface	29
5.4	DAQ	29
5.5	Test Beam Setup	29
5.6	Radioactive Sources	29
5.7	Measuring Diffusion	31
6	Data Analysis	35
6.1	Introduction to Corryvreckan	35
6.2	Corryvreckan Modules	35
III	Diffusion	37
7	Guard Ring Investigation	39
8	Cluster size and ToT	43
8.1	Cluster Size	43
8.2	ToT	47
8.3	Chip Variations	49
9	ToT Analysis	53
9.1	ToTAnalyzer	53
9.2	Calibration Method	56

9.3	^{55}Fe in the ToTAnalyzer	57
10	ToT Calibration	69
10.1	Introduction	69
10.2	Quality Control of Calibration	70
11	Calibrated Diffusion Studies	79
11.1	Test Beam	79
11.2	^{90}Sr	82
IV	Discussion	87
12	Summary & Conclusion	89
13	Outlook	93
V	Appendix	95
A	DAC Values	97
B	ToTAnalyzer Maps	98
A	Bibliography	101

I Introduction

1 Introduction

The Standard Model (SM) of particle physics describes the fundamental particles and their interactions. The SM predictions were confirmed by experiments with an astonishing precision. However, the SM can not explain many fundamental observations such as the matter-antimatter asymmetry, or the properties of dark matter. Therefore, modern particle physics experiments are steadily searching for experimental evidence of deviations from the SM. There are mainly two frontiers to find these new physics. First, there is the energy frontier: Collider experiments, with ever increasing center of mass energies have the potential of producing yet unknown heavy particles. A well known example for this kind of experiment is the ATLAS experiment at the Large Hadron Collider (LHC). Second, there is the precision frontier: Precision experiments which search for the tiniest deviation from SM processes. Such deviations could e.g. arise due to new heavy particles contributing at quantum loop level. One of these high precision experiments is the Mu3e experiment. It searches for the decay $\mu^+ \rightarrow e^+ + e^+ + e^-$ with a sensitivity of 10^{-16} , increasing the current limit set by the SINDRUM experiment by four orders of magnitude [1]. This decay violates charged lepton flavor conservation, an accidental symmetry of the SM and is therefore highly suppressed with a branching ratio in the order of 10^{-54} [2].

All these experiments have an ever-growing demand on new detector technologies which enable measurements with supreme precision. Typical requirements for these detectors are a combination of excellent spatial and time resolution. In addition, a high detector granularity is required for the application in regions of high track density. A technology which meets all these requirements is the High-Voltage Monolithic Active Pixel Sensor (HV-MAPS) technology. Here, pixel sensor and digital readout are housed in the same chip. These sensors have cheaper production costs than hybrid pixel sensors and can be produced in a commercial HV-CMOS process. By applying a reverse bias voltage to the sensor, a depletion zone is created. Within this depletion zone charge is collected via drift. The presence of an electric field allows for a time resolution in the order of a few nanoseconds. The readout circuitry then processes the collected charge and outputs a digital signal.

Within the course of this thesis the contribution of diffusion to the created signal is investigated. Depending on substrate resistivity and applied voltage, the depletion zone is approximately between 20 μm and 70 μm deep. Charge carriers which are created in the undepleted substrate move along the concentration gradient, which microscopically corresponds to a random walk. This effect is called diffusion. The velocity and also the mean free path of these charge carriers depends on the substrate resistivity. If this random movement leads to a charge carrier entering the depleted volume, the electric field will accelerate the charge carrier and it will therefore contribute to the signal. With the growing number of possible applications of the HV-CMOS process, the importance of gaining a deeper understanding of the charge collection process is rising as well.

In order to study the impact of diffusion on the signal, different sources are used to induce signals in the sensor. These are two radioactive sources, (^{55}Fe and ^{90}Sr), a 4 GeV electron beam obtained from the DESY testbeam facility and an artificial charge induced by an injection circuit. By varying the depletion depth and comparing sensors of different thickness, conclusions on the importance of diffusion to

the signal can be drawn. The sensor used for this study is manufactured in an 180 nm HV-CMOS process with an in-pixel amplifier and CMOS comparator. This sensor has shown an excellent performance [3] and is therefore suitable for this study. One of the difficulties to distinguish diffusion from other effects are pixel to pixel variations which arise from the process node size. These differences make it hard to directly compare different sensors. To overcome this difficulty, a calibration with the ^{55}Fe source was performed. This calibration enables a more precise comparison between individual sensors and allows to experimentally establish the impact of diffusion on the signal generation.

2 Particle Detection

The basis of every particle detection is the interaction of the particle with the detector material. In the interaction, energy is transferred from the particle to the material. This energy transfer then causes a signal which can be processed. The probability of interaction and the amount of transferred energy depends on the type of interaction, the incident particle and detector material. In this chapter, the interactions which are relevant to pixel sensors will be discussed.

2.1 Photons

Photons are massless particles which carry no electric charge. Photons have three different energy loss mechanisms: The photoelectric effect, Compton scattering and pair production. Which of these effects dominates the energy loss, depends on the energy of the photon. Figure 2.1 shows the predominant energy loss mechanism for photons between 10 keV and 100 MeV. In this thesis, the main photon source used is

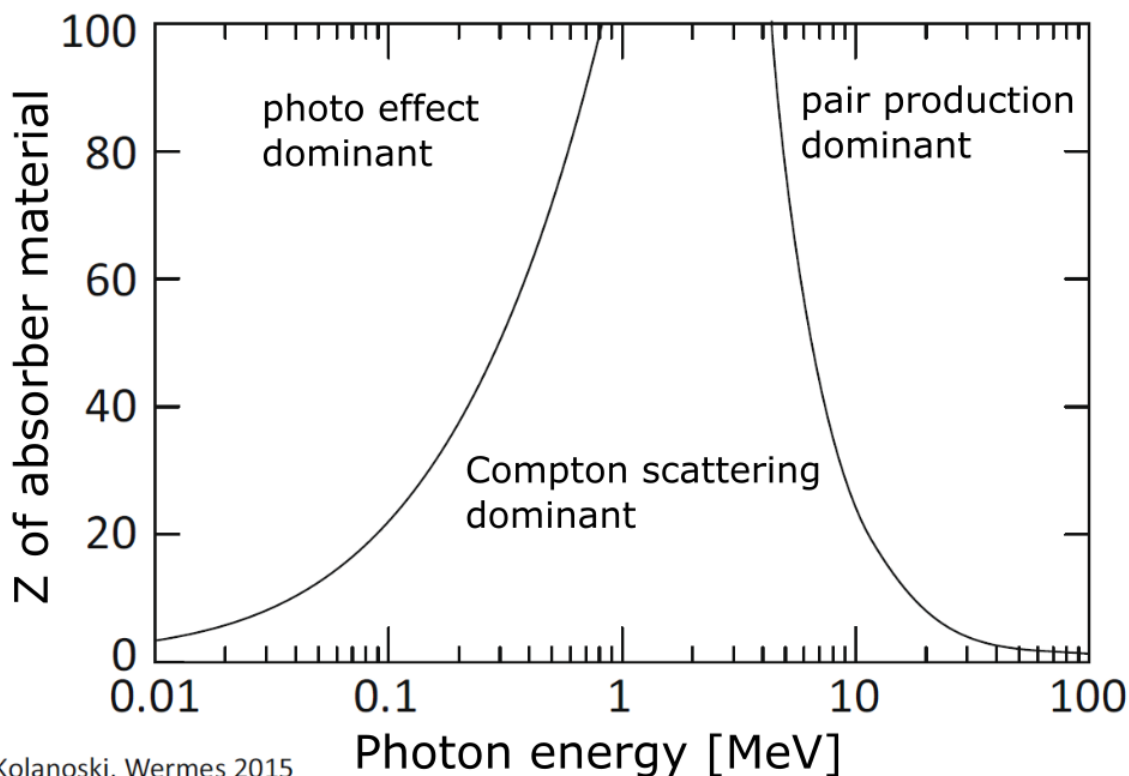


Figure 2.1: Mean energy loss for heavy particles in different materials described by the Bethe-Bloch formula [4] (edited).

^{55}Fe , which emits photons at energies of 5.9 keV and 6.4 keV, respectively. At these energies, the photo effect is the dominant mechanism. However, it should be noted that Compton scattering is also possible and has a non negligible contribution.

2.1.1 Photoelectric Effect

Photons which interact via the photoelectric effect lose all their energy to an atom. The absorbed energy is transferred to an electron which is then kicked out of its

shell. Hence, the energy threshold for this interaction is the binding energy of the electron in its shell E_B . The vacant spot in the shell is subsequently filled by an electron of an higher shell. During this process a new x-ray is emitted.

2.1.2 Compton Scattering

Another energy loss mechanism for photons is the so-called Compton Scattering. This phenomenon describes the inelastic scattering of a photon on a charged particle. The photon is scattered at an angle θ'_γ and transfers a part of its energy on the charged particle. Equation 2.1 gives the energy of the scattered photon, where E_γ is the energy of the incident photon, m_e is the rest mass of the electron and h is the Planck constant. In the interaction with detector material, the photon typically scatters of an electron in the detector material. The cross section of Compton scattering increases linearly with the charge number Z of the absorbing atom.

$$E'_\gamma = \frac{E_\gamma}{1 + \frac{E_\gamma}{m_e h} \cos(\theta'_\gamma)} \quad (2.1)$$

2.1.3 Pair Production

Pair production is the dominating effect at high photon energies. Here, the photon can produce an electron positron pair in the presence of a nucleus. It follows from simple kinematic considerations that the minimal energy for this process is 1.022 MeV:

$$E_\gamma \geq 2m_e c^2 \quad (2.2)$$

Here, c is the speed of light. The electron positron pair itself then interacts with matter and is, therefore, detectable. The interaction process of electrons and positrons is described in the following subsection.

2.2 Charged Particles

Particles which carry charge interact with the detector material via the electromagnetic force. Therefore, the amount of transferred energy depends on the charge z of the particle. For charged particles with a mass above 100 MeV, the energy loss is dominated by ionisation. The energy loss of a charged particle is described by the Bethe-Bloch formula:

$$-\left\langle \frac{dE}{dx} \right\rangle = \frac{4\pi n z^2}{m_e c^2 \beta^2} \cdot \left(\frac{e^2}{4\pi\epsilon_0} \right)^2 \cdot \left[\log \left(\frac{2m_e c^2 \beta^2}{I(1 - \beta^2)} \right) - \beta^2 - \frac{\delta(\beta\gamma)}{2} \right] \quad (2.3)$$

The equation describes the mean energy loss of a charged particle by ionization, taking into account its fraction of speed of light β , its charge number z , the density correction $\delta(\beta\gamma)$, as well as several properties of the material, such as the electron density n and the mean excitation energy I of the medium. Finally, it is also parameterized by several natural constants, such as the electron mass m_e , the speed of light c and the vacuum permittivity ϵ_0 . In Figure 2.2 the shape of the function is shown for different materials. For lower energies, the energy loss rises with a rough proportionality to β^{-2} . Furthermore, for $\beta\gamma > 3$, the Bethe-Bloch formula

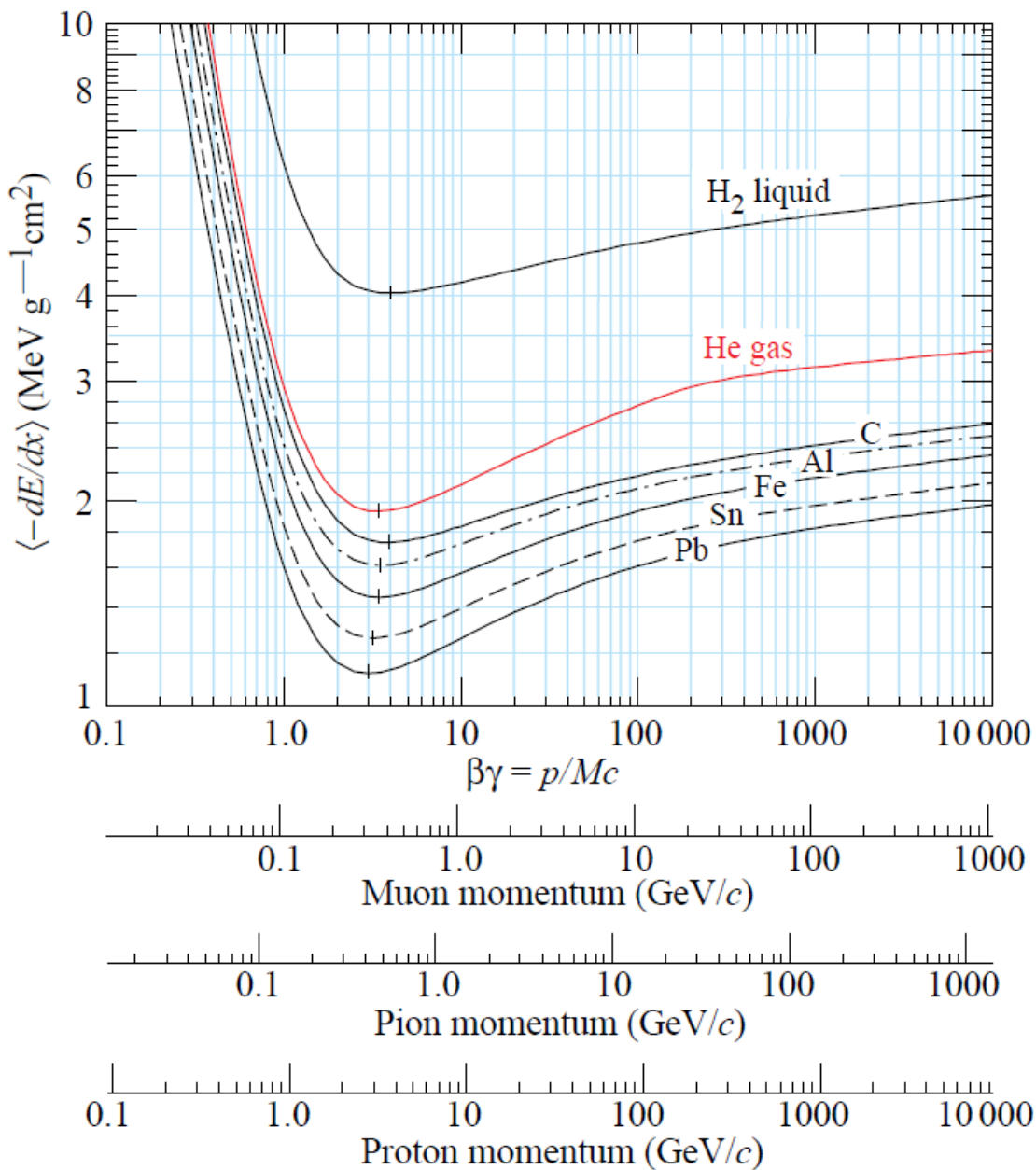


Figure 2.2: Mean energy loss for heavy particles in different materials described by the Bethe-Bloch formula [5].

shows a logarithmic rise. One of the important features of this functions is the minimum mean energy loss at $\beta\gamma \approx 3$. At this energy, a particle loses a minimal amount of energy due to ionisation and is, therefore, also called a minimum ionizing particle (MIP). The actual energy loss for a single particle is described by a Landau distribution.

2.2.1 Electrons and Positrons

The previous paragraph described the energy loss of charged particles above 100 MeV. This excludes only the electrons and positrons. There are two main reasons for their distinguished treatment. Firstly, the energy loss via Bremsstrahlung increases rapidly with increasing momentum due to their low mass. Secondly, the detector

material itself contains electrons and positrons. Hence, annihilation plays a role for positrons interacting with the detector material.

Moreover, incident electrons which interact with electrons in the detector material are indistinguishable. These quantum effects are treated in the Berger-Seltzer formula:

$$-\left\langle \frac{dE}{dx} \right\rangle = \rho \frac{0.153536}{\beta^2} \frac{Z}{A} \left(B_0(T) - 2 \log \left(\frac{I}{m_e c^2} \right) - \delta \right) \quad (2.4)$$

Here, the stopping power of the material B_0 is a function of the kinetic energy of the incident electron T . Moreover, the energy loss depends on the material density ρ , the ratio of the number of protons to nucleons $\frac{Z}{A}$, the mean excitation energy of the material I and the density correction δ . The energy loss for electrons and positrons in silicon is depicted in Figure 2.3. Here, the electrons lose more energy at high momentum due to repulsion caused by the Pauli principle.

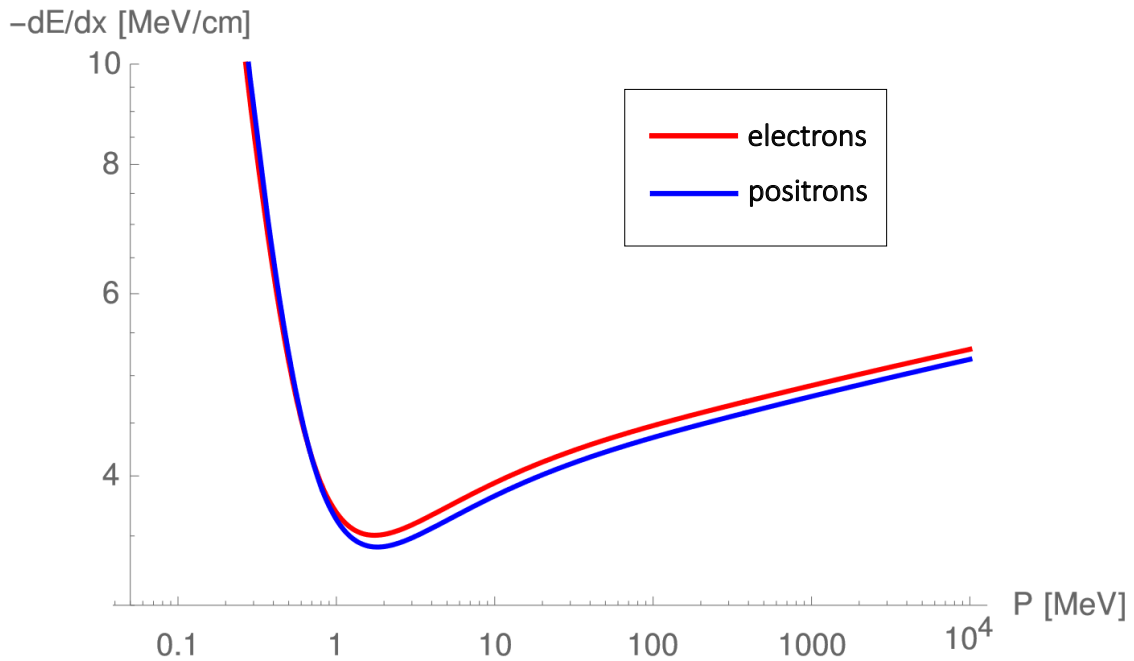


Figure 2.3: Mean energy loss of electrons and positrons in silicon [6], [7] (edited).

2.2.2 δ -Electrons

The term δ -electrons refers to electrons in the detector material, which are hit in a central collision by the traversing particle. These δ -electrons receive a high amount of kinetic energy, thus enabling them to create secondary ionization. This phenomenon causes an additional uncertainty in the detector resolution, as the secondary electrons can have a diverging direction with respect to the original particle.

3 Semiconductor Physics

3.1 Semiconductors

Semiconductors are very interesting materials for various technological applications, as their conductive properties lie between insulators and metals. In a semiconductor, the band gap between the valence and conduction band is smaller than for an insulator. Therefore, at temperatures above 0 K, electrons can be thermally excited into the conduction band. The excited electron leaves behind a vacancy which acts as a positive space charge, commonly called "hole". This process increases the conductivity of the semiconductor. If one of the thermally excited electrons loses energy, it can fill the hole in the valence band, which is called recombination. At a temperature of 0 Kelvin, the semiconductor acts as an insulator. Here, all states in the valence band are occupied by electrons, while all states in the conduction band are empty.

Semiconductor materials can be used to build pixel or strip detectors, which can detect charged particles and photons. Typical materials for this purpose are silicon (Si), germanium (Ge) and gallium arsenide (GaAs) [4]. Each of these materials has different properties and hence different applications. Germanium has a low bandgap and therefore can only be used with extensive cooling. Gallium arsenide has a high atomic Z which increases the absorption of photons (see subsection 2.1). Silicon has a medium band gap and is therefore very well suited to be operated at room temperatures. Silicon has 4 valence electrons which form a covalent bond with its neighboring atoms, very much like carbon. The properties of silicon are summarized in Table 1.

Property		Value	Unit
Atomic number	Z	14	
Atomic mass	m_a	28.09	u
Density	ρ_{Si}	2.328	g/cm^3
Intrinsic charge carrier density	n_i	1.01×10^{10}	cm^3
Dielectric constant	ϵ_{Si}	11.9	ϵ_0
Specific resistivity	ρ	2.3×10^5	Ωcm
Average energy for e/h-pair creation	w	3.65	eV
Indirect band gap	E_{gap}	1.12	eV
Radiation length	X_0	9.36	cm
Electron mobility	μ_n	1450	$\text{cm}^2\text{V}^{-1}\text{s}^{-1}$
Hole mobility	μ_p	500	$\text{cm}^2\text{V}^{-1}\text{s}^{-1}$
Life time e/h	$\tau_{e/h}$	> 100	μs
Fano factor	F	0.115	

Table 1: Properties of silicon at a Temperature of 300 K [4].

3.2 Doping

In the following the process of doping is described exemplary for silicon. Here, the intrinsic charge carrier density is small compared to the atomic density. Therefore, pure silicon acts as an insulator. To increase the electrical conductivity, impurities are introduced into the lattice, effectively increasing the amount of free charge carriers. This process is called doping and can be applied in two different ways [4]:

- **p-doping:** Here, an acceptor element from group-III is added to introduce additional holes to the lattice, which then can capture a valence electron. Therefore, the number of free electrons decreases and the majority charge carriers in this case are holes. Typical elements are boron, aluminum, gallium or indium.
- **n-doping:** A donor element from group-V is added to introduce additional electrons to the conductor band. Hence, the number of free electrons increases and the majority charge carriers in this case are electrons. Typical elements are phosphorus, arsenic, antimony, bismuth or lithium.

3.3 The pn-junction Diode

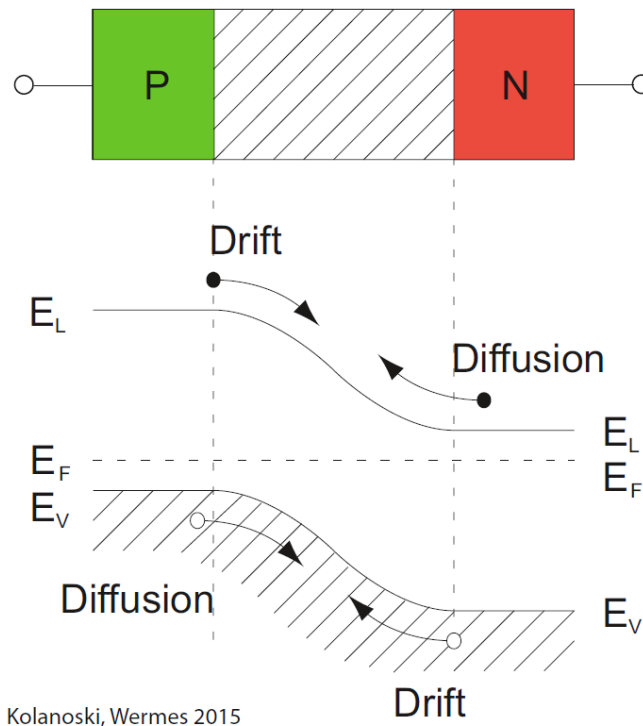


Figure 3.1: Drift and diffusion current of a pn-diode [4].

It is possible to take advantage of the two types of doping by forming a p-n junction, also called diode. For this, the surface of a p-doped material is brought into contact with an n-doped material. At the intersection of both materials, there is a high concentration gradient of free charge carriers. This leads to a diffusion current, where the free electrons from the n-doped material diffuse into the p-doped

material and recombine with the free holes of the p-doped material and vice versa. Hence, a region with no free charge carriers is created, the so-called depletion zone. At this point, an intrinsic electric field is created, causing a drift current which flows in opposite direction of the diffusion current. If no external bias voltage is applied, these two currents reach a stable equilibrium. However, an external voltage can be applied to manipulate the depth of the depletion zone w , which is then given by [4]:

$$w = \sqrt{\left(\frac{2\epsilon\epsilon_0(U - U_0)}{e}\right) \frac{N_A + N_D}{N_A N_D}} \quad (3.1)$$

where ϵ is the dielectric constant of silicon, $U - U_0$ is the external bias voltage minus the intrinsic voltage of the diode, N_A and N_D are the acceptor and donor doping concentrations, e is the elementary charge and ϵ_0 is the vacuum permittivity. This equation simplifies to Equation 3.2 in the case of $U \gg U_0$ and $N_D \gg N_A$:

$$w = \sqrt{\frac{2\epsilon\epsilon_0 U}{e N_A}} \quad (3.2)$$

In principal there are two possibilities to apply an external voltage:

- **forward bias** $U > 0$: Forward biasing leads to a decrease of drift current relative to the diffusive current. Therefore, the depletion depth is reduced.
- **reverse bias**: $U < 0$: Reverse biasing leads to an increase of drift current relative to the diffusive current. Therefore, the depletion depth is extended.

In the case of a silicon particle detector, the depleted region is the sensitive volume in which particles can be detected (see also subsection 3.5). Hence, the reverse bias case is of particular interest.

An important quantity is the capacitance of the diode. If the diode is connected to an electronic circuit (e.g. a readout), the diode can act as parasitic capacitance. It can be calculated by assuming a parallel plate capacitor for the diode, where the depleted substrate functions as dielectric. Accordingly, the capacitance is given in Equation 3.3 by the intersection area of the pn-junction A divided by the depletion depth w [4]:

$$C = \frac{A\epsilon\epsilon_0}{w} = A\sqrt{\frac{eN_A\epsilon\epsilon_0}{2U}} \quad (3.3)$$

It is possible to replace the acceptor density N_A with the substrate resistivity ρ and the hole mobility μ_p of the material, yielding new expression for Equation 3.2 and Equation 3.3:

$$\rho = \frac{1}{eN_A\mu_p}; \quad N_A = \frac{1}{e\rho\mu_p} \quad (3.4)$$

$$w = \sqrt{2\epsilon\epsilon_0 U \rho \mu_p} \quad (3.5)$$

$$C = A\sqrt{\frac{\epsilon\epsilon_0}{2U\rho\mu_p}} \quad (3.6)$$

Furthermore, in the diode a leakage current (also called dark current) forms, which arises from thermal excitation of charge carriers in the depleted zone or diffusion of

such charge carriers into the depleted zone. Therefore, the dark current is highly temperature dependent:

$$I(T) \propto T^2 e^{-\frac{1.21eV}{2k_B T}} \quad (3.7)$$

The leakage current is the main source of noise in the diode and hence is an important quantity for the application of the diode as particle detector.

3.4 Diffusion in Semiconductors

Diffusion denotes a phenomenon where particles move due to a gradient in particle concentration Δn . The emerging current is proportional to $-\Delta n$ and corresponds microscopically to a random walk. The laws of diffusion can be derived from the Boltzmann transport equation and are named after their discoverer Fick's laws. Equation 3.8 describes the diffusive charge transport, where $Q_0(\vec{x}')$ describes the initial charge distribution, D the diffusion constant (see Equation 3.10) and t the diffusion time [8]. In silicon the electrons as well as the holes are subject to diffusive movement. It should be noted, that holes and electrons have different diffusion constants.

$$\frac{dQ}{dx}(\vec{x}, t) = \frac{1}{8(\pi Dt)^{\frac{3}{2}}} \int Q_0(\vec{x}') e^{-\frac{\vec{x}-\vec{x}'}{4Dt}} d\vec{x}' \quad (3.8)$$

Under the assumption of a point charge, the Gaussian spread can be calculated. This gives an estimate on the mean squared deviation (MSD) of a charge from its point of creation:

$$\sigma = \sqrt{2Dt} \quad (3.9)$$

The Einstein equation calculates the diffusion constant:

$$D = \mu_{e/h} \frac{k_B T}{q} \quad (3.10)$$

Here, $\mu_{e/h}$ is the electron or hole mobility, T is the temperature, q is the electron or hole charge and k_B is the Boltzmann constant. In principle, the free charges are subject to recombination. However, the mean life time of the free charge carriers is in the order of 100 μs for the substrate used within this thesis [9]. Hence, recombination is negligible on the time scale of the signal.

3.5 Charge Collection

To detect a particle, it needs to interact with the detector material and deposit energy in the detector material. Moreover, the energy deposition has to be transformed into a signal. In the case of a pixel detector the energy is deposited via ionisation caused by a charged particle or photon (which then produces a secondary particle) traversing the detector material. Within the sensitive detector material there are two regions: the depleted substrate, where charge is collected through drift and the undepleted substrate where charge can be collected via diffusion. In both of these regions, free charge carriers are created by ionisation. In the following these two mechanisms of charge collection are discussed in more detail.

3.5.1 Charge Collection via Drift

Charge collection through drift only can happen in the presence of an electric field. Therefore, this is only possible in the depleted volume. The drift velocity can be calculated by the Drude model [4]:

$$\vec{v}_{drift} = Q_{e/h} \mu_{n/p} \vec{E} \quad (3.11)$$

It should be noted, that electrons have a higher mobility μ_n in silicon compared to the holes. For the HV-MAPS only the signal of the fast electrons is read out and thus holes are not considered anymore in the signal generation subsequently.

3.5.2 Charge Collection via Diffusion

In first approaches to understand the charge collection in an HV-MAPS, the charge collection through diffusion was thought negligible. However, lately theoretical considerations showed that diffusion might have a sizable impact on the signal [10]. The charge contributes to the signal, if it diffuses into the depleted volume. As soon as the charge enters the depletion volume, it is rapidly collected via drift. For more information on the charge collection via diffusion see subsection 5.7.

3.6 Signal Generation

Next, the signal generation is discussed in more detail. The movement of the charge carriers in the electric field creates an inductive charge on the electrode. This process is described by the Shockley-Ramo theorem [11].

$$i(t) = \vec{E}_w \vec{v}_{drift} q(t) \quad (3.12)$$

Here, i is the induced current and \vec{E}_w is the so-called weighting field. This weighting field is the theoretical field of the electrode set to unit potential with all other electrodes at zero potential. As discussed in the previous subsection, the electrons induce the signal in HV-MAPS. The electron velocity is mainly determined by the electric field. For moderate electric fields up to approximately 3×10^3 V/cm the relationship between velocity and electric field is linear. At higher electric fields, the velocity starts to saturate due to inelastic interaction with phonons and reaches saturation at approximately 5×10^4 V/cm, where the velocity of the electron is 10^7 cm/s [12]. From electric field studies with TCAD [13] it is known, that the electric field within the depletion zone is in the order of 10^4 V/cm for a substrate resistivity of $370 \Omega \text{ cm}$ at the typical external bias voltage. Hence, the velocity of the electrons within the electric field is fairly saturated.

At very high electric fields, the diode reaches the so-called breakdown. The breakdown is caused by primary electrons, which gather enough energy between collisions to create secondary electron-hole pairs. If the electric field is large enough, a self sustaining avalanche process starts, leading to the huge current increase. This effect can thermally destroy the diode.

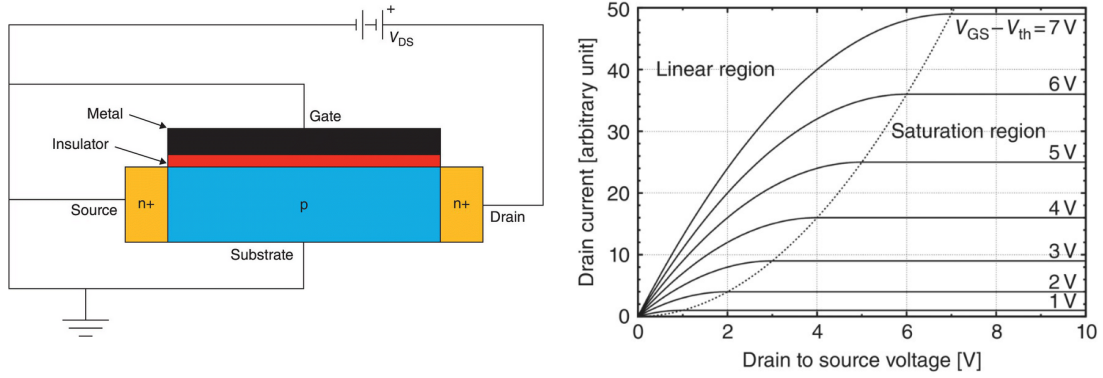


Figure 3.2: Schematic (left) and characteristic drain current against the drain to source voltage behavior of an NMOS MOSFET (right) [14].

3.7 MOSFET

The metal-oxide-semiconductor-field-effect transistor, or short MOSFET, is a type of field-effect transistor. It is a voltage controlled switching element, where the applied voltage regulates the current. Hence, it is also used as a logical switching element. There are two types of MOSFET transistors, p-channel (PMOS) and n-channel (NMOS). Furthermore, these two types can be combined on the same substrate into a complementary MOS (CMOS). This is achieved by placing PMOS and NMOS transistors in so-called wells, which are specifically doped regions. Moreover, the simultaneous usage of both types of MOSFET allows a reduced power consumption as the current can be switched off by the applied voltage. On the left side of Figure 3.2 the schematic of an NMOS is shown. It consists of an isolated gate and two heavily doped n^+ regions which are placed in contact with a p-substrate, also called bulk. The thin sheet of dielectric material between the p-substrate and the gate often is silicon dioxide (SiO_2). The n-doped regions act as source and drain and form a pn-junction with the p-substrate in equilibrium. Moreover, the p-substrate and gate form a parallel plate capacitor. If a positive voltage is applied at the gate, positive charges accrue at the gate and negative charges on the top of the substrate. In a semiconductor this means that the mobile holes move to the bottom of the substrate. If a voltage V_{GS} is applied between the gate and the source, a channel between source and drain is formed. This channel allows a current I_D to flow between these two elements, where the voltage V_{GS} controls the amount of current. The right side of 3.2 shows the drain current plotted against the drain to source voltage for different values of $(V_{GS} - V_{Th})$. Depending on the applied voltage, the transistor can be operated in three different modes:

- **Sub-Threshold Mode:** $V_{GS} < V_{Th}$

In this mode the transistor is switched off and can be used as a logic element. In this mode, only a small so-called sub-threshold leakage current can flow [15]:

$$I_D = \frac{W}{L} I_{D0} \cdot \left[e^{\frac{V_{GS}}{nV_T}} \right], \quad \text{with} \quad V_T = \frac{k_B T}{q}, \quad n = 1 + \frac{C_{\text{Dep}}}{C_{\text{Ox}}} \quad (3.13)$$

Here, W is the effective channel width, L the effective channel length, I_{D0} the current at $V_{GS} = V_{Th}$, V_T the thermal voltage, C_{Dep} and C_{Ox} the capacitance of the depleted layer and of the oxide layer, respectively.

- **Linear Mode:** $0 < V_{DS} < (V_{GS} - V_{Th})$

By increasing V_{GS} , the linear mode is reached and the transistor is switched on. In this case, a current can flow which is proportional to V_{DS} and the transistor acts as a resistor. Therefore, the current can be controlled by V_{DS} [16]:

$$I_D = \frac{\mu_0 C_{Ox} W}{L} \left((V_{GS} - V_{Th}) - \frac{V_{DS}}{2} \right) \cdot V_{DS} \quad (3.14)$$

- **Saturation Mode:** $0 < (V_{GS} - V_{Th}) \leq V_{DS}$

At the point where V_{DS} is comparable to $(V_{GS} - V_{Th})$, the current I_D is not any longer determined by V_{DS} , but rather by V_{GS} [16].

$$I_D \approx \frac{\mu_0 C_{Ox} W}{2L} (V_{GS} - V_{Th})^2 \quad (3.15)$$

II HV-CMOS Sensors

4 Pixel Detectors

In most modern particle physics experiments, the inner tracking layers consist out of silicon pixel sensors. Here, a supreme spatial resolution is crucial to differentiate the particles in a high track density environment and determine the momentum precisely. Both of these requirements are met by pixel detectors. In most of the currently operating modern experiments hybrid sensors are used for this task.

4.1 Hybrid Pixel Detectors

A hybrid pixel sensor consists out of two parts: First, there is a sensor which contains the sensitive detection volume. A bias voltage is applied to the sensor, which is typically in the order of several hundred volts. Secondly, a readout ASIC (Application-Specific Integrated Circuit) which houses the necessary readout electronics as for example the amplifier. These two chips need to be bump bonded to each other, making manufacturing complex and expensive. However, the separation of these two entities allows a precise characterization and dedicated optimization of both of them. Many years of research led to a vast amount of experience, making this the default technology for large experiments at CERN. Overall, the radiation hardness, high granularity and experience with the technology are advantages which explain the huge success of these detectors. An example for this detector is the RD53B [17] chip, which is currently developed for the ATLAS and CMS experiment. It is manufactured in a node size of 65 nm and has a pixel size of $50 \times 50 \mu\text{m}^2$.

4.2 Monolithic Active Pixel Sensors (MAPS)

In a MAPS the two entities of readout and active volume are combined in one sensor. Generally, this kind of diode is realized as a highly doped electrode, placed in a high resistivity epitaxial layer, where the latter is the sensitive detection volume. The charge is collected via diffusion at the electrode, while a secondary well houses additional n- and p-wells for the in-pixel circuitry. A so-called periphery houses additional electronics, as the clock of the sensor. This is an insensitive area in which particles can not be detected. However, charge transport via diffusion is comparably slow, leading to a limited time resolution in the order of a few microseconds in this detector. This design is possible with commercial CMOS technology, hence reducing the production cost and increasing the availability. Additionally, the sensor can be thinned down to a thickness of $50 \mu\text{m}$ to reduce the material budget. An example for this technology is the ALPIDE [18], which is used in the ALICE experiment. It has a small pixel size of approximately $27 \times 29 \mu\text{m}^2$, facilitating an extraordinary spatial resolution at ultra-low material budget. The event time resolution is between 2 ns to 4 ns [19].

4.3 HV-MAPS

The advantages of hybrid pixel sensors and MAPS can be combined in the High-Voltage Monolithic Active Pixel Sensors (HV-MAPS) technology. It offers the low production cost of commercial CMOS technology as well as a time resolution in the few nanosecond regime. The sensors can be thinned down to $50 \mu\text{m}$, allowing the

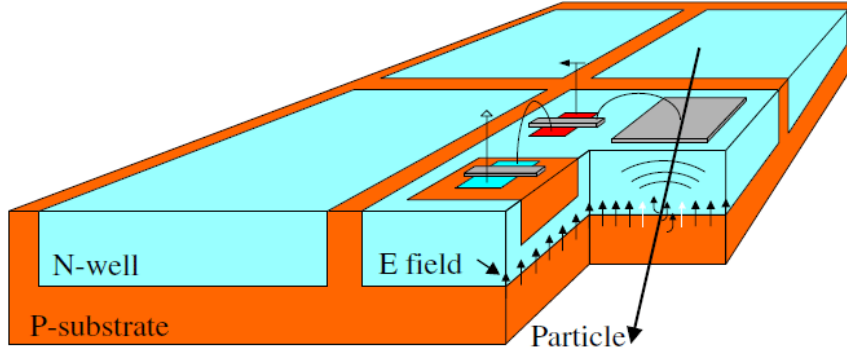


Figure 4.1: HV-MAPS concept [22].

application in environments where particles are at relatively low momenta. Figure 4.1 shows the concept of the HV-MAPS. In this technology, the diode is formed by a deep n-well placed in a p-substrate. Moreover, a voltage of up to -150 V can be applied to reverse bias the diode. This further enhances the depletion volume and therefore also the sensitive detector volume. A substantial part of the charge is collected through drift at the deep n-well which enables the superior time resolution in comparison to the MAPS approach. The deep n-well houses multiple shallow n- and p-wells in which PMOS and NMOS transistors can be placed, respectively. This allows for dedicated in-pixel electronics. Again, the clock circuitry and other electronics are housed in the periphery. An example of this is the MuPix11[20], which has a pixel size of $80 \times 80 \mu\text{m}^2$. The time resolution is 15 ns before and 6 ns after row and time walk correction [21].

An example for the utilization of the HV-MAPS technology is the Mu3e experiment. It searches for the charged lepton flavor violating decay $\mu^+ \rightarrow e^+e^+e^-$, which is suppressed in the standard model with a factor of about 10^{-54} [2]. The current limit of this decay is 10^{-12} [1], while the Mu3e experiment aims to either exclude or observe the decay up to a branching ratio of 10^{-16} [23]. To achieve this goal in a feasible measurement duration, a high intensity muon beam with a rate of 10^9

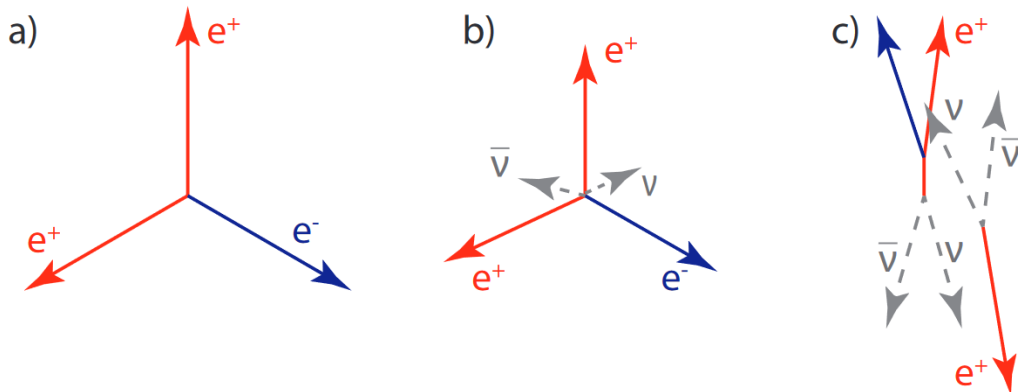


Figure 4.2: Signal and background processes for the $\mu^+ \rightarrow e^+e^+e^-$ decay. Figure (a) shows the signal decay, while (b) displays the internal conversion decay. Figure (c) depicts the accidental background of two Michel decays with a Bhabha scattering [23].

is necessary. To exclude accidental background shown in Figure 4.2, it is necessary to measure the momentum of the decay particles precisely, making excellent spatial resolution essential. The low energetic muons will be stopped in a helium target and decay at rest. Therefore, the resulting electrons are at low momenta of $53 \text{ MeV}/c$ and below. At these momenta, the specified spatial resolution is dominated by the multiple Coulomb scattering of the electrons and positrons in the detector material. Hence, the material budget of the detector needs to be as small as possible. The design goal for the Mu3e experiment is a relative radiation length of $X/X_0 \sim 0.1\%$ per layer, which is allowing a thickness of only $50 \text{ }\mu\text{m}$ for the silicon sensors [23].

In summary, the requirements for the Mu3e vertex detector are ultra thin sensors to keep the material budget low, while maintaining an excellent time resolution of below 20 ns and spatial resolution with a hit efficiency above 99% . The HV-MAPS technology was developed to meet these requirements. After extensive R&D efforts, the final version of the sensor, the MuPix11, is fully working and even surpasses many of the initial requirements [21]. Currently, the first modules of the Mu3e experiment are under construction.

4.4 The Run 2021 V2 Sensor

The Run2021v2¹ sensor is a small scale R&D prototype. The sensor is produced by TSI Semiconductors² in a 180 nm process. The comparably low cost of a small scale sensor is advantageous to test new designs. The Run2021v2 sensor features advanced in-pixel electronics such as a CMOS amplifier and comparator. With regard to the in-pixel electronics this is one of the most advanced HV-CMOS sensor currently available. Moreover, in the clock of the sensor a 8 ns time binning is implemented, enabling an outstanding time resolution for a HV-CMOS sensor. Figure 4.3 shows a high resolution picture of the prototype. The top part of the sensor houses the pixel matrix with the 29×124 pixels, which have a size of $165 \times 25 \text{ }\mu\text{m}$. This is the sensitive detector area of 14.834 mm^2 . The bottom part of the sensor is housing the periphery and the power pads, with the bond wires connected.

Another new feature in the Run2021 sensors is the separation between pixel guard ring and chip guard ring. In earlier designs the guard rings were effectively shorted, while in the new design an additional n-well is placed in between the two guard rings. This forces the current to flow through the substrate. Figure 4.4 displays the schematic layout of the guard rings. The chip guard ring is the outer guard ring, surrounding the full matrix, while the pixel guard ring is the inner guard ring, dividing the individual pixels from each other. A study of the impact of this new feature on the signal and breakdown voltage is presented in section 7.

The simplified circuitry is depicted in Figure 4.5. The signal is created in the reversely biased sensor diode, which is capacitively coupled to the charge sensitive amplifier (CSA). A feedback circuit creates a constant current, leading to a linear falling edge and therefore to a linearity between signal amplitude and pulse duration. Subsequently, the amplifier output passes another capacity and is modulated on a baseline. This voltage is connected to on one input of a comparator. The second input for the comparator is the applied threshold, which is adjustable. As long as the signal is larger than the threshold, a digital signal is put out. As soon as the

¹The Run2021v2 sensor is also known as TelePix or TelePix1 in other publications.

²TSI Semiconductors, USA, <https://www.tsisemi.com>

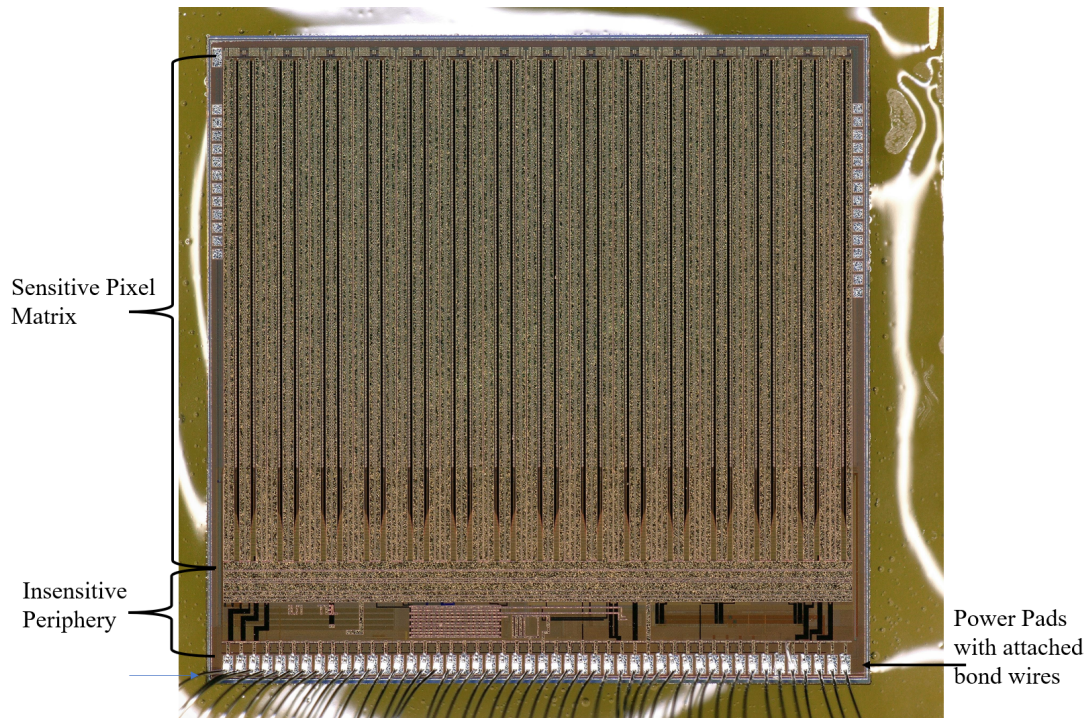


Figure 4.3: High resolution image of the Run2021v2 sensor, glued and bonded to its insert.

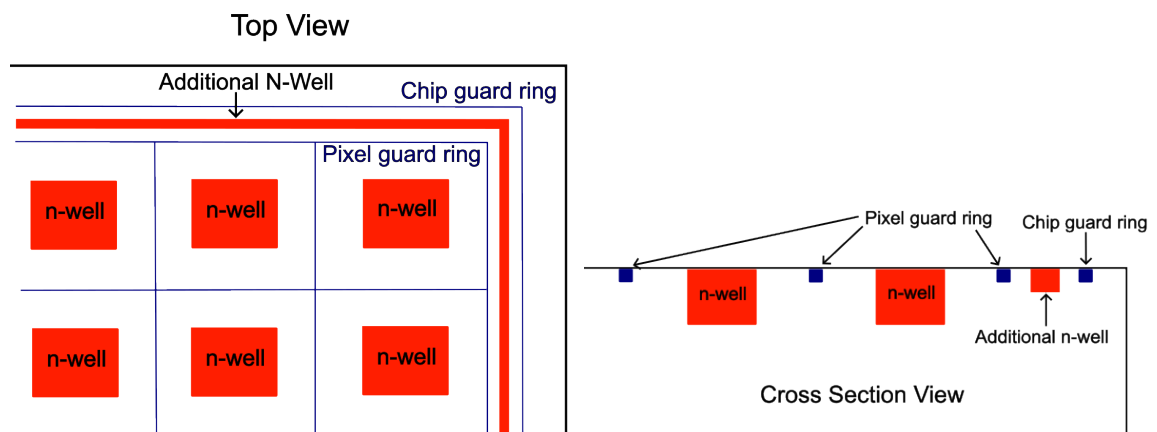


Figure 4.4: Schematic drawing of the guard ring structures in top view (left) and cross sectional view (right).

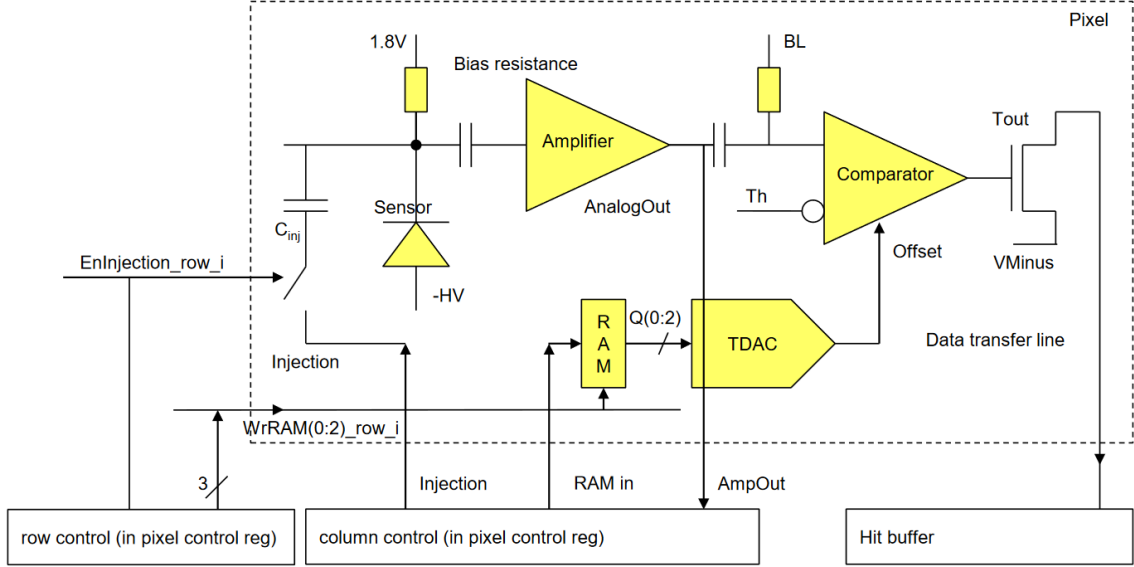


Figure 4.5: A simplified circuit diagram of the in-pixel electronics for the Run2021v2 sensor [24]. For more information see text.

threshold of the comparator is crossed a timestamp t_1 is created. When the signal drops below the threshold, a second timestamp t_2 is created. With these timestamps one can calculate the Time-over-Threshold (ToT):

$$ToT = t_2 - t_1 \quad (4.1)$$

The discriminated pulse is send to the periphery. Finally, the digitized information is transferred to the further data acquisition (DAQ) entities, described in the subsequent section.

Property	Value	Unit
Sensor Size	5×5	mm^2
Matrix	29×124	Pixel
Pixel Size	165×25	μm^2
Active Area	$4.785 \times 3.1 = 14.834$	mm^2
Thickness	50, 100, 300, 650-750 (unthinned)	μm
Substrate Resistivity	20, 370, ~ 8000	Ωcm
Efficiency	> 99	%
Time Resolution [3]	< 2.4	ns

Table 2: Summary of sensor performance and design.

Table 2 summarizes the design and performance of the sensor. It has a highly asymmetrical pixel size, where the pixel pitch in row direction is only $25 \mu\text{m}$ wide.

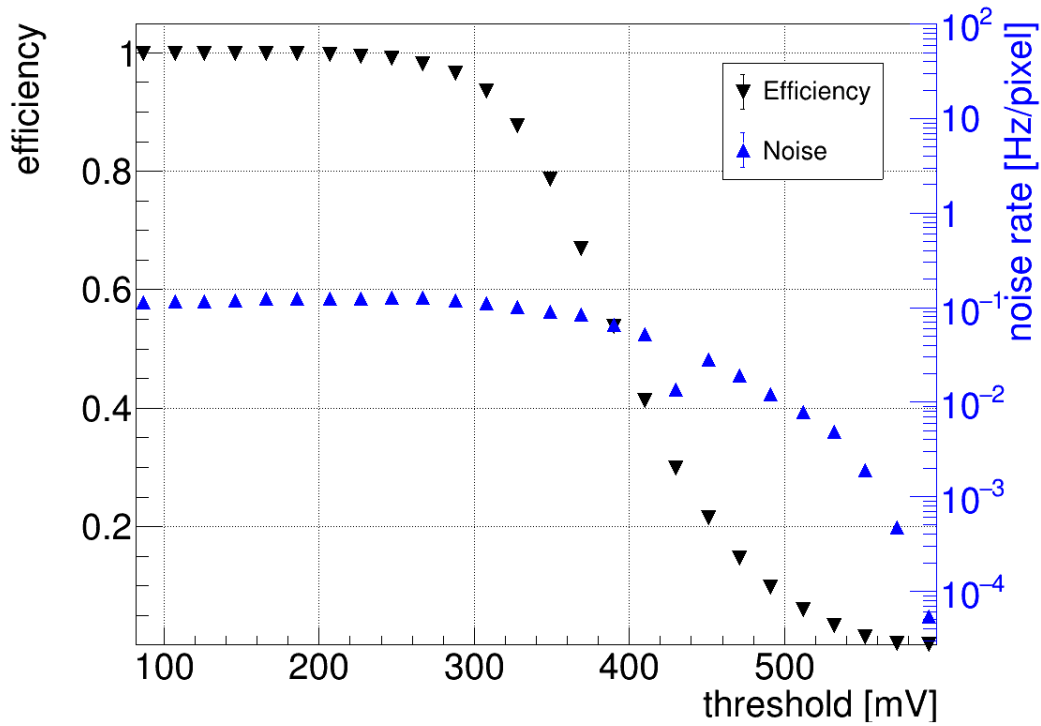
For the substrate resistivity of 370 Ωcm , three different thicknesses are available: 50 μm , 100 μm and unthinned, which is approximately 650 μm to 750 μm thick. The sensors with a resistivity of 20 and 8000 Ωcm are only available in one or two different thicknesses, respectively. Hence, the investigations within this thesis focus on sensors with a substrate resistivity of 370 Ωcm .

The performance of the Run2021v2 sensor is shown in Figure 4.6, where the efficiency and average noise rate per pixel are displayed on the top and the time resolution on the bottom. These results were obtained with a 100 μm sample at the DESY test beam facility [25] at a beam energy of 4 GeV. The top part of the figure displays the efficiency (black) and the average noise rate in Hertz per pixel (blue) plotted against the applied threshold for a bias voltage of -130 V. Here, the efficiency stays above 99% for a threshold range of nearly 150 mV, while the average noise rate per pixel is below 0.2 Hz/pixel for all displayed thresholds. The bottom part of the figure shows the time resolution obtained at a bias voltage of -70 V and a threshold of 108 mV. The time resolution was measured with respect to a fast LySo crystal connected to a silicon photomultiplier (SiPM). The Gaussian fit to the core of the distribution yields an unprecedented time resolution of 2.4 ns [3].

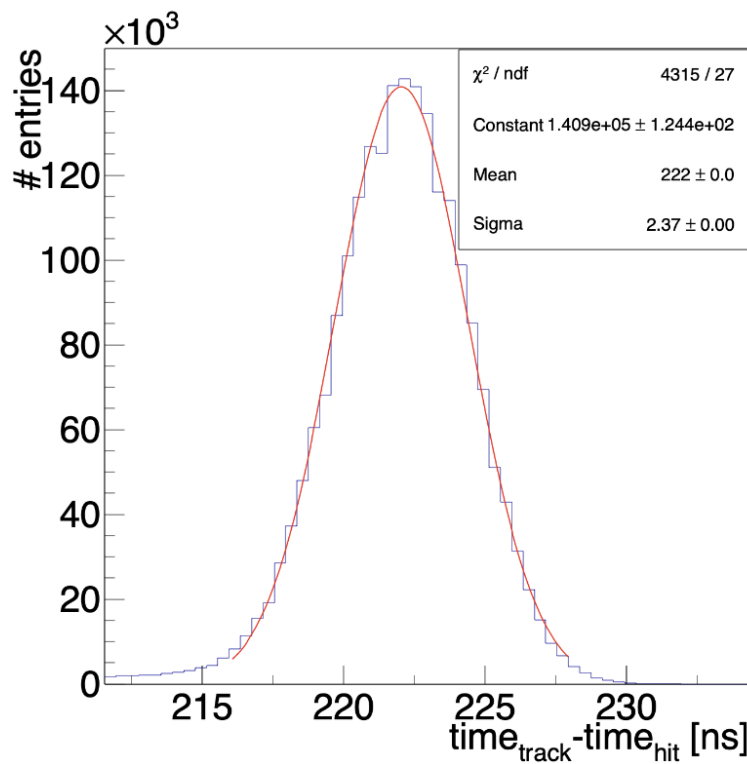
4.5 The Injection Circuit

The injection circuit is a rather simple test circuit to probe the amplifier and comparator of a sensor with reproducible artificial signals. The charge is directly injected into the amplifier and thus is not influenced directly by the depletion volume or the electric field within it, as depicted on the left side of Figure 4.5. However, it should be noted, that the depletion volume acts as a parasitic capacitance and therefore influences the shaping of the amplifier. The created charge is depending on the injection voltage U_{Inj} and the injection capacity C_{Inj} :

$$Q_{\text{Inj}} = U_{\text{Inj}} \cdot C_{\text{Inj}} \quad (4.2)$$



(a) Efficiency (black) and average noise rate in Hertz per pixel (blue) plotted against the applied threshold for a bias voltage of -130 V.



(b) Time resolution of an $100 \mu\text{m}$ sensor biased with -70 V [3].

Figure 4.6: Performance of the Run2021v2, efficiency and average noise rate per pixel (a) and time resolution (b).

5 Measurement Setup

In this section the components of the sensor setup are described. Moreover, the radioactive sources which will be used within the course of this thesis are introduced. Finally, the measurement approach to quantify the impact of diffusion on the signal is explained.

5.1 Motherboard PCB

Within the HV-MAPS research group in Heidelberg, a so-called "motherboard" printed-circuit-board (PCB) [26] was developed to test and operate HV-CMOS sensors. The motherboard offers vast possibilities to characterize and investigate sensors. Using a common motherboard for multiple sensors, minimizes systematical errors. A dedicated insert PCB was designed to house each sensor type, which will be explained in subsection 5.2.

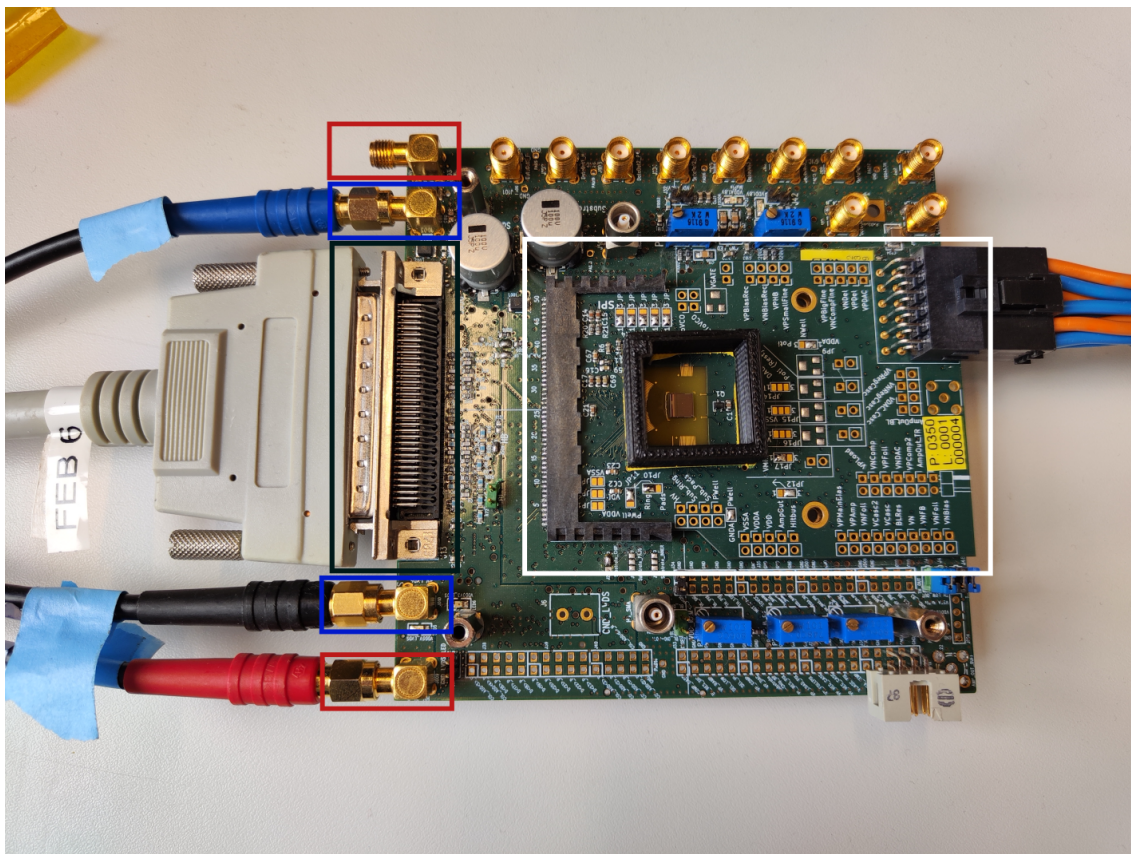


Figure 5.1: Standard Mupix-type motherboard PCB connected to a Run2021 insert PCB. The color-coding is explained in the text.

Figure 5.1 shows a picture of the motherboard with an insert attached. On the left-hand side 4 SMA connectors are highlighted in blue and red. The high voltage (red) can be supplied through the pixel guard ring (upper one) or the chip guard ring (lower one). If not stated otherwise, the results within this thesis are obtained by supplying the high voltage via the chip guard ring. A study on how the high voltage biasing of each guard ring influences the sensor is presented in section 7. The two middle one SMA connectors (blue) are supplying the low voltage of 5 V which

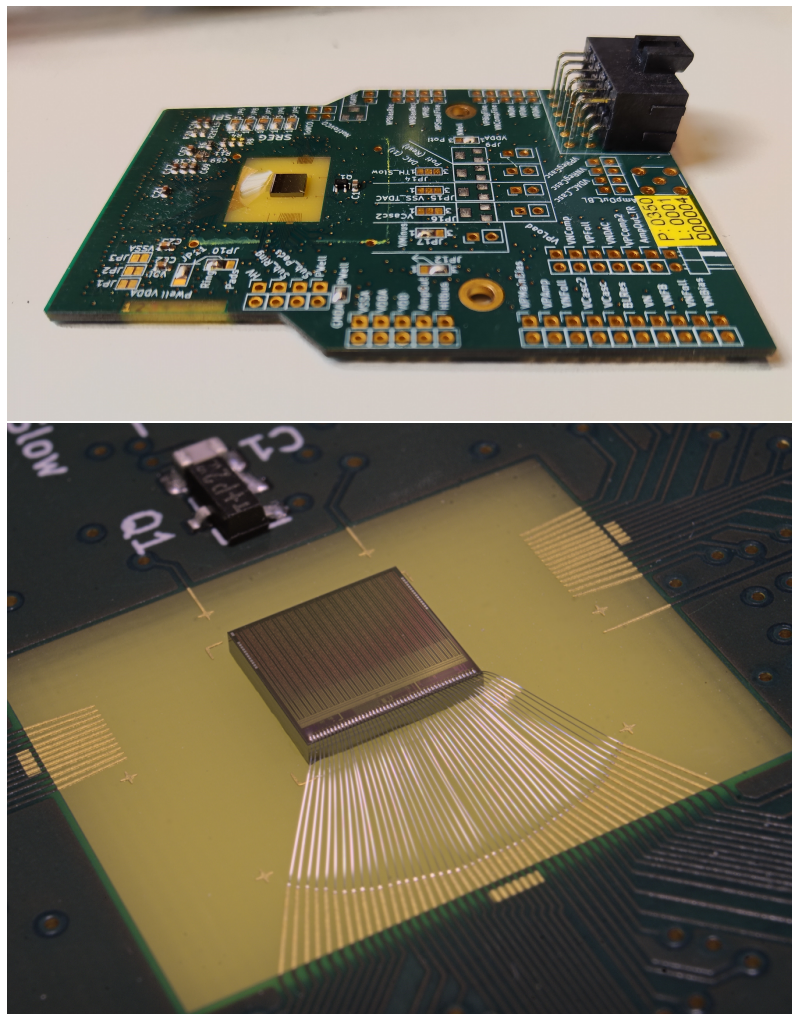


Figure 5.2: An unthinned Run2021v2 sensor, glued and bonded to the insert PCB.

then can be regulated on the motherboard. A fine tuned adjustment is possible through digital-to-analog converters (DACs), which can be steered via the software interface. The insert PCB is highlighted in the picture in white. On the right side of the sensor an additional low voltage is supplied directly to the sensor. In the case of the Run2021v2 sensor, it supplies the VDDD (digital) and VDDA (analog) voltages, while the VSSA is regulated down from these voltages on the sensor. On the left hand side between the SMA connectors, the SCSI-3 connector is highlighted in black. This provides the interface between the sensor and the DAQ-PC.

5.2 Insert PCB

As already mentioned in the subsection 5.1, the PCB is directly designed for one certain sensor type and can be used for all subversions in the case of the Run2021 chip. Figure 5.2 shows an unthinned Run2021v2 sensor glued and bonded to its insert PCB.

5.3 FPGA Interface

A Field-Programmable Gate Array Interface, short FPGA, is used to provide the external clock to the sensor, configure the chip and process its data. The FPGA is an integrated circuit with programmable logic units on it. The FPGA used in this thesis is the Stratix IV GX Development Board [27]. It is directly connected to the DAQ computer by a PCI express connection.

5.4 DAQ

The data acquisition (DAQ) software allows to either test multiple sensors in a telescope environment or characterize a single sensor in the laboratory. The created data can then be analyzed with the Corryvreckan framework, which is introduced in section 6.

5.5 Test Beam Setup

Within this thesis, results from a test beam at the DESY II test beam facility in Hamburg, Germany are presented. Therefore, the test beam facility itself and the measurement setup during the test beam is introduced in this subsection. The DESY II test beam facility offers an electron beam in the range of 1 to 6 GeV [25]. For the results in this thesis, a beam energy of 4 GeV is used. The beam is produced by photons impinging on a target and undergoing pair production. The electrons or positrons then are separated by a magnet.

In principle, the DESY test beam facility offers a ALPIDE based ADENIUM telescope [30] and a MIMOSA26 telescope to the users. The latter one is currently being replaced with a TelePix2³ telescope [31]. However, within this thesis the telescopes offered by the DESY test beam facility were not used. Instead, a custom telescope consisting of MuPix type sensors is used. A schematic of the setup and a picture of assembled telescope is shown in Figure 5.3. Here, the sensors are aligned perpendicular to the electron beam. The three reference planes are MuPix11 sensors and the DUT is a Run2021v2 sensor. For a more precise time information scintillating tiles are placed in front and behind the telescope.

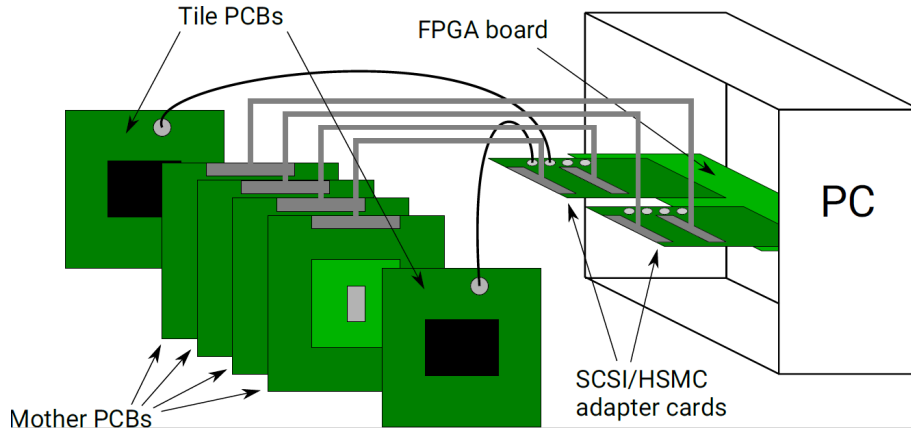
5.6 Radioactive Sources

Radioactive sources are a convenient way to study charge deposition in a laboratory environment. The two radioactive sources which are used within this thesis will be introduced in the following.

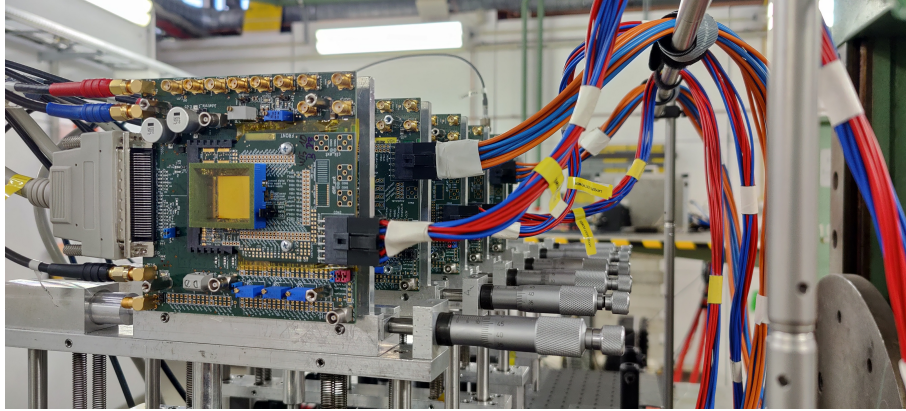
5.6.1 Strontium-90

First, the Strontium-90 source will be introduced. The ^{90}Sr decays to Yttrium-90 via β^- decay with a half-life of 28.79 years [32]. The decay is a 3 body decay into an e^- , a $\bar{\nu}$ and a ^{90}Y atom, where the decay products share the decay energy of 0.546 MeV [33]. The ^{90}Y atom itself will undergo radioactive decay to the stable Zirconium-90 with an decay energy of 2.28 MeV [34], again splitted between the e^- , a $\bar{\nu}$ and a ^{90}Zr atom. The half-life of this decay is 64 hours [32]. Figure 5.4 shows

³The TelePix2 is the full-scale successor of the Run2021v2 R&D sensor presented in this thesis.



(a) Schematic of the measurement setup at the DESY test beam facility [28].



(b) MuPix 11 telescope with the Run2021 sensor as DUT in the second telescope plane.

Figure 5.3: Measurement setup at the DESY test beam facility [29].

a calculated cumulative spectrum of the ^{90}Sr and ^{90}Y decay. As both decays are three-body decays, the energy of the electron is not fixed. The electrons created by the ^{90}Sr decay, which correspond to the low energetic peak in Figure 5.4, are rapidly losing energy when interacting with matter due to the sharp rise in the Berger-Seltzer formula (see Equation 2.2.1). In typical radioactive sources a thin window is placed before the source for safety reasons. Therefore, these low energetic electrons can not be observed in the detector, as this window is enough material to absorb them. Hence, only the electrons created by the ^{90}Y decay can be observed.

5.6.2 Iron-55

Second, Iron-55 is a gamma source with a half-life of 2.737 years [32]. The main decay mode with a probability of about 60% is by emitting auger electrons with an energy of 5.19 keV. These electrons have a very low probability to leave the source because of their low energy. Furthermore, there are two K_α decays with a probability of 16.2 % and 8.2 % to release a photon of an energy of 5.899 keV and 5.888 keV, respectively [36]. The energy resolution of the detector in this thesis

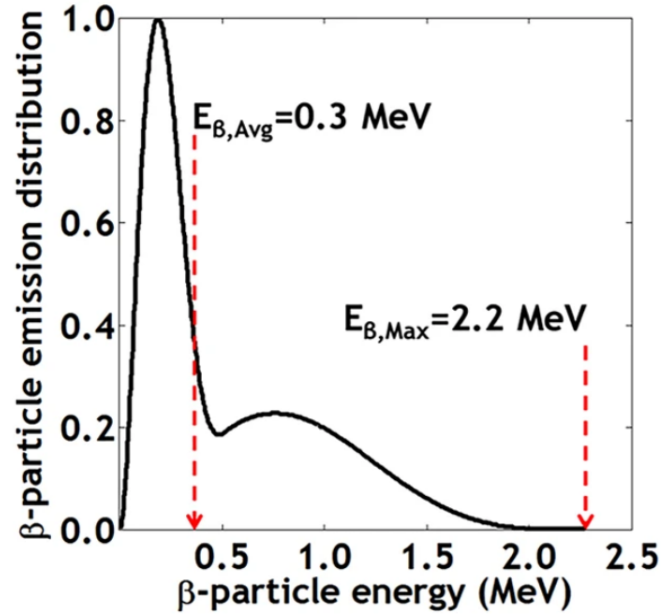


Figure 5.4: Calculated cumulative spectrum for the Sr90 and Y90 decay [35].

can not distinguish these decays as they are very similar in energy. Hence, they can be treated as a monochromatic x-ray source of 5.9 keV. Finally, there is a K_{β} decay with an probability of 2.85% to emit a photon of 6.49 keV [36]. Therefore, the probability of this decay is an order of magnitude less than the K_{α} decays.

5.7 Measuring Diffusion

There are multiple approaches to experimentally verify the impact of diffusion on the signal generation. First, it is possible to study particles traversing the sensor under different angles. By varying the depletion depth and comparing the cluster size to the theoretical expectation under the chosen angle, it is possible to verify if diffusion has an impact on the signal. This approach is taken in a dissertation which is being concluded at the time of this thesis [13]. Second, one can employ multiple sensors of different thickness and investigate differences in their signal response at the same settings. The latter approach is taken in this thesis and is explained in more detail in the following.

Figure 5.5 displays the cross section of an HV-MAPS sensor. The pixels are separated by the pixel guard ring (blue) with the deep n-well centered in the pixel. The depleted substrate, in which a high electric field is present, is shown in grey, while the undepleted substrate is turquoise. Here, it should be noted that in HV-MAPS the bias voltage is applied from the front side via the guard ring (shown in the top part of Figure 5.5). Hence, in HV-MAPS there is always some undepleted substrate at the backside of the sensor. From left to right three different cases of traversing electrons (dashed lines) are represented. The left electron (labeled with 1) enters the sensor under an angle and hence deposits energy in the depleted substrate of two pixels. The ionisation creates electron-hole pairs and the electrons in the depleted substrate move toward the electrode (indicated by an arrow for some of the electrons). The right traversing electron (labeled with 3) hits the sensor perpendicular to the sensor surface close to the area of the pixel guard ring. Therefore,

this particle might also produce a detectable signal in both of the pixels, depending on the amount of charge collected in the second pixel. The straight traversing electron in the middle (labeled with 2) only ionizes the material of one pixel and therefore the created electrons induce a signal only in this pixel. However, all three of the traversing particles create electron-hole pairs by ionization in the undepleted p-substrate. Here, the charges are not in the presence of an electric field and therefore will move via diffusion. If one of these electrons diffuses into the electric field of the depleted volume, it will be collected via drift and contribute to the signal. This charge collection can increase the signal in one of the pixels or help to create a signal in a neighboring pixel.

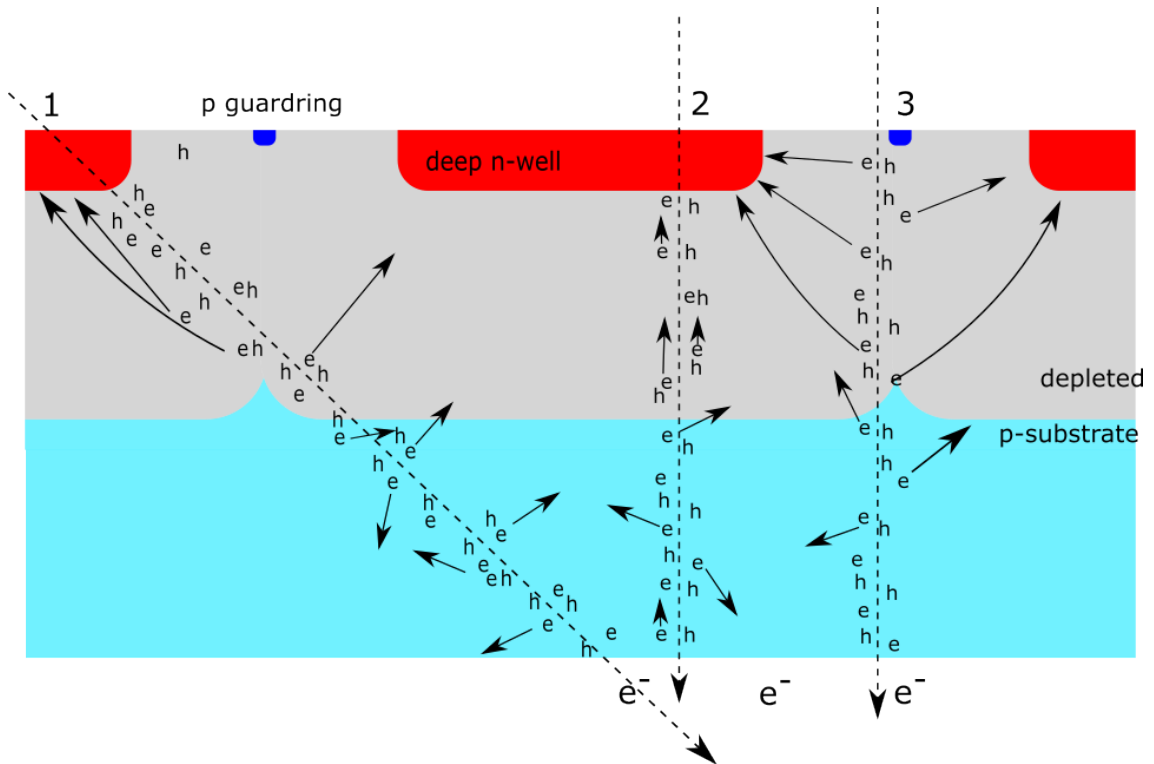


Figure 5.5: Cross section of an HV-MAPS, with the deep n-well in red, pixel guard ring in blue, depleted substrate in grey and undepleted p-substrate in turquoise. Traversing electrons (dashed lines) create electron-hole pairs via ionisation. For some of the created electrons the movement direction is indicated by an arrow [7] (modified).

These considerations lead to the two key observables which will be investigated within this thesis. First, the collected charge in a pixel, which is reflected in the time over threshold (ToT) of the pixel, which is defined in Equation 4.1. Ideally, the ToT should be linearly proportional to the collected charge. Hence, it is a measure of the amount of collected charge in a single pixel and with that also a measure of the amount of charge collected via diffusion. For example, the middle traversing electron (2), which traverses the pixel perpendicular and centrally in Figure 5.5 can be considered. Here, the free charge carriers created in the undepleted substrate could enter the depleted volume of the pixel and then increase the signal amplitude and therefore also the ToT.

The second observable is the cluster size, which is the amount of neighboring

pixels registering a hit in a certain time frame. In the scope of this thesis, this clustering time is set in the analysis to 300 ns if not stated otherwise. The clustering time should not be too long to avoid the counting of a second incident particle as a cluster. Nevertheless, the time scale of 300 ns is chosen rather conservatively in comparison to the expected rates in this study, which are below a 100 Hz per pixel. A cluster size larger than one is possible for multiple reasons. Firstly, the primary particle can enter the sensor under an angle as depicted with the left traversing electron (1) in Figure 5.5. By ionizing the material in the depletion volume of two or more pixels, the cluster size increases. Secondly, a perpendicular traversing particle, similar to the right electron (3) in Figure 5.5, can hit the sensor at the border of two or more pixels. The created charge is shared between the involved pixels and hence increases the cluster size. Furthermore, an example for a cluster size of one is the middle traversing electron (2) in Figure 5.5. The incoming electron hits the pixel centrally and the electrons which are created in the depleted volume are collected only in one pixel. By a careful alignment of the sensor to the particle source, the amount of clusters created by particles traversing the sensor under an angle can be drastically reduced. The second source of larger cluster sizes are the particles which hit the sensor near the pixel border. These are limited by geometrical considerations and should be comparable for all sensors with the same pixel geometry.

However, if diffusion plays a sizable role in the signal generation, the area in which a traversing particle is able to create a signal in the neighboring pixel is increased. This is illustrated by the right traversing electron (3) in Figure 5.5, where a small amount of charge is collected in the neighboring pixel. The charges created in the undepleted substrate diffuse and can increase the signal in the neighboring pixel above the threshold. In the Run2021v2 sensor this possibility is enhanced by the highly asymmetrical pixel dimensions of $25 \times 165 \mu\text{m}$, where the distance between the pixels in row direction is very small. Hence, if a sizable difference in cluster size is observed between sensors of different thickness, it would be evidence for a significant impact of diffusion on the signal.

Next, an estimate of the Gaussian spread of a diffusing point charge is presented to give an idea of the spatial extent of diffusion. The calculation is based on the formulas introduced in subsection 3.4. The Gaussian spread of a point charge is given by:

$$\sigma = \sqrt{2Dt_{\text{diff}}} \quad , \quad \text{with} \quad D = \mu_e \frac{k_B T}{q} \quad (5.1)$$

First, the diffusion constant D is estimated. Within the substrate resistivity range used in this thesis, the electron mobility is only weakly dependent on the resistivity, as there is less than 2% variation in the range from 100 - 1000 Ωcm [37]. However, the mobility is strongly depending on the temperature [4]. Therefore, a relatively large uncertainty is assumed for the electron mobility. The electron mobility is estimated to be $(1450 \pm 100) \text{ cm}^2 \text{ V}^{-1} \text{ s}^{-1}$ for the further calculations. With a temperature of $(300 \pm 10) \text{ K}$ one can calculate the diffusion constant to be:

$$D = (37.5 \pm 2.9) \text{ cm}^2 \text{ s}^{-1} \quad (5.2)$$

Next, the relevant time scale for diffusion has to be defined. In principle, there are two timescales for diffusion in an HV-MAPS. On one hand, there is the rise time of the amplifier, as charge which is collected within this time actively impacts the pulse shaping of the amplifier. Additional charge which is collected within this time

has a strong impact on the signal, as it influences the pulse shaping. On the other hand, there is the measured ToT, as this is the time in which additional charge from diffusion is detectable. Charge which is collected within this time compensates the feedback current and therefore prolongs the signal. Within this thesis, the focus lies on disentangling the amount of charge which is collected via diffusion from the charge collection by drift. Hence the relevant timescale $t_{\text{diffusion}}$ is the ToT. As will be shown later on, the most probable value (MPV) of the ToT ranges from 500 ns to 1000 ns for various signal sources. The Gaussian spread of a point charge can be calculated to range from $(61 \pm 5) \mu\text{m}$ to $(87 \pm 7) \mu\text{m}$ within this time scale.

Nevertheless, the Gaussian spread is also evaluated for the rise time of the amplifier. As the rise time varies from pixel to pixel and with the applied HV, the following calculation gives only an estimate. The rise time is measured with an oscilloscope for a single pixel with the ^{55}Fe source. The definition of rise time for the oscilloscope is the time the signal takes to rise from 10% to 90% of the maximum value. Here, a rise time of approximately 30 ns is observed. With this, a Gaussian spread of $(15.0 \pm 1.2) \mu\text{m}$ is calculated for the rise time of the amplifier.

Lastly, the Gaussian spread for the clustering time of 300 ns is determined. Here, a spread of $(47 \pm 4) \mu\text{m}$ is calculated. This is almost twice the pixel width of $25 \mu\text{m}$ in row direction. Hence, it is evident that the free charge carriers in the undepleted substrate can be collected in a neighboring pixel.

In the course of this thesis, these observables will be compared for sensors of different thickness. The substrate resistivity, applied high voltage and configuration will be the same for all sensors within the comparison. Therefore, all of them have the same depleted volume (see subsection 3.3). As the sensors are on the same settings, they all should reproduce the same signal for a certain amount of collected charge. Hence, if the signal for sensors at same high voltage, same configuration and same substrate resistivity differs significantly for one signal source, it is evidence for the impact of diffusion on the signal.

6 Data Analysis

6.1 Introduction to Corryvreckan

The Corryvreckan framework [38] is a test beam data reconstruction software. It uses a flexible, modular approach to enable customized data analysis. The modular structure of the framework also allows for user contributions, e.g. in the form of event loaders to handle different readout architectures. Moreover, the modular approach also facilitates the characterization of single sensors outside of a test beam setting. Within the course of this thesis two additional custom modules are contributed to Corryvreckan: The ToTAnalyzer and ToTCalibration module. These two modules are explained in detail in section 9 and 10, respectively.

The central element of the Corryvreckan framework is a configuration file which is used to enable certain modules and set parameters for these modules. For each of these modules an event loop for all specified detectors is executed. Each module passes the created reconstruction information to the following modules. In this way all critical information about the interaction of the traversing particle are extracted subsequently. The upper and lower part of Figure 6.1 shows the flowchart for laboratory and test beam analysis for this thesis, respectively. The used modules will be explained in the following.

6.2 Corryvreckan Modules

6.2.1 Metronome

In a data-driven detector, the readout does not require a trigger or event definition. However, as stated above, the data analysis within Corryvreckan is event driven. To overcome the missing event definition, the Metronome module was introduced. It splits the data stream into event frames with an adjustable time frame. For the following analysis a time window of 10 μs is chosen.

6.2.2 EventLoaderMupix

Corryvreckan can not interpret the data of the sensor directly. Therefore, an event loader is needed. It reads in the hit information for every event from the sensor and provides the data as Corryvreckan objects for the following modules. The

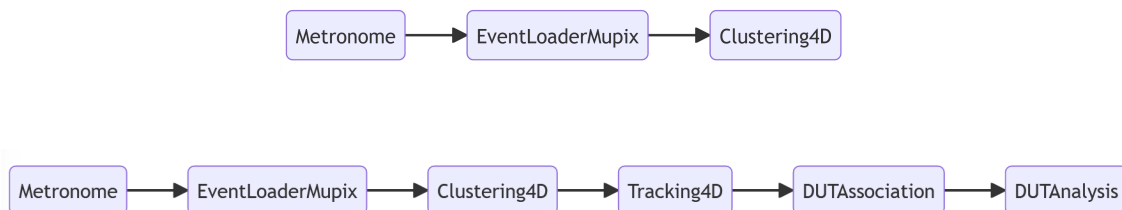


Figure 6.1: The flowchart displays the order of modules within the Corryvreckan configuration file. The one on the top describes the laboratory data analysis, while the one on the bottom describes the basic test beam analysis. For further information see text.

EventLoaderMupix is a common event loader for the sensors developed within the Heidelberg HV-MAPS group. It was originally created to convert the data for the MuPix, but was adapted for the Run2021 sensors. The module creates multiple plots, for example a hitmap and the ToT of the sensor.

6.2.3 Clustering4D

Next, the cluster information is analyzed. Here, for every registered hit in a pixel a time window is defined, the so-called clustering time. The neighboring four pixels are scanned for hits in this time window and if hits are found they are added to the cluster. This process is then repeated for each of the new pixels in the cluster until no more neighboring pixels with hits are found in the time frame. The cluster size is then the amount of connected pixels which registered a hit in this time interval. Furthermore, the cluster charge is defined as the sum of all charge collected in the cluster. However, for the MuPix type sensors there is presently no internal conversion from ToT to collected charge. Therefore, for these sensors the cluster charge is the summed up ToT of all participating pixels. The contribution to the Corryvreckan framework within this thesis enables a fast and precise conversion method from ToT to charge on a per sensor basis for the first time for a MuPix type sensor.

6.2.4 Tracking4D

The following modules are only performed in a telescope environment, where the definition of a track is possible. Here, a telescope consisting out of 4 planes was used in the DESY test beam. A detailed description of the setup is given in subsection 5.5. The Tracking4D module starts with the cluster information and connects all clusters in the first and in the last plane with a straight line, if they are within the specified time frame. Subsequently, the intermediate sensors are scanned for hits within spatial proximity and the time frame of the track and are added if they match. It is possible to specify the minimum amount of hits along the track to filter out false track candidates. In the following, the DUT is always excluded from the track building.

6.2.5 DUTAssociation

Within this module, the clusters on the DUT are associated with tracks which match in time and space. The produced plots allow for a quality control of the matched clusters on the DUT, e.g. providing the hitmap of discarded and matched clusters for a given cut.

6.2.6 AnalysisDUT

Finally, the AnalysisDUT module is executed. The main focus of this module is to gauge the performance of the DUT. It produces plots of the spatial resolution, time resolution and efficiency of the DUT.

III Diffusion

7 Guard Ring Investigation

Before the study of diffusion starts, a guard ring investigation is carried out. As mentioned in subsection 4.4, the Run2021 sensor has two guard rings and hence also two ways to apply the bias voltage. In the following, the functionality and influence on the signal of each of the guard rings is tested for the unthinned sensor with a resistivity of $(370 \pm 20) \Omega \text{ cm}$ used in this thesis.

First, a measurement of the applicable bias voltage is carried out to find the breakdown voltage of the diode. At this point, a small increase of voltage leads to an immense current increase. The break down voltage is determined by the intersection of two linear fits, where one straight line is fitted to the flat part of the curve and the other to the rising part of the curve.

For the measurement, the bias voltage is applied once through the pixel guard ring and once through the chip guard ring. The voltage is scanned in steps of 5 V and for each measured voltage the leakage current is noted after a short setting time. The voltage source is a Keithley 2611B SourceMeter where the leakage current can be read off. The uncertainties of the applied voltage and the measured current are plotted as well, but the uncertainty is too small to be visible. The characteristic IV-curve of the diode is displayed in Figure 7.1 for both guard rings. Here, the current is plotted against the applied bias voltage, with the current on a logarithmic

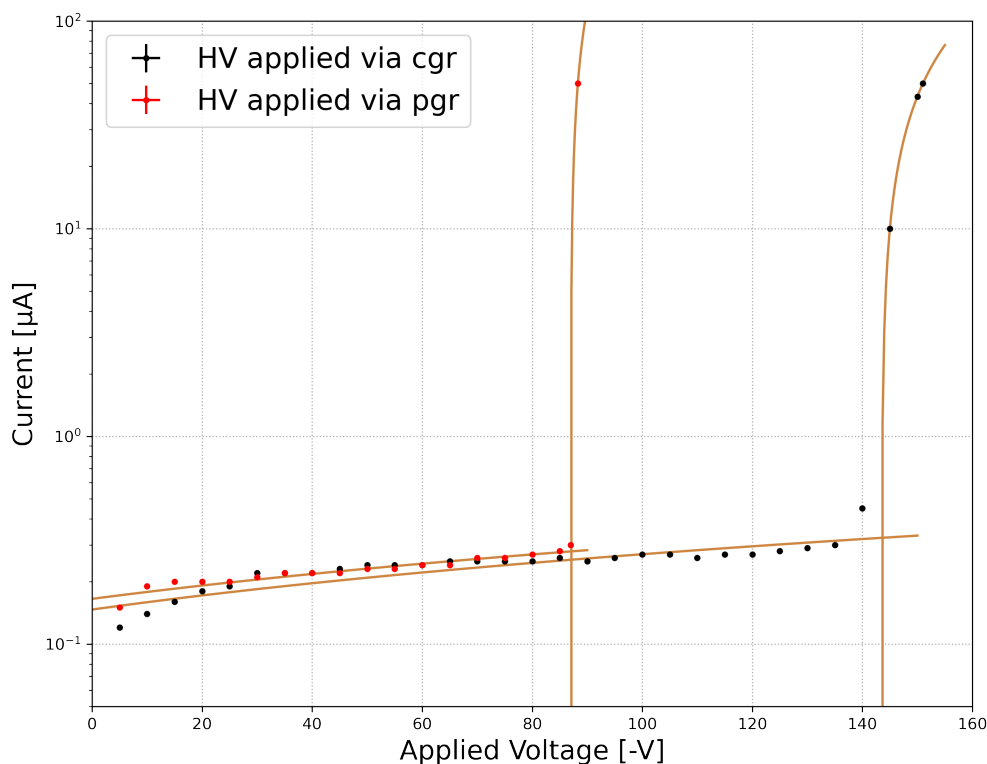


Figure 7.1: Measured leakage current on a logarithmic axis plotted against the applied bias voltage on the chip (black) and pixel (red) guard ring. Straight line fits are used to determine the breakdown voltage.

scale. The data points in red show the IV-curve of the pixel guard ring (pgr), while the points in black show the IV-curve of the chip guard ring (cgr). For bias voltages below -80 V, both of the sensors have comparable leakage current. However, the pixel guard ring (pgr) has a breakdown voltage of about -87.2 V and the chip guard ring (cgr) of -143.6 V for this sensor. Another difference is, that the current on the pixel guard ring rises very suddenly at the point where the breakdown is reached, while the current on the chip guard ring rises less steep.

In a further investigation, the bias voltage is applied on the chip guard ring while measuring the voltage on the pixel guard ring with a multimeter. The result is shown in Figure 7.2, where the applied voltage on the chip guard ring is shown on the x-axis, while the measured voltage on the pixel guard ring is shown on the y-axis. The uncertainties in the measurement arise from the uncertainty of the multimeter. Up to a bias voltage of -20 V both of them agree within the measurement error. At this point, the measured high voltage on the pixel guard ring starts to rise slower than the applied high voltage on the chip guard ring. When the breakdown is reached at -143.6 V, the measured voltage on the pixel guard ring is -88.5 V, indicating that the breakdown still happens due to the pixel guard ring. If the voltage is applied at the pixel guard ring, the measured voltage on the chip guard ring diverges towards lower voltages in the same extend. This behavior can be explained with Figure 4.4, where the placement of the guard rings is depicted. Between the chip guard ring and the pixel guard ring, an additional n-well is placed. Therefore, the two guard rings are not shorted through the surface of the material anymore. As the substrate acts as a resistor, the bias voltage drops between the two guard rings.

Next, the influence of the guard rings on the signal is investigated. For this, the ToT distribution of the ^{90}Sr source is studied. The bias voltage is once supplied through the pixel guard ring and once through the chip guard ring. The applied bias voltage at the chip guard ring is adjusted, so that in both cases the same voltage is measured on the pixel guard ring. For the pixel guard ring a bias voltage of -40 V is chosen, yielding a bias voltage of -48.9 V for the chip guard ring. The ToT distributions are shown in figure 7.3, where the ToT is given in the internal sensor unit least significant bits (lsb) which are equivalent to a time of 8 ns. Hence, the 1024 bits on the x-axis are equivalent to a time of 8192 ns. The distributions are normalized with respect to their entries to allow for comparison. Here, it is clearly visible that in the case of applied voltage on the chip guard ring, the ToT distribution is shifted towards higher values. As the high voltage on the pixel guard ring is the same in both cases, it is concluded that the lateral depletion is the same. However, the depth of the depletion volume is influenced by the larger bias voltage on the chip guard ring. This leads to the visible increase in ToT in Figure 7.3, as more charge is collected via drift in the deeper depletion zone. Hence, within this thesis the bias voltage is always supplied through the chip guard ring, to maximize the depleted volume.

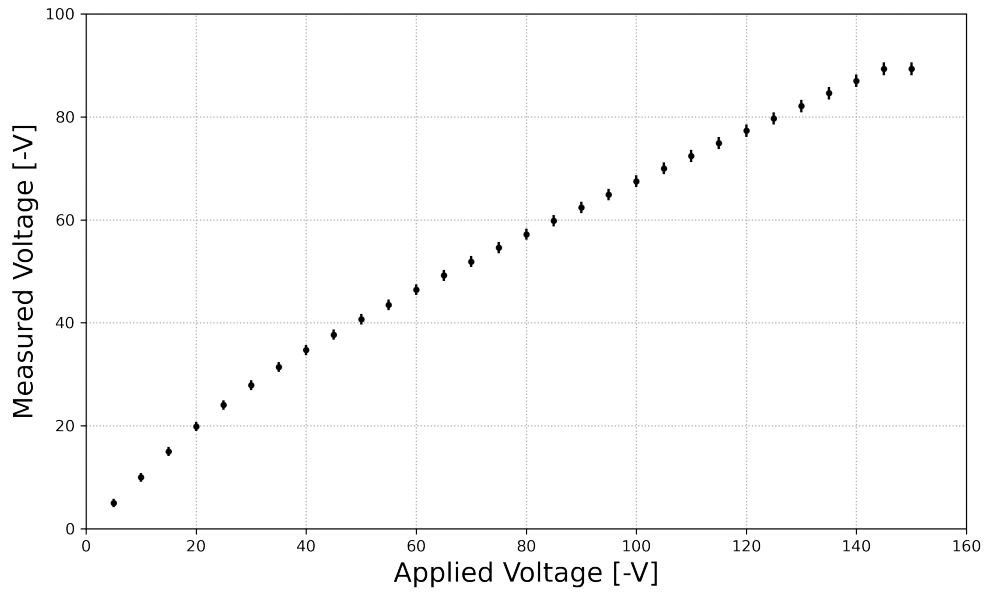


Figure 7.2: Measured bias voltage on the pixel guard ring plotted against the applied bias voltage on the chip guard ring. The two voltages start to diverge around 20 V.

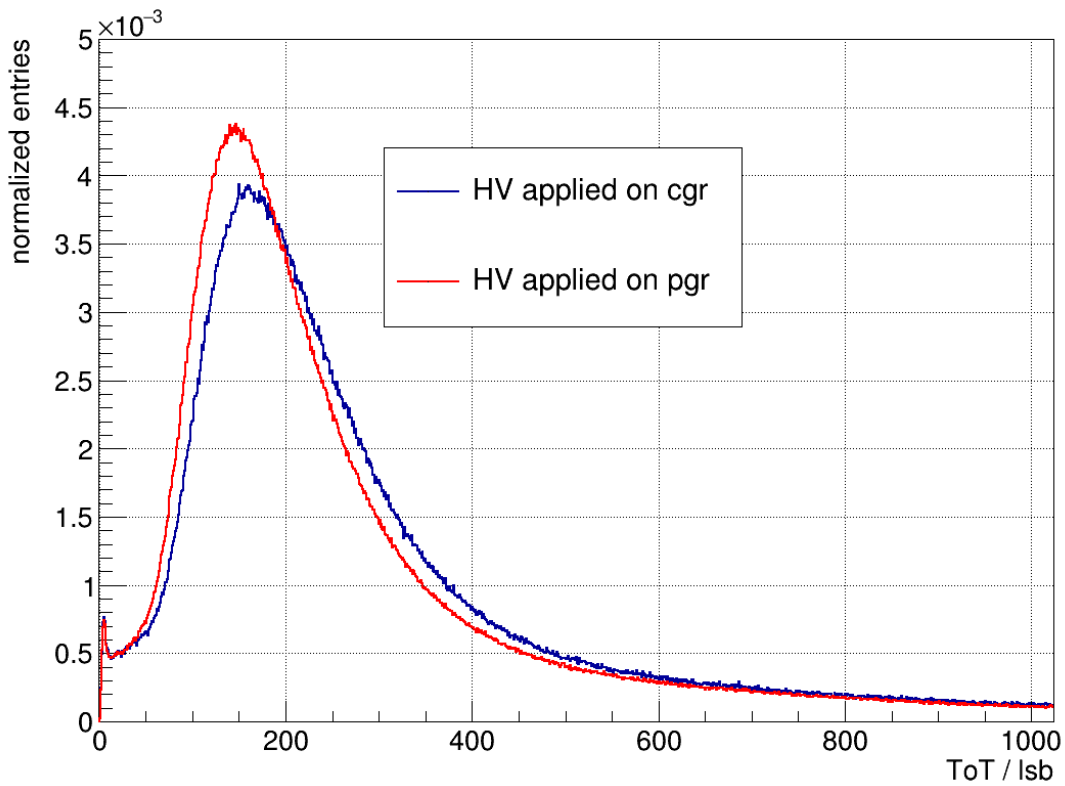


Figure 7.3: Normalized ToT distributions for the ^{90}Sr source for the two guard rings. The applied bias voltage on the chip guard ring (blue) is -48.9 V, while the applied voltage on pixel guard ring (red) is -40 V.

8 Cluster size and ToT

In the following, measurements with three sensors of different thickness (50 μm : ID 350-3-8, 100 μm : ID 350-2-17 and unthinned: ID 350-2-10) are presented. All of them have the same substrate resistivity of $(370 \pm 20)\Omega\text{cm}$ and are operated on the same settings (see Appendix A). In order to achieve the same depletion depth (within the uncertainty of the substrate resistivity), the sensors are biased with the same HV. Therefore, the average amount of collected charge from the depleted volume should be the same for all sensors and any deviation from average should arise from diffusion. For more details on the measurement see subsection 5.7. The measurement is repeated for two bias voltages, at -15 V and -130 V . These points are chosen, as the first one represents the maximum bias voltage which can be applied to the 50 μm sensor and the latter one is the maximum for the 100 μm sensor in stable operation. The depletion depths calculated for these voltages are (see Equation 3.5):

$$w(-15\text{ V}) = (24.0 \pm 0.65)\ \mu\text{m} \quad (8.1)$$

and

$$w(-130\text{ V}) = (70.5 \pm 1.9)\ \mu\text{m} \quad (8.2)$$

The top part of the sensor is covered by metal layers for the routing, which are approximately 16 μm thick [39]. As the deep n-well also extends into the p-substrate, approximately 30 μm of depletable p-substrate are present at this sensor thickness. Hence, at a bias voltage of -15 V , the 50 μm sensor is almost completely depleted. Therefore, the diffusive contribution is negligible. In contrast, both the 100 μm and the unthinned sensor still have plenty of undepleted substrate in which diffusion can occur. At a bias voltage of -130 V , the 100 μm sensor is nearly completely depleted, while the unthinned sensor (which has a thickness of approximately 650 μm to 750 μm) has a plethora of undepleted substrate, allowing diffusion to contribute to the charge collection. In the following, cluster size and ToT will be compared for these sensors, starting with the former one.

8.1 Cluster Size

For the following study, the clustering time cut is set to 300 ns and hits are only added to a cluster if a hit is registered in one of the four neighboring pixels. This procedure is repeated for each pixel added to the cluster until no more hits matching the cuts are found. More information on the clustering can be found in section 6.

First, measurements of the 50 μm and 100 μm sensor, taken at a test beam at DESY, are evaluated. The measurement setup is described in detail in section 5. Figure 8.1 displays the cluster size for both sensors, where the histogram is normalized with respect to its entries for comparison. The average cluster size for the 50 μm sensor is 1.05, mostly consisting of single pixel cluster, with only a small portion of entries having a cluster size of 2. In comparison, the 100 μm sensor has a larger average cluster size of 1.14, with a sizable amount of entries with cluster size 2.

Next, to validate these results, the measurement is repeated in the laboratory, using a ^{90}Sr source. Figure 8.2 shows the cluster size for the 50 μm (blue), 100 μm (red) and the unthinned (green) sensor at a bias voltage of -15 V . A clear increase in average cluster size is observed for the thicker sensors. Both the 100 μm and the unthinned sensor, have almost 20% 2 pixel clusters, while about 10% of the hits

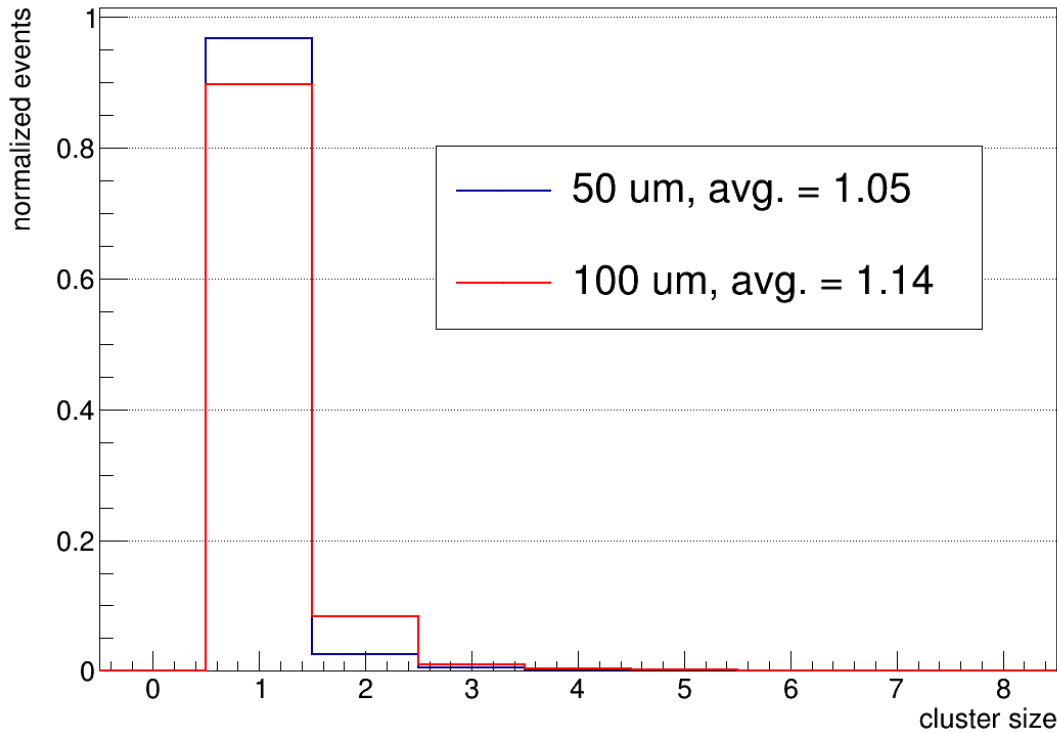


Figure 8.1: Normalized cluster size distribution for all three sensors at a bias voltage of -15 V. The signal source are 4 GeV electrons.

even have 3 or more pixels involved in the cluster, yielding an average cluster size of 1.57 and 1.69 respectively. In contrast, the $50\ \mu\text{m}$ sensor has the lowest average cluster size of 1.21, having more than 80% of hits associated with only a single pixel. Overall, the ^{90}Sr source produces larger cluster sizes than the 4 GeV electrons in the test beam. This phenomenon can be explained by the Berger-Seltzer formula (see Equation 2.2.1, which describes the energy loss of electrons in matter. Here, the monoenergetic 4 GeV electrons are in the logarithmic rising region of the graph (Figure 2.3). In contrast, the energy spectrum of the combined ^{90}Sr and ^{90}Y decay yields mostly electrons below 1 MeV, corresponding to energy losses in the sharply rising part of the Berger-Seltzer formula. As a result, the electrons created by the decay create more electron-hole pairs than the 4 GeV electrons from the test beam.

The high bias voltage case of -130 V is investigated, comparing the $100\ \mu\text{m}$ and the unthinned sensor. Figure 8.3 shows the cluster size for the ^{90}Sr source. Both sensors exhibit a larger cluster size compared to the lower bias voltage for the same source. The relative amount of hits which induce a signal in only one pixel is about 50% for the $100\ \mu\text{m}$ sensor and decreases to 40% for the unthinned sensor. The reason for this is the electric field and depletion depth, which increase with the rising HV. This enlarges the area where charge sharing between pixels leads to an increased cluster size. The unthinned sensor has a larger average cluster size of 2.42, while the $100\ \mu\text{m}$ sensor has an average cluster size of 1.95.

Figure 8.4 shows the time difference between the hit registration of the first pixel in the cluster (called seed pixel), and the second pixel in the cluster for a cluster size of 2. The data is obtained from the same data set as the test beam cluster size

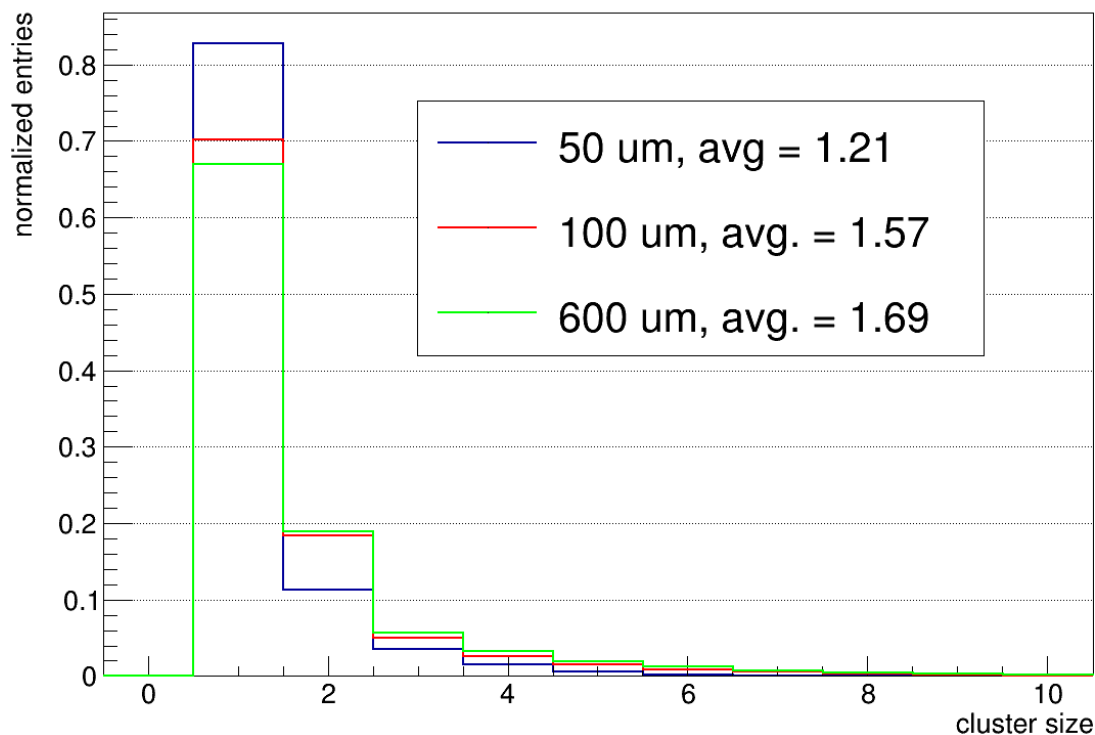


Figure 8.2: Normalized cluster size distribution for all three sensors at a bias voltage of -15 V. The signal source is ^{90}Sr .

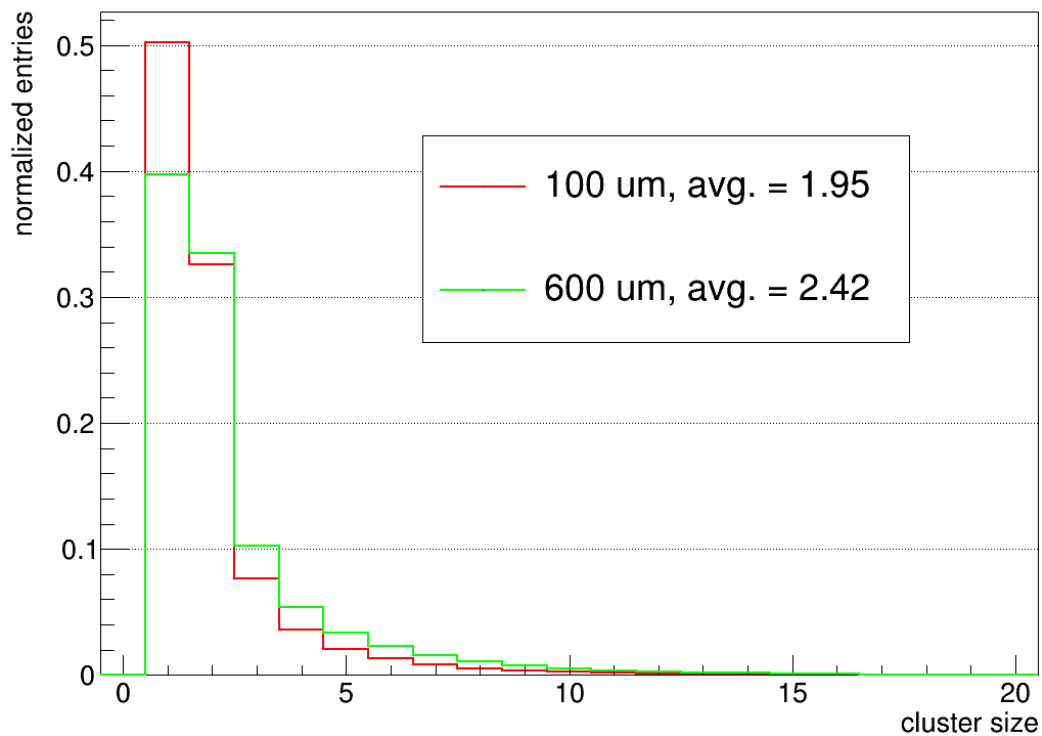


Figure 8.3: Normalized cluster size distribution for the $100\ \mu\text{m}$ and the unthinned sensor at a bias voltage of -130 V. The signal source is ^{90}Sr .

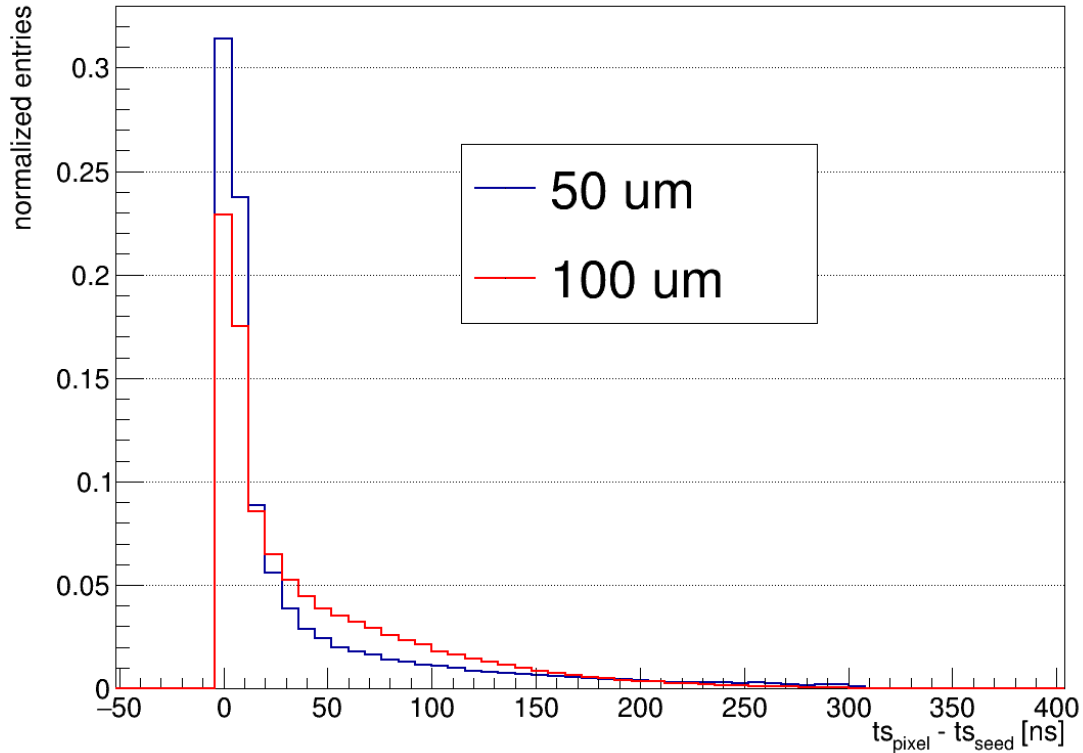


Figure 8.4: Normalized time difference between the seed pixel and the time stamp of the second hit in a cluster of size 2 for perpendicularly impinging 4 GeV electrons obtained in a test beam.

in Figure 8.1 and is normalized with respect to the entries for comparison. Delayed clusters are present in both sensors. The reason for this is the so-called timewalk effect, where a smaller signal crosses the threshold later. This effect can lead to a delay of small signals. Notably, the 100 μm sensor exhibits a larger delay on average between the registration of the hit in the seed pixel and the registration of the hit in the second pixel of the cluster. This larger delay can not be explained by different beam rates, as the beam rate at the DESY test beam facility is consistently lower than 1 Hz/pixel for the Run2021 sensors. Hence, it is concluded, that the excess of delayed clusters originates from diffusive charges which induce a slightly delayed signal in the second pixel of the cluster.

In conclusion, the thicker sensors have higher average cluster sizes in the low bias voltage case for both signal sources. As all sensors are configured in the same way and have the same bias voltage applied, the sizable deviation in cluster size arises from the different thickness. Traversing particles create electron-hole pairs in both the depleted and undepleted substrate. While electrons created in the depleted substrate are collected via drift, electrons in the undepleted substrate move diffusively. The latter ones can enter the depleted volume of an adjacent pixel, contributing to cluster formation. The significant difference in cluster size between the 50 μm and the 100 μm sensor and the comparably small difference between the 100 μm and the unthinned sensor, in the ^{90}Sr measurement, align well with the diffusion explanation. The further away a charge is created the lower is the probability to be collected through diffusion within the time frame of 300 ns. In the high bias voltage case, a

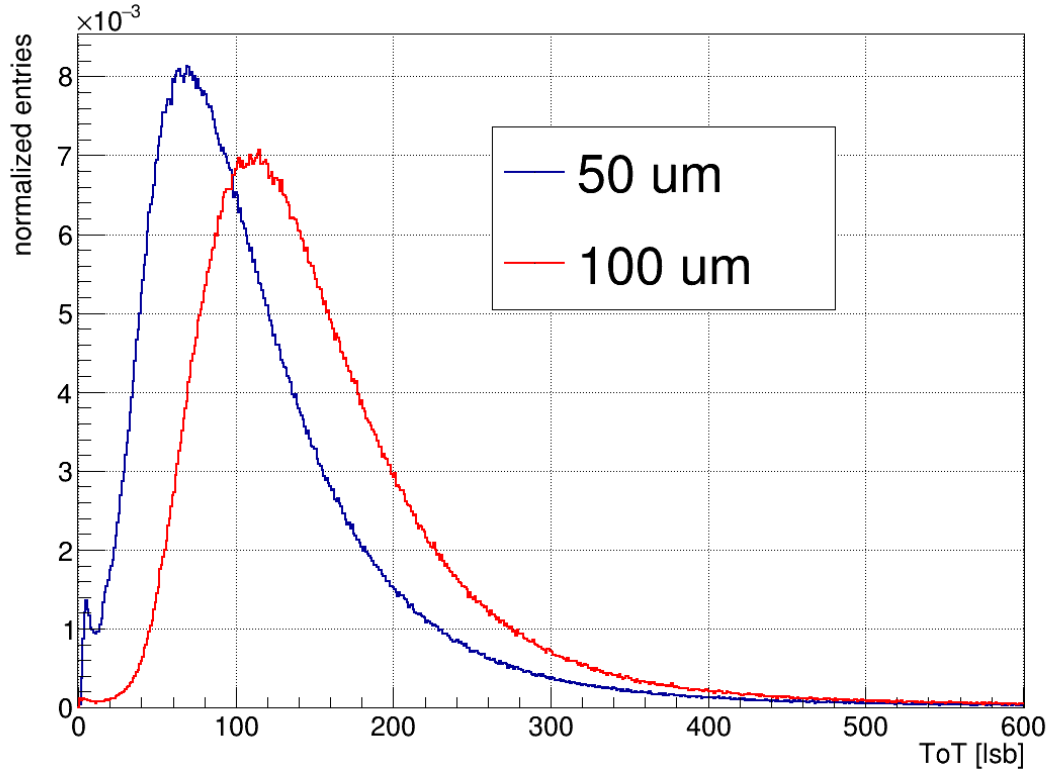


Figure 8.5: Normalized ToT distribution for the 50 μm (blue) and 100 μm (red) sensor at a bias voltage of -15 V . The ToT distribution is given in units of lsb, where every bin corresponds to 8 ns. The signal source are 4 GeV electrons.

sizable difference in the average cluster size is observed between the 100 μm and the unthinned sensor. The thicker sensor has larger average cluster sizes than the thinner, nearly entirely depleted sensor, further supporting the diffusion hypothesis. Additionally, the higher probability of delayed clusters in the 100 μm sensor in the same electron beam can only be explained by diffusion.

8.2 ToT

Since the analysis of the cluster size suggests a sizable influence of diffusion, the investigation is continued by observing the ToT. The presented data originates from the same data set as the cluster size investigation and ensuring identical setup conditions.

First, the ToT distribution measured from the test beam data for a bias voltage of -15 V is depicted in Figure 8.5. The x-axis is represented in least significant bits (lsb) with each bin corresponding to 8 ns. Both distributions are normalized with respect to their entries for comparison. For the 50 μm sensor noise and cross talk are visible at the very low end of the ToT scale. In comparison to the 50 μm sensor, which has its most probable value at 69 lsb, the entire ToT spectrum of the 100 μm sensor is shifted towards higher ToT values. The most probable value of the 100 μm sensor is 115 lsb. The most probable value is shifted approximately by 368 ns (46 lsb).

Next, all three sensors (50 μm blue, 100 μm red and unthinned green) are inves-

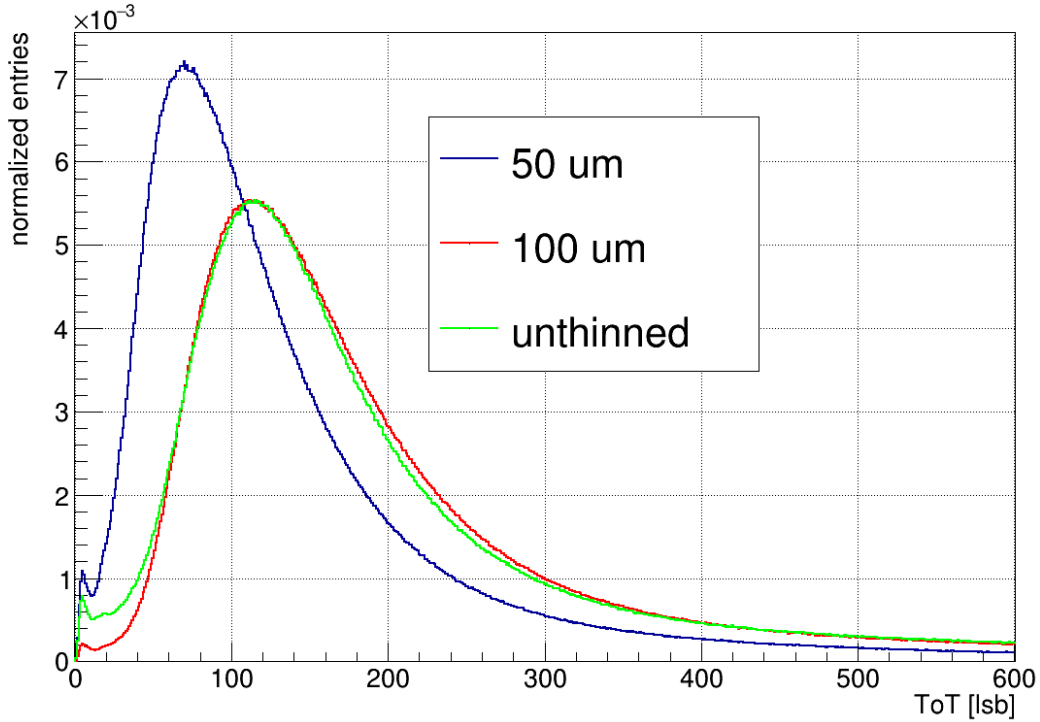


Figure 8.6: Normalized ToT distribution for all three sensors at a bias voltage of -15 V. The signal source is ^{90}Sr .

tigated with the ^{90}Sr source in Figure 8.6. The bias voltage is -15 V. Again noise and crosstalk entries are evident at the lower end of the spectrum for the $50\ \mu\text{m}$ as well as for the unthinned sensor. The most probable value of the $50\ \mu\text{m}$ sensor is 70 lsb, while the most probable value of the $50\ \mu\text{m}$ and the unthinned sensor is 114 lsb. Overall the observed behavior is consistent with the test beam result, with both the $100\ \mu\text{m}$ and the unthinned sensor exhibiting a sizable shift towards larger ToT values. Moreover, the $100\ \mu\text{m}$ and the unthinned sensor have almost identical ToT distributions.

Finally, the ToT distributions for the $100\ \mu\text{m}$ and the unthinned sensor at a bias voltage of -130 V are displayed in Figure 8.7. Here, both sensor have a visible contribution of crosstalk and noise in the lower part of the spectrum. Moreover, both distributions are again almost identical. Overall, the distributions are rather similar to the low bias voltage case of both sensors.

In summary, the ToT distributions of the two thicker sensors are shifted to higher ToT values, compared to the $50\ \mu\text{m}$ sensor. This is a further indication of diffusion playing a significant role in signal generation. In this measurement setup, all sensors should have the same depletion volume and hence on average the same amount of charge should be collected via drift. Therefore, the shift in ToT can be attributed to additional charge which is created in the undepleted volume and enters the depleted volume through diffusion. This charge is then collected rapidly via drift in the electric field of the depleted volume. However, it seems there is no difference between the $100\ \mu\text{m}$ and the unthinned sensor, which is in tension with the measurements of the cluster size. There, in both the low and the high bias voltage case, a difference is visible between the two sensors. Yet, in the case of the ToT the similarity of the two

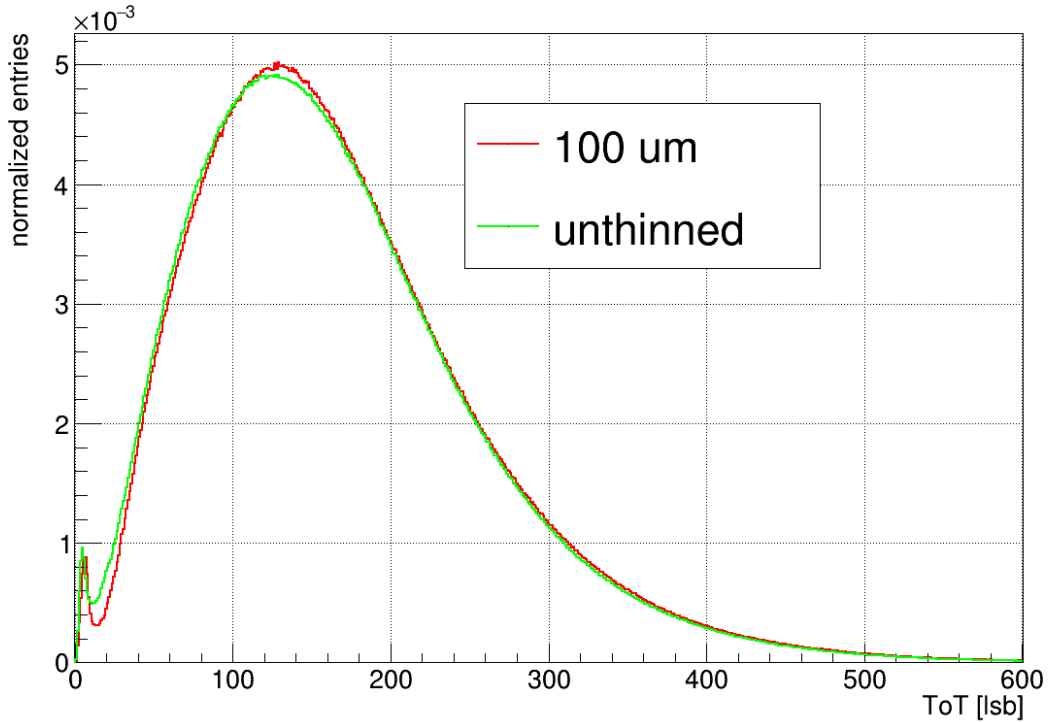


Figure 8.7: Normalized ToT distribution for the 100 μm and the unthinned sensor at a bias voltage of -130 V . The signal source is ^{90}Sr .

distributions could also be a saturation effect of the in-pixel amplifier. The amplifier behavior for large energy depositions in the sensor is known to be non-linear. To disentangle these contributions, a dedicated study is needed.

8.3 Chip Variations

To increase the sample size of the investigated sensors, several unthinned sensors are analyzed. The result of this is shown in Figure 8.8. The sensor labeled with 350-2-10 (green) is the one shown in the previous plots as unthinned sensor. As one of the unthinned sensors has a noisy region for the bias voltage of -15 V , a slightly higher bias voltage of -30 V is chosen for the comparison. All sensors are on the same settings and have a comparable current draw for the low voltage power supply. This is an indication, that the sensors have a similar working point. In principle one would expect these sensors to exhibit very similar ToT distributions. However, this is not the case, as not only the most probable value of the distribution, but also the width of the distribution is different. The most probable value and FWHM of the three sensors are summarized in Table 3. The variation in most probable value and FWHM is about 20%. Moreover, the extend of the tail of the three distributions shows small variations. Similar observations have been made for higher bias voltages as well. This is a concerning information, as these differences only can arise from chip to chip variations. These variations limit the comparability of the ToT distribution.

Chip ID	MPV [lsb]	FWHM [lsb]
350-1-4	102	133
350-2-10	122	156
350-2-12	113	149

Table 3: Most probable value and FWHM for the three unthinned sensors at a bias voltage of -30 V. The signal source is ^{90}Sr .

Chip ID	Average Cluster Size
350-1-4	1.8
350-2-10	1.847
350-2-12	1.821

Table 4: Average cluster size for the three unthinned sensors at a bias voltage of -30 V. The signal source is ^{90}Sr .

If these signal variations arise in the readout chain before the comparator (e.g. in the amplifier), they can influence the cluster size as well. Therefore, the cluster size of the unthinned sensors is compared in Table 4. Here, only a small variation in cluster size is visible. The variation is approximately 3% and hence about one order of magnitude smaller than in the ToT. In the cluster size investigation the cluster size of the thicker sensors is more than 30% larger. It is concluded, that the cluster size is significantly more stable towards the variations than the ToT and hence can be used to quantify Diffusion.

These variations are further investigated in Figure 8.9. Here, for the normalized ToT for the three sensors of different thickness is displayed for the ^{55}Fe source at a bias voltage of -15 V. This source is a monochromatic photon source and hence the response of the sensors ideally should be the same. However, all three sensors show a slightly different most probable value and width in their ToT distribution. Interestingly, the unthinned sensor has the lowest most probable value, while the $100\ \mu\text{m}$ sensor has the highest. This could explain, why in Figure 8.7 no significant difference is visible. However, at this point it is not possible to quantify if this is due to sensor-to-sensor variations or if the signal is dominated by the signal created in the depleted volume.

In summary, chip to chip variations are observed in the ToT spectra. Therefore a direct comparison of ToT distributions for different sensors is very difficult without correcting for these variations. It is suspected, that the differences arise from process variations on the transistor level of the amplifier. Here, especially the feedback of the amplifier is sensitive to variations, as the feedback current is only in the order of $10\ \text{pA}$. As the feedback current determines the falling edge of the pulse, it has a strong influence on the ToT. The cluster size is observed to be more stable than the ToT. It is concluded, that the cluster size can be used to quantify diffusion.

Overall, it is concluded that a sensor calibration is needed in order to compare ToT distributions of different sensors. The necessary steps for this calibration are introduced in the following two sections.

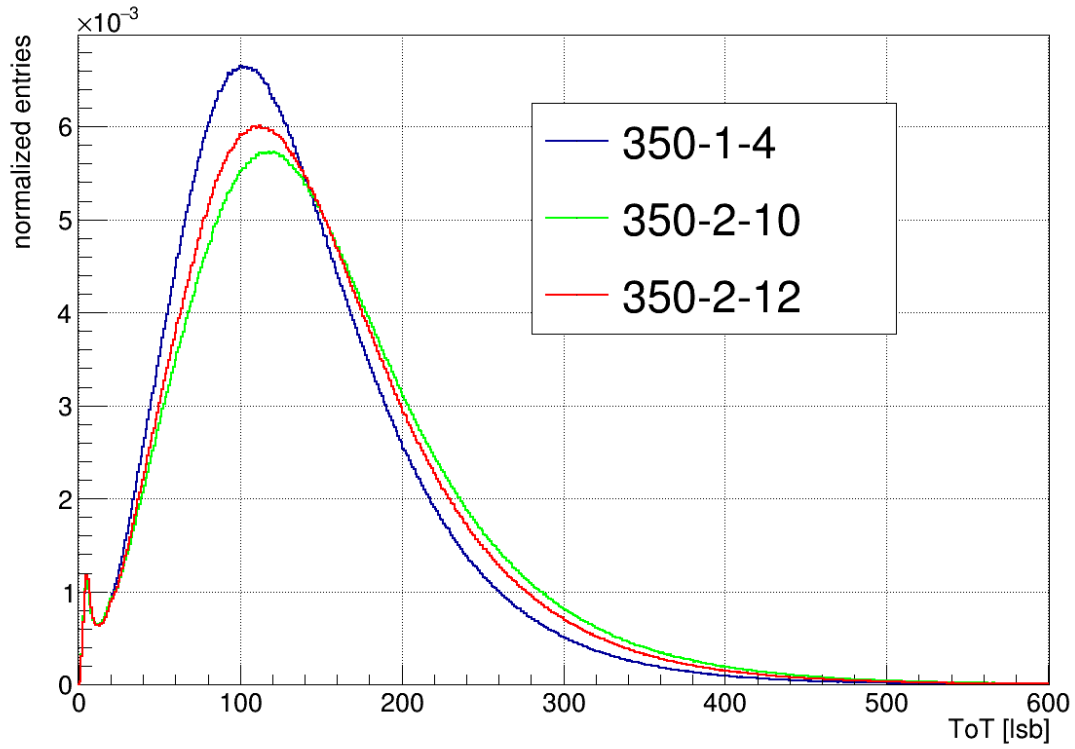


Figure 8.8: Normalized ToT distribution for three different unthinned sensors at a bias voltage of -30 V. The signal source is ^{90}Sr .

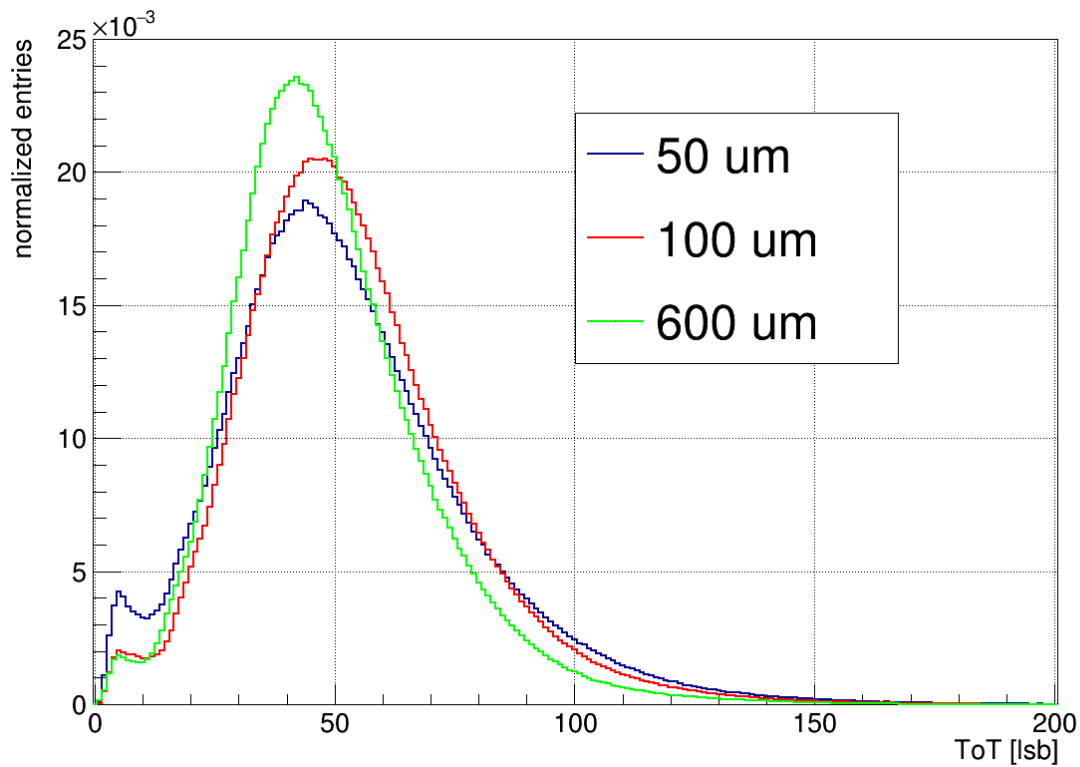


Figure 8.9: Normalized ToT distribution for all three sensors at a bias voltage of -15 V. The signal source is ^{55}Fe .

9 ToT Analysis

As demonstrated in subsection 8.3, the sensor-to-sensor variations are not negligible for the ToT comparison of different sensors. The reason for this fluctuation are process variations due to the node size of 180 nm, as will be proven in subsection 9.3. To overcome this uneven pixel responses, a calibration is needed. To implement this calibration, two custom Corryvreckan modules are introduced in the course of this thesis. The first is the ToTAnalyzer, which is introduced in the following. It is a multipurpose ToT analysis tool on a per pixel level. Moreover, it is possible to cut on the cluster size, e.g. to evaluate only single cluster signals. It is not exclusively written for the Run2021 sensors, but can be used with every pixel sensor which has a ToT information.

9.1 ToTAnalyzer

The ToTAnalyzer is based on the cluster data produced in the Clustering4D module. It extracts the summed up cluster ToT values and creates a distribution for each pixel. Here, the total ToT of the cluster is assigned to the earliest pixel of the cluster which registered a hit. In the ToTAnalyzer, these cluster ToT distributions are statistically evaluated for every pixel. In the following, the necessary definitions are introduced and explained.

9.1.1 Mean

The arithmetic mean is defined in Equation 9.1. The mean μ is the sum of all entries x_i , divided by the number of entries n .

$$\mu = \frac{1}{n} \sum_i^n x_i \quad (9.1)$$

By this definition, the mean is sensitive to outliers. Hence, if many outliers are present, the mean might not represent the core of the distribution anymore.

9.1.2 Mode

The mode of a distribution is simply the most frequent entry of a sample. Therefore, in the case of low statistics, it is rather unstable. Within this thesis the mode is always calculated as a mean of the mode, considering the entries in the three neighboring bins on each side as well. This measure stabilizes it and hence the mean of the mode is a more representative value of the distribution. In the following equation, the mean of the mode is \tilde{m} , the amount of entries in the 7 bins is m and the x_i are the entries in these bins:

$$\tilde{m} = \frac{1}{m} \sum_i^m x_i \quad (9.2)$$

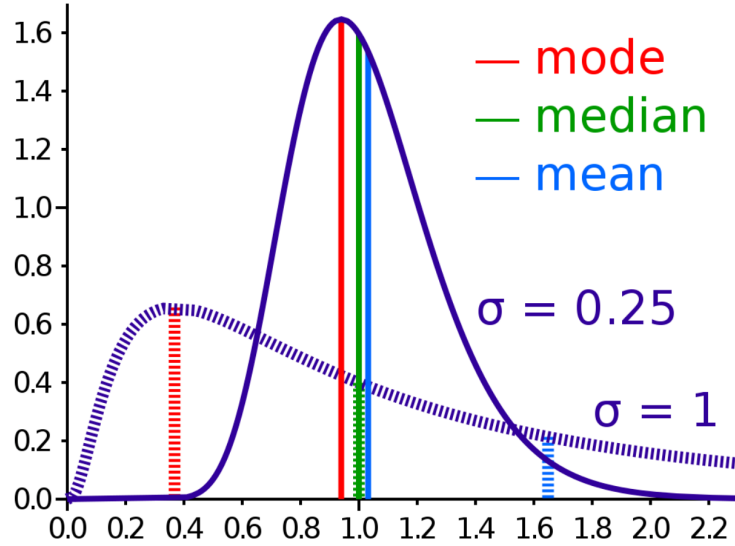


Figure 9.1: An illustration of mean, mode and median for two different log normal distributions [40].

9.1.3 Median

The median m is defined as the number, where the integral of the probability density function (pdf) reaches the value 0.5 and hence satisfies the following equations:

$$F(x) = \int_{(-\infty, x]} f(x') dx' \geq \frac{1}{2} \quad \text{and} \quad F(x) = \int_{[x, \infty)} f(x') dx' \leq \frac{1}{2} \quad (9.3)$$

This integral is also known as cumulative distribution function (cdf) F . Even if outliers are present, the median is stable measure of a distribution. An illustration of mean, mode and median is shown in Figure 9.1, where two log normal distributions with different positive skewness (vide infra) are shown. The distribution drawn with a solid line has a shorter tail and therefore mean, mode and median are close together. In contrast, the distribution drawn with dashed lines has a very long tail and hence mean, mode and median are very far apart. For the Gaussian distribution, mean, mode and median are identical.

9.1.4 Skewness

The skewness (third standardized moment), is a measure of the asymmetry of a distribution. The skewness γ_1 of a random variable X is given by:

$$\gamma_1 = \text{E} \left[\left(\frac{X - \mu}{\sigma} \right)^3 \right] \quad (9.4)$$

With E the expectation operator, μ the mean and σ the standard deviation. Symmetric distributions like the Gaussian have a skewness of 0, while positive (negative) skewness indicates an excess of values larger (smaller) than the mean. The ToTAnalyzer module uses the built in function of the ROOT framework to calculate the skewness.

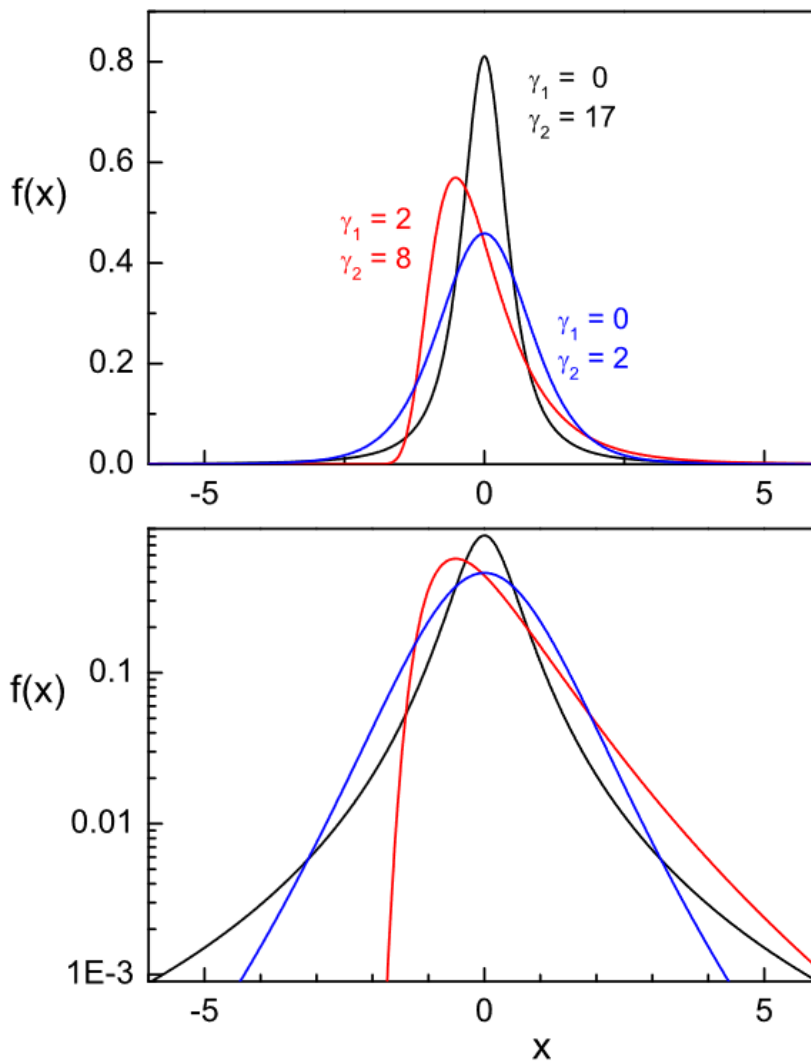


Figure 9.2: Skewness and kurtosis for three distributions with same mean and variance, shown on a linear (top) and logarithmic (bottom) y-scale [41].

9.1.5 Kurtosis

The kurtosis or fourth standardized moment, is a measure of the "tailedness" of a distribution. The kurtosis γ_2 of a random variable X can be calculated as follows:

$$\gamma_2 = E \left[\left(\frac{X - \mu}{\sigma} \right)^4 \right] \quad (9.5)$$

One important value is the kurtosis of the Gaussian distribution, which is 3. This information allows to compare distributions in terms of their "tailedness" to the Gaussian distribution. Hence, it is useful to define the so-called excess kurtosis which is given by:

$$\gamma_2^{\text{Excess}} = \gamma_2 - 3 \quad (9.6)$$

The excess kurtosis of a Gaussian is 0, facilitating an easy comparison of a distribution to a Gaussian. Again, the built in function of ROOT [42] is used for the

calculation.¹ Both the kurtosis and the skewness are illustrated in Figure 9.2, where three distributions with the same mean and variance are depicted. The blue and the black distribution are symmetric and therefore have a skewness of 0. However, the distributions vary in their kurtosis. In the logarithmic scale it is clearly visible, that the black distribution has more pronounced tails and a sharper peak. This is reflected in the high kurtosis of 17 of the black distribution, while the blue distribution with a kurtosis of 2 is close to the normal distribution. Finally, the red distribution is an example of a positively skewed distribution and therefore exhibits an asymmetry.

9.1.6 FWHM

The Full Width at Half Maximum (FWHM) is the width of the distribution at half the amplitude. It is a common measure for the width of a distribution. For the Gaussian, the following relationship can be derived:

$$\text{FWHM} = 2\sqrt{2\ln(2)} \approx 2.355\sigma \quad (9.7)$$

9.2 Calibration Method

In a first approach, the calibration will use the ^{55}Fe signal of every pixel to linearly gauge the sensor response to the number of electrons created. As stated in subsection 5.6, ^{55}Fe emits photons of two energies. If one takes the probabilities of these decays into account, an average weighted photon energy of 5.895 keV is calculated. The average energy needed to create an electron-hole pair in silicon is 3.65 eV at 300 K (see Table 1). However, this energy is temperature dependent [43]. A simulation carried out for photons of 5.9 keV indicates an average energy to create an electron-hole pair of (3.65 ± 0.01) eV at a temperature of (300 ± 10) K for silicon [44]. Hence the number of electron-hole pairs created from the ^{55}Fe source is calculated to be:

$$(1615 \pm 16)e \quad (9.8)$$

For the calibration, a linear relationship between the deposited charge and the ToT of the signal is assumed.

In practice this means either the mean, mode or median of the ^{55}Fe signal have to be extracted for every pixel. In a further step, a calibration function has to be chosen. This calibration then can be applied to the ^{90}Sr or test beam signal. The further details of the calibration are explained in section 10. In the subsequent subsection the signal of ^{55}Fe is carefully evaluated on a per pixel basis to gain a better understanding of possible uncertainties in the calibration process.

¹The "GetKurtosis" function does **not** calculate the kurtosis, but the so-called excess kurtosis.

9.3 ^{55}Fe in the ToTAnalyzer

The relationships and observables defined in subsection 9.1 can now be utilized to investigate the signal of ^{55}Fe on a pixel-to-pixel basis. As an example, high statistic data sets with about 10 000 entries per pixel are taken and analyzed for the unthinned sensor with bias voltages of -15 V and -130 V . Each pixel has about 10 000 entries, allowing a precise analysis on a per pixel basis.

9.3.1 Single Pixel ToT and Energy Resolution

First, an example ToT distribution for a single pixel is evaluated. Figure 9.3 shows the ToT distribution of pixel 10/10 with a Gaussian fitted to the core of the distribution. Again the ToT is given in the internal unit of the sensor, least significant bits (lsb) corresponding to 8 ns. The Gaussian fit is chosen, as it describes the expected (non-ideal) pixel response for a monochromatic source like ^{55}Fe . However, there are outliers towards the lower part of the ToT. These low ToT entries can be explained by charge sharing between pixels and charge depositions at the interface of the sensitive material (i.e. the depletion volume) and the insensitive material on top of the silicon.

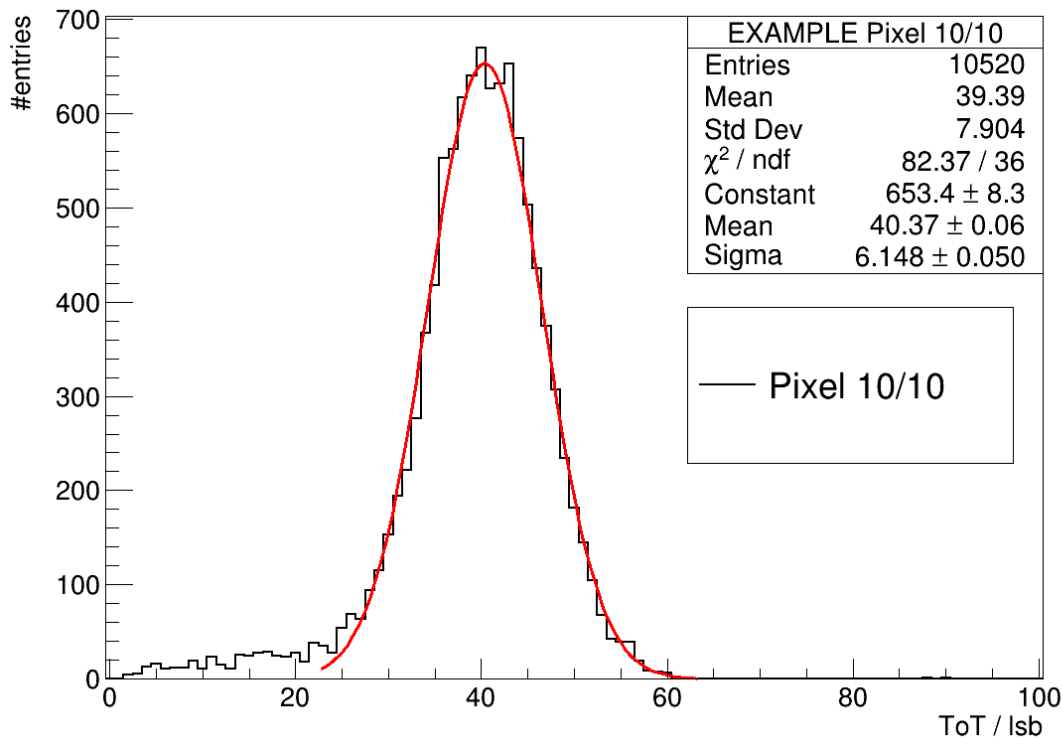


Figure 9.3: ToT distribution of a single Pixel of the sensor (pixel address 10/10) for ^{55}Fe at a bias voltage of -15 V . The ToT is given in units of lsb, corresponding to 8 ns. A Gaussian is fitted to the core of the distribution.

From the fit parameters of the Gaussian distribution the energy resolution of a single pixel after the full readout and analysis chain can be estimated. The calculation yields an energy resolution of:

$$\frac{\sigma_E}{E} = (15.23 \pm 0.13)\% \quad (9.9)$$

This uncertainty includes the noise overlaying the signal, the uncertainty arising from the Fano factor [45] and the combination of uncertainties induced by the read-out circuit. Within the calculated energy resolution the second K_β photons² can not be resolved. This deteriorates the energy resolution further, as the K_β decay broadens the spectrum. However, there is a small excess of entries on the right side of the peak of the Gaussian fit. This second peak is exactly at the position, where one would expect the 6.49 keV photon. Hence, this might be an indication for the secondary peak of ^{55}Fe . However, at this point, a statistical fluctuation also can not be excluded. For higher bias voltages an even better energy resolution can be obtained. This is shown in Figure 9.4, where the Gaussian fit yields a resolution of:

$$\frac{\sigma_E}{E} = (13.09 \pm 0.12)\% \quad (9.10)$$

Here, in contrast to the low voltage case, the ToT distribution has a tail towards larger ToT values. This can be explained by the electric field distribution within the sensor. At this high voltage, the electric field is sufficient to accelerate electrons to a velocity where they can produce secondary electron-hole pairs. However, the amount of entries overall is rather small, indicating only a small region of the pixel exhibits these very large electric fields. This behavior is investigated in more detail at the end of this section.

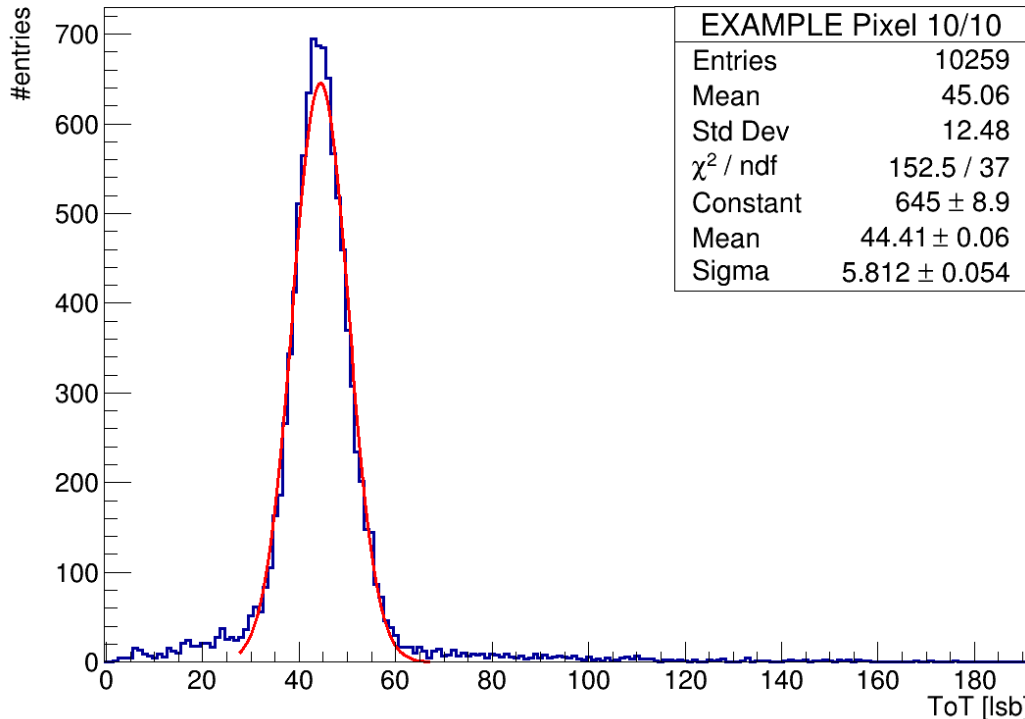


Figure 9.4: ToT distribution of a single Pixel of the sensor (pixel address 10/10) for ^{55}Fe at a bias voltage of -130 V . A Gaussian is fitted to the core of the distribution.

²These photons have an energy of 6.49 keV and are one order of magnitude less frequent. They have approximately 10 % more energy than the dominant photons of averagely 5.895 keV.

9.3.2 Bias Voltage of -15 V

In the following a detailed statistical analysis of all pixels of the sensor is presented for a bias voltage of -15 V . First, the example ToT for a single pixel is compared to the ToT of the full sensor in Figure 9.5. Both ToT spectra are normalized with respect to their entries to allow for comparison. While the single pixel has a FWHM of 13 lsb (104 ns) and has an almost perfect Gaussian shape at its core, the ToT distribution of the full sensor has a FWHM of 39 lsb (312 ns). The reason for this broadening of the spectrum is the superposition of the individual pixel responses. The contrast of the two spectra supports the initial assumption, that the chip to chip differences observed in Figure 8.8 emerge from process variations of the individual pixels. Nevertheless, for a better understanding of these variations, a detailed study of the pixel-to-pixel variations in their ToT spectra is presented for the sensor. Furthermore, in foresight of the overarching goal, these investigations will facilitate a more precise understanding of the calibration process.

The mean, mode and median distribution of the sensor are investigated in the following. Figure 9.6 displays the median of the ToT on a per pixel basis. Each entry corresponds to the median value of the ToT distribution of one pixel given in lsb. In principle, the median of the ToT distribution should be a stable measure to characterize the ToT of the pixel as it is only lightly influenced by outliers or statistical fluctuations. Here, it is immediately visible that the pixel response varies over a large range. Especially towards large median values a rather long tail is visible, where some pixels even have a median about a factor 3 higher than the most

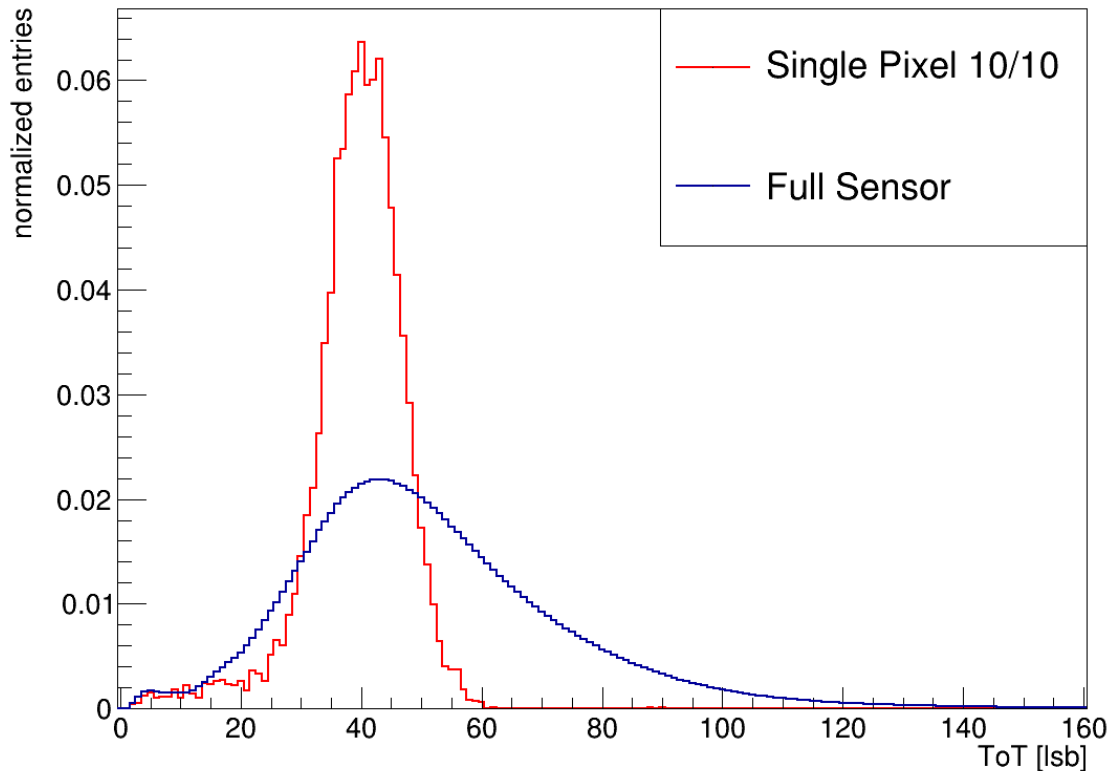


Figure 9.5: ToT distribution of the full sensor (blue) and a single pixel of the sensor (red) for ^{55}Fe , each normalized with respect to their entries.

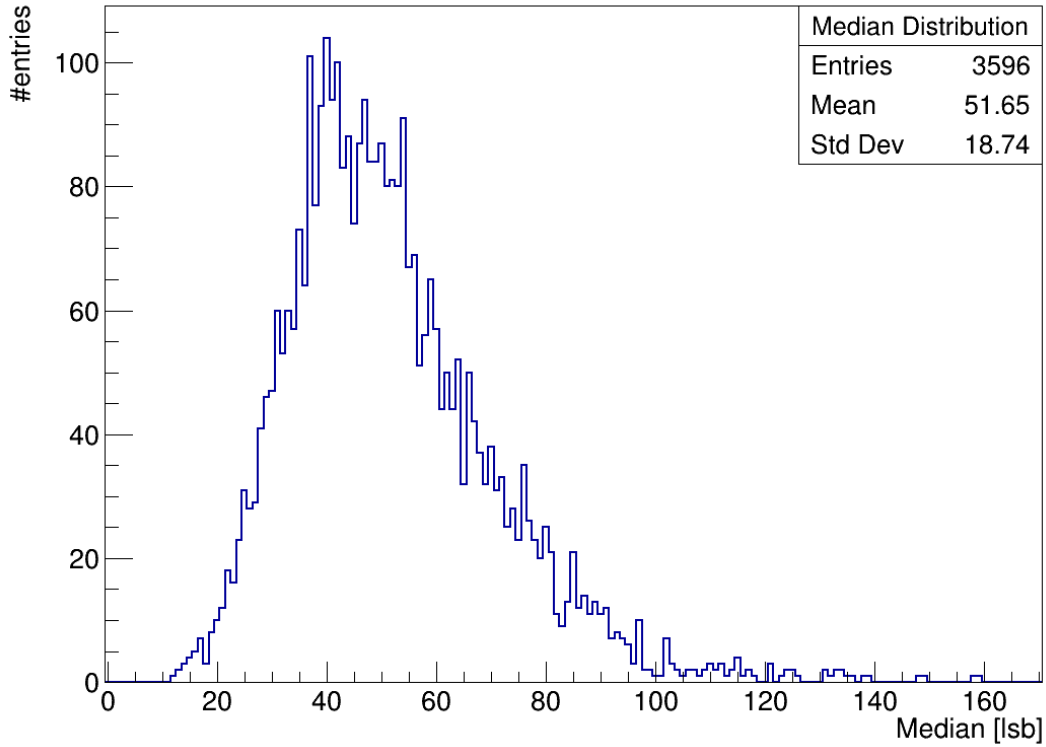


Figure 9.6: Median of the ToT distribution on a per pixel basis for ^{55}Fe . Every entry corresponds to the median of the ToT distribution of a single pixel.

probable value of the distribution. Moreover, the FWHM of the median distribution is rather broad, indicating sizable variations in pixel response for a large part of the sensor. Figure 9.7 shows the same behavior for the mean (left) and the mode (right). Overall, mean, mode and median distribution are similar in shape but have slightly different mean, indicating the underlying ToT distributions are close to a Gaussian distribution.

To further investigate the relation of the ToT distribution of the individual pixels to a Gaussian, skewness and excess kurtosis are investigated. The skewness distribution of the pixels is shown in Figure 9.8. The center of the distribution is slightly below 0, indicating a slight asymmetry for the majority of pixels with an excess of

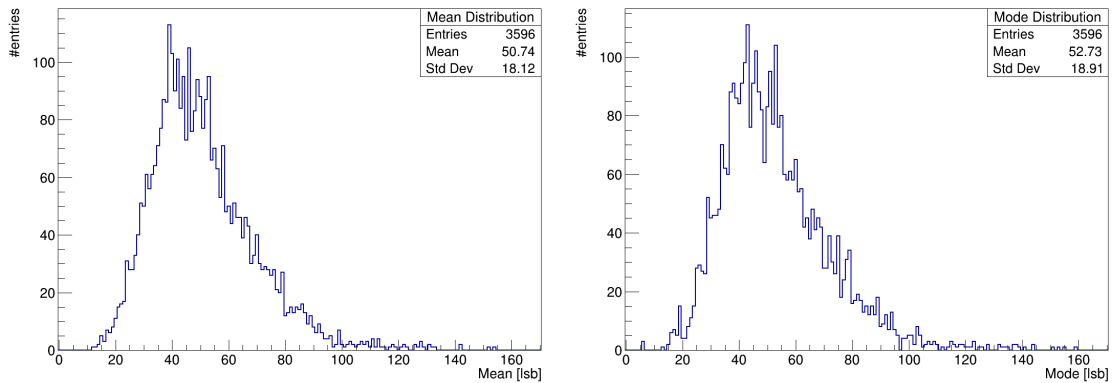


Figure 9.7: Mean (left) and mode of the ToT distribution of every pixel for ^{55}Fe .

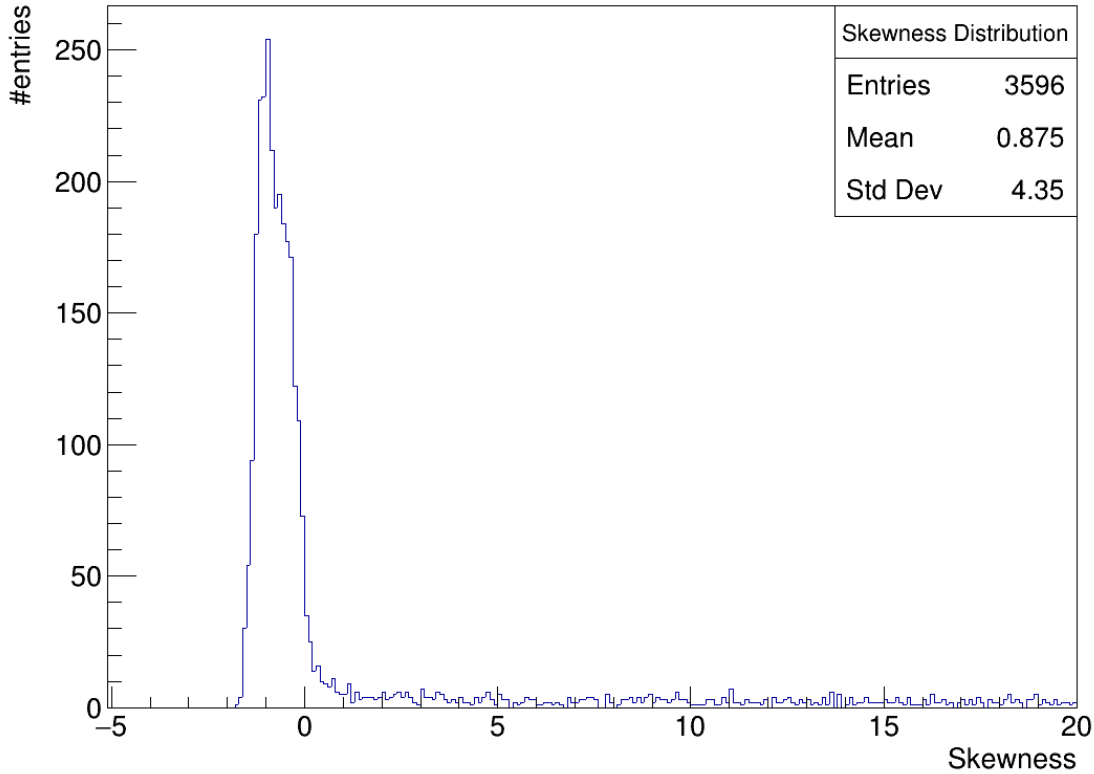


Figure 9.8: Skewness distribution of the ToT of every pixel for ^{55}Fe .

entries towards lower ToT values. These low ToT entries are probably induced by charge sharing between pixels and energy depositions at the surface of the sensitive material, where the energy is partly deposited in insensitive material. Therefore, it seems the randomly selected pixel in Figure 9.3 represents the majority of pixels on the sensor. However, in the skewness distribution a long tail to high skewness values is visible, which even exceeds the displayed range. To investigate this, the ToT distributions of three single pixels with large skewness are evaluated. In each of the ToT distributions of the three pixels a single entry is at around 1000 lsb, while the distributions are very similar to the one discussed in detail in Figure 9.3. This outliers increase the skewness dramatically. Therefore, it is suspected, that a small amount of outliers at very large ToT values is responsible for the tail towards large skewness values.

Figure 9.9 displays the excess kurtosis distribution on a per pixel basis. The distribution deviates from the value expected for a Gaussian, as basically all pixels have an excess kurtosis larger 0. The majority of entries lies between 0 and 6, indicating that the ToT spectra have more pronounced tails than a Gaussian. This is in agreement with the observations in single pixel ToT and the skewness, where tails towards low ToT values are observed. Nevertheless, similar to the skewness distribution, the excess kurtosis distribution has a large tail to values of high excess kurtosis. As the excess kurtosis is even more effected by outliers, it is again suspected, that single outliers at very large ToT values are responsible for this effect. To investigate if this effect is localized, the skewness and excess kurtosis of each pixel are shown in a map in Appendix B in Figure B.1 and Figure B.2. Here, no localization of the high skewness and excess kurtosis values is observed.

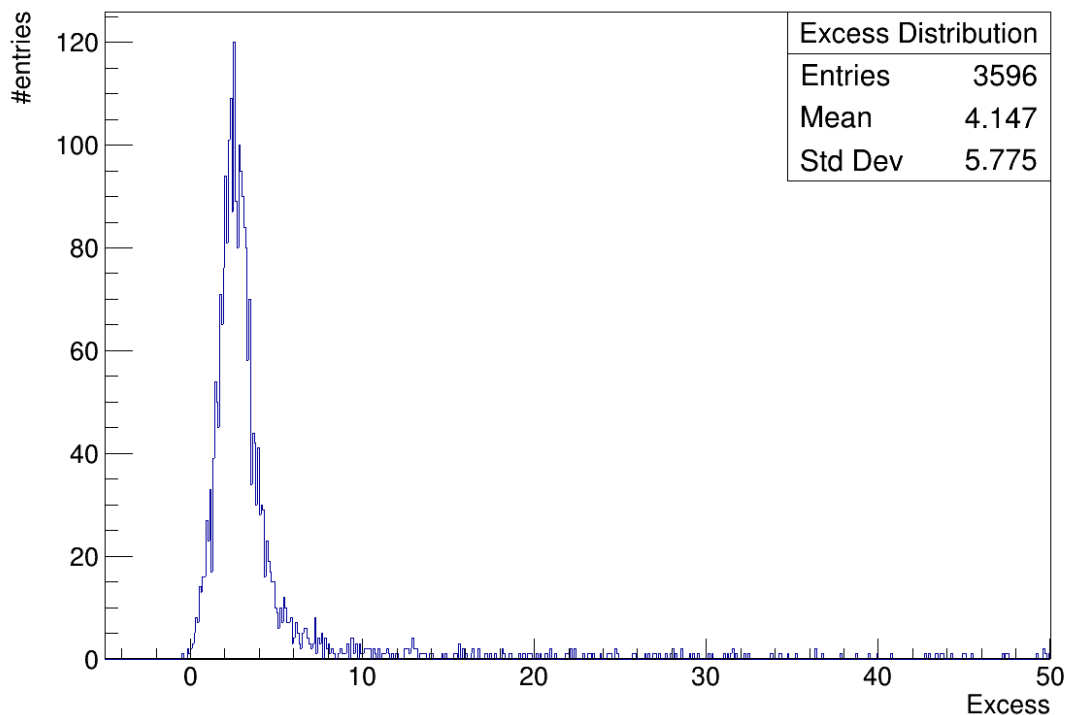


Figure 9.9: Excess kurtosis of the ToT distribution of every pixel for ^{55}Fe .

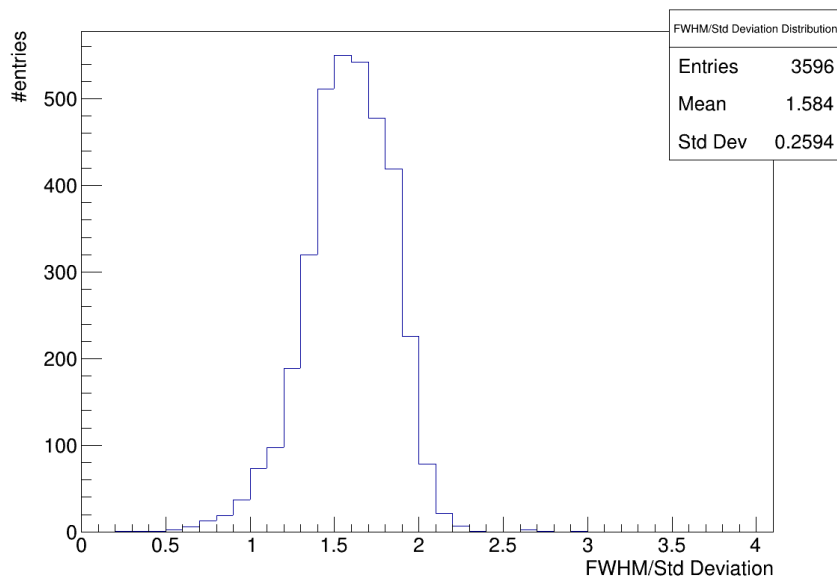


Figure 9.10: Ratio of the FWHM to the standard deviation of the ToT distribution of every pixel for ^{55}Fe .

Subsequently, the ratio of FWHM to standard deviation of the single pixel ToT is shown in Figure 9.10. Again it is possible to use this distribution to compare the ToT of the individual pixels to a Gaussian distribution. For the latter, a ratio of approximately 2.355 would be expected. Here, it is clearly visible, that the ratio of FWHM to standard deviation is smaller, as the mean of the distribution is 1.584. This can be explained by the long tails in the ToT distribution, which are visible in the single pixel ToT (Figure 9.3) and are expressed in the negative skewness

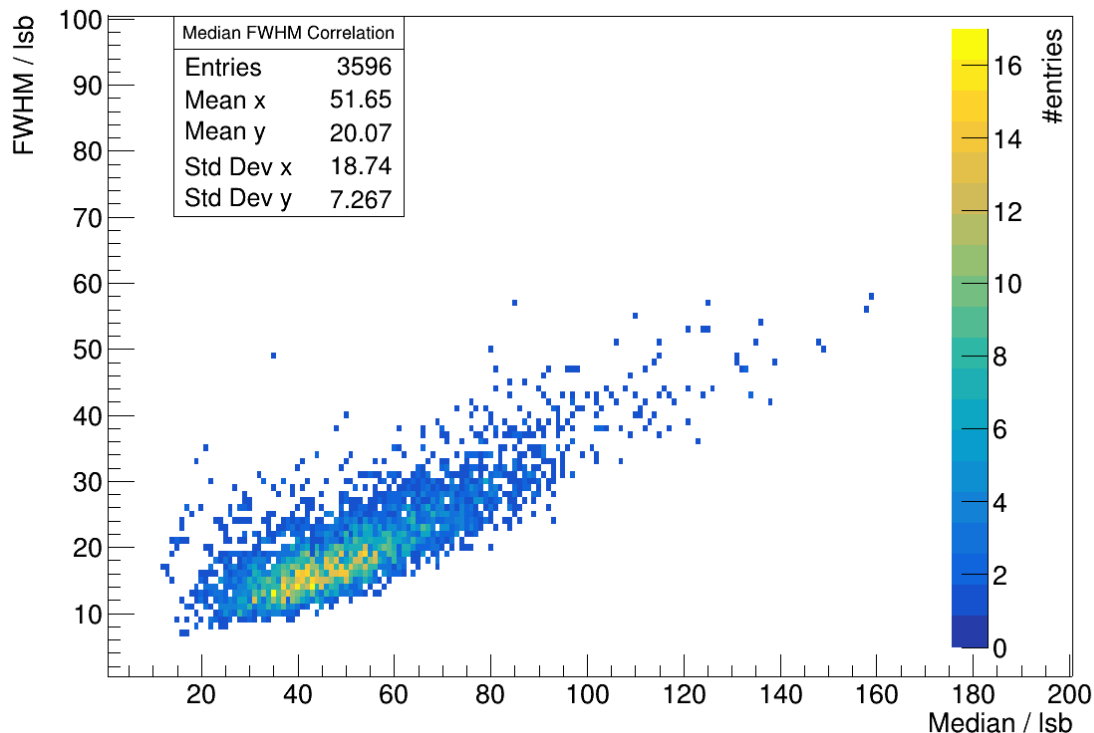


Figure 9.11: Correlation between the FWHM and the median of the ToT distribution on a per pixel basis for ^{55}Fe .

of the majority of pixels (Figure 9.8). These tails are effectively outliers, which influence the standard deviation rather heavily. Therefore, the standard deviation is comparably large, which is shifting the ratio to lower values.

Finally, a scatter plot is depicted in Figure 9.11, which shows the correlation between the FWHM and the median of the single pixel ToT distribution. While an overall linear correlation between FWHM and median is visible, outliers are present. These are more pronounced towards large FWHM. Moreover, the color coding indicates that a large part of the pixels has a similar response in median and FWHM with respect to each other. Nevertheless, the amount of outliers with very high median or large FWHM is sizable. The median ranges approximately from 15 to 150 lsb (corresponding to a range of 120 to 1200 ns), while the FWHM ranges from 10 to 50 lsb (corresponding to a range of 80 to 400 ns). Hence, the ToT of the monochromatic signal of ^{55}Fe varies strongly from pixel-to-pixel, indicating a strong variation in the signal shaping of the amplifier. Overall, the correlation plot shows why a calibration is required to compare the response of different sensors to each other. It summarizes the difference in pixel response by showing the large spread of median and FWHM. The goal of the calibration is to minimize this spread, enabling a precise comparison of the signal response.

9.3.3 Bias Voltage of -130 V

As a cross check and to investigate the tail towards large ToT values which is detected in Figure 9.4, a short complementary study of the ^{55}Fe signal at a bias voltage of -130 V is presented. First, a comparison of the single pixel ToT distribution for both bias voltages is shown in Figure 9.12. Here, two deviations are visible. Firstly, the tail towards higher ToT values, which is already observed in Figure 9.4. Secondly, for the larger bias voltage the ToT distribution is shifted towards higher values. This shift can not be derived from additional charge collection in the deeper depletion depth, which is caused by the higher voltage, as the photon from ^{55}Fe deposits all its energy in a very small volume. Hence, the difference in the signal arises from the signal processing. Here, the amplifier is influenced by the change in pixel capacity. The capacity is inversely proportional to the depth of the depletion zone and hence also to square root of the applied HV. The smaller capacitance increases the signal.

Regarding the tail towards large ToT values which is visible in the high bias voltage case, a coarse measurement series with different bias voltages in steps of 20 V is performed, to identify at which voltage the tail emerges. Figure 9.13 shows the pixel with address 10/10 at a bias voltage of -100 V . Here, the outliers toward larger ToT arise.

To further investigate this tail, the skewness distributions for both bias voltages are compared in Figure 9.14. In the low bias voltage case, the majority of pixels has skewness of slightly below zero, originating from the entries at low ToT. In contrast, the skewness at a bias voltage of -130 V is larger than 0 for all pixels. Therefore it is interpreted, that at this bias voltage the electric field reaches very high values in some areas of the pixel, leading to outliers in the high ToT region, which outweigh

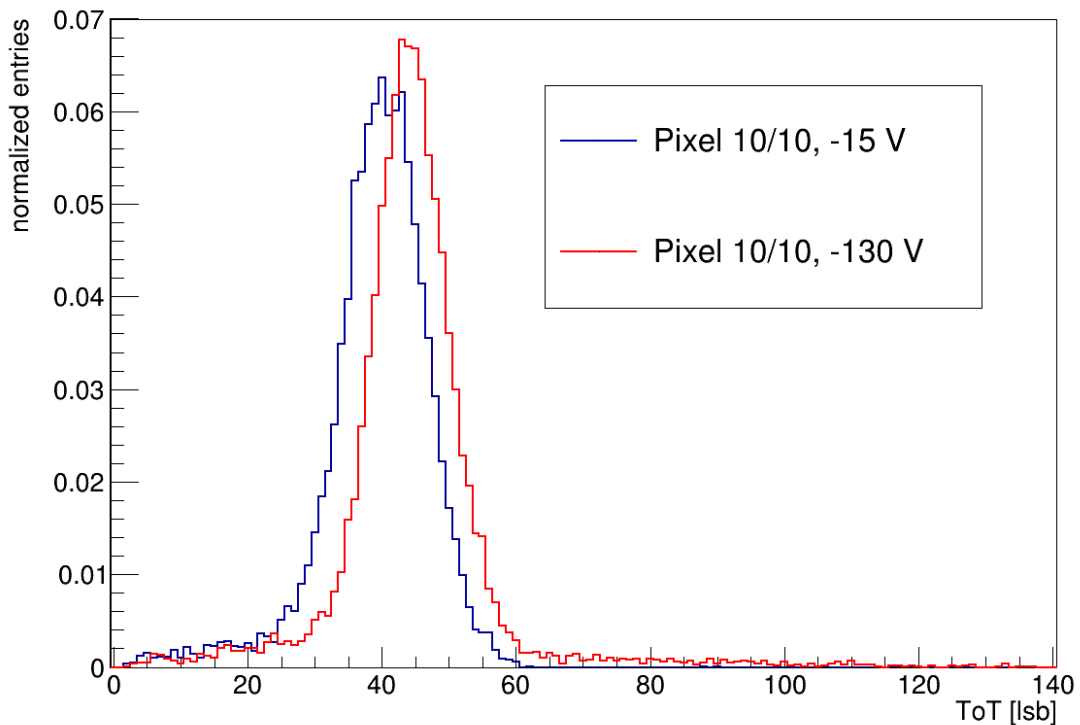


Figure 9.12: ToT distribution for ^{55}Fe of a single pixel (pixel address 10/10) at a bias voltage of -15 V (blue) -130 V (red) for ^{55}Fe .

the low ToT entries in the skewness. These areas of high electric field are most likely located at edges, where the electric field is largest. Moreover, areas near the pixel guard ring might also exhibit large electric fields. As shown in section 7, the HV on the pixel guard ring is close to the breakdown voltage for a bias voltage of -130 V on the chip guard ring.

Next, the ratio of FWHM to standard deviation is depicted in Figure 9.15. The ratio has a mean of approximately 0.9, deviating even more from the ratio of approximately 2.355, which is expected for a Gaussian. Again, this can be explained by the outliers towards both sides of the ToT spectrum. The standard deviation is heavily influenced by these and especially the tail towards larger ToT values introduces outliers very far away from the mean. As there are now outliers to both sides of the core of the distribution, the ratio is even smaller than in the low bias voltage case.

Finally, Figure 9.16 displays a comparison of the median distributions at -15 V (blue) and -130 V (red). Here, the observation made in Figure 9.12 can be confirmed for the full sensor. The median distribution of the higher bias voltage is shifted towards higher median values. Nevertheless, the overall shape of distributions is similar. In foresight of the calibration, this is very valuable input. In consequence, to enable a precise calibration, for every evaluated bias voltage, a corresponding ^{55}Fe calibration data set is necessary.

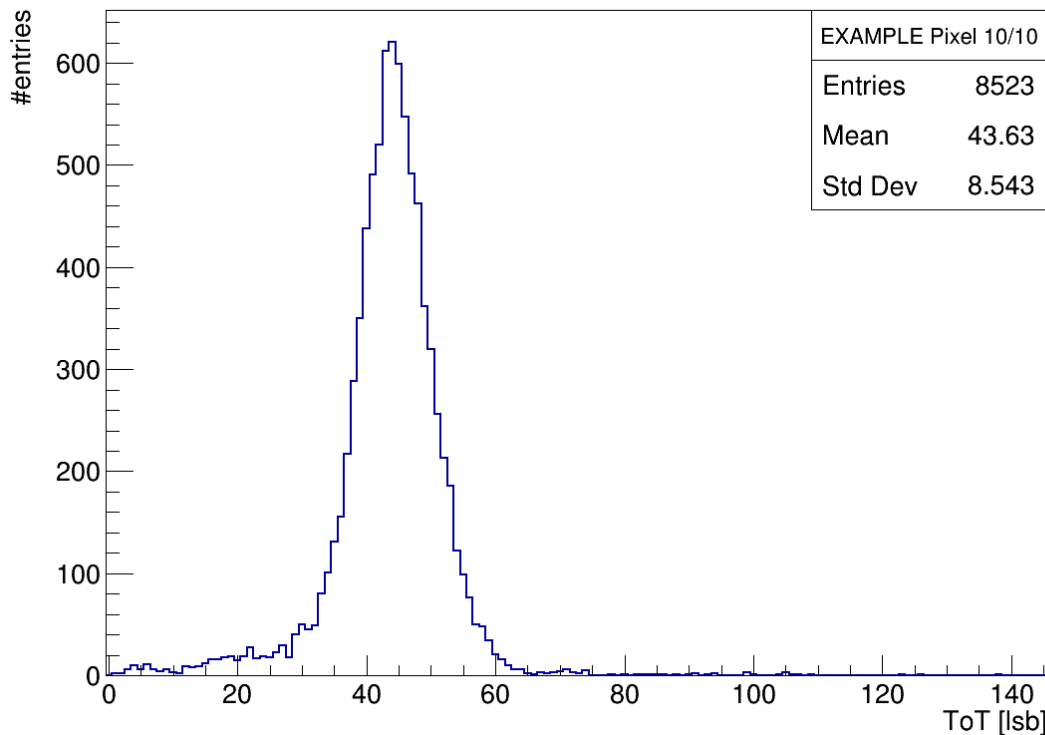


Figure 9.13: ToT distribution of a single pixel (pixel address 10/10) for ^{55}Fe at a bias voltage of -100 V.

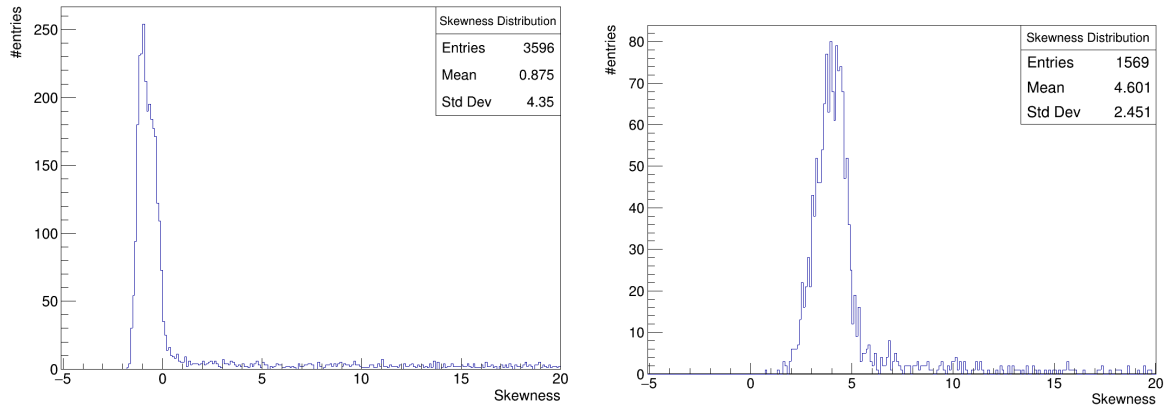


Figure 9.14: Skewness of the ToT distribution on a per pixel basis for ^{55}Fe at a bias voltage of -15 V (left) and -130 V (right).

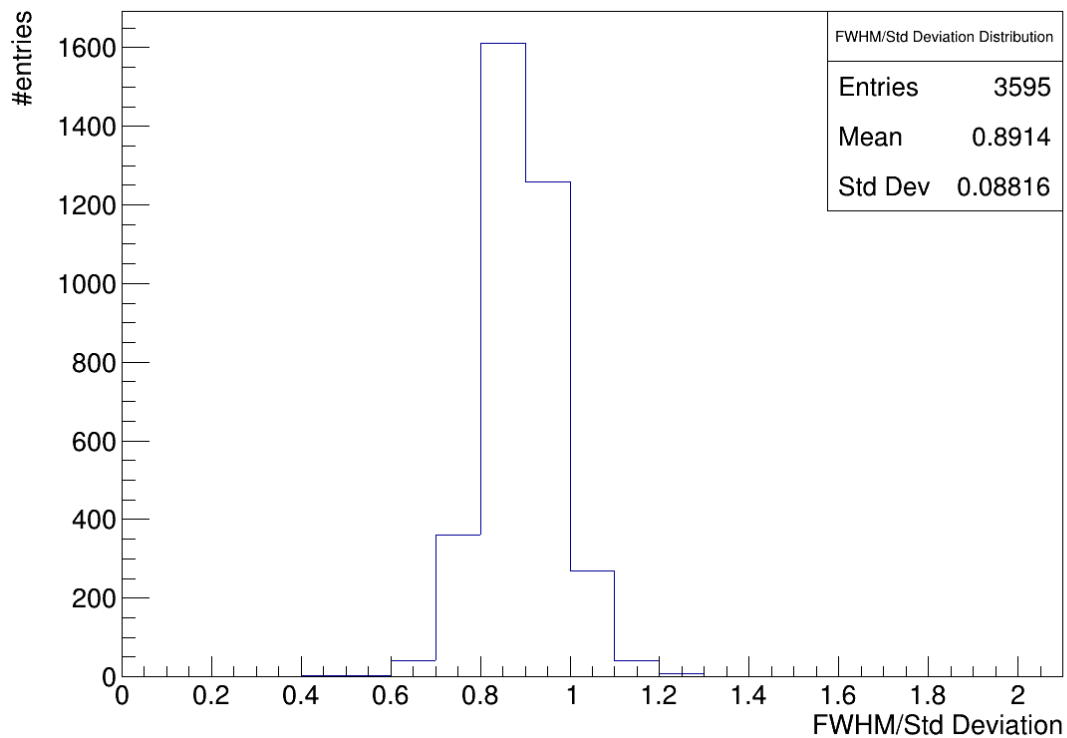


Figure 9.15: Ratio of the FWHM to the standard deviation of the ToT distribution on a per pixel basis for ^{55}Fe at a bias voltage of -130 V .

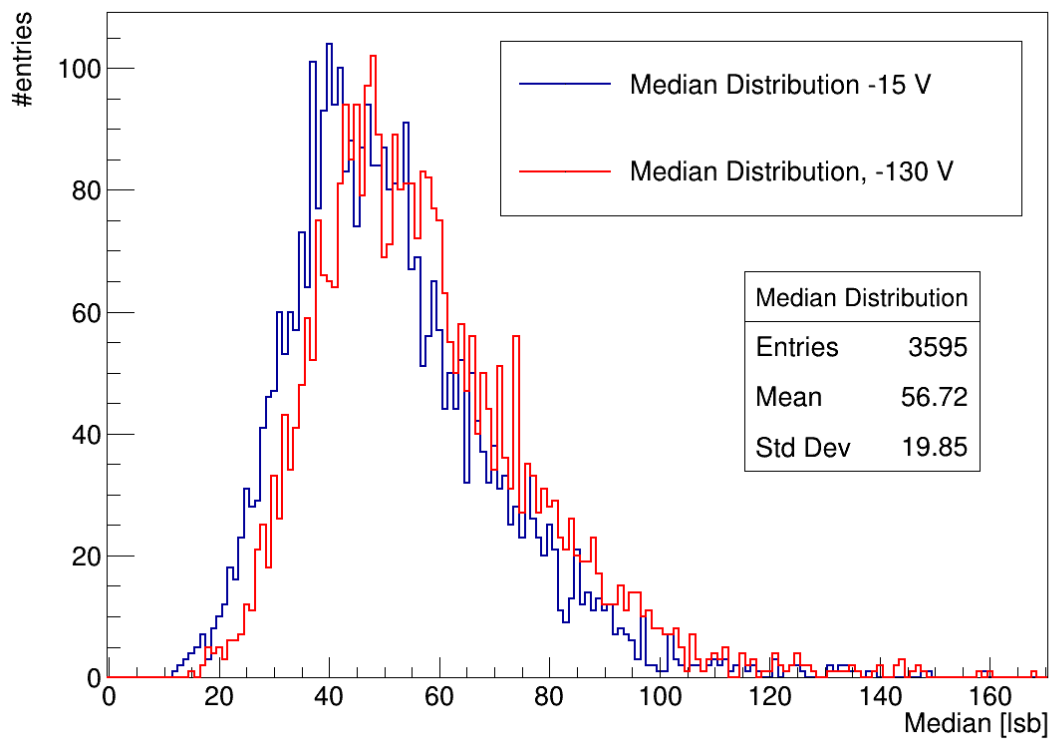


Figure 9.16: Median of the ToT distribution on a per pixel basis for ^{55}Fe at a bias voltage of -15 V (blue) and -130 V (red).

10 ToT Calibration

10.1 Introduction

The ToTAnalyzer, which is discussed in section 9, has an option to write the created distributions to a file. This file contains the information about the signal response (contained in the mean, mode or median) of every pixel to the monochromatic source. The basis of the ToTCalibration module is this file written by the ToTAnalyzer and the ToT information of every pixel, obtained from the event loader. The general approach for the calibration, using the monochromatic ^{55}Fe source, is explained in subsection 9.2. As tails are observed in single pixel ToT distributions, the median is chosen for the ^{55}Fe calibration in this thesis. To avoid signals shared between two pixels, a cluster size cut is used to only allow a cluster size of 1. A detailed discussion of this choices is given in the discussion of uncertainties of the calibration at the end of this subsection. In the following, two functions for the calibration are implemented and tested.

The first approach, which changes the ToT by *shifting* it to higher values uses the following function:

$$ToT_{\text{new}} = ToT_{\text{signal}} + (ToT_{\text{cal}}^{\text{max}} - ToT_{\text{cal}}^{\text{Pixel}}) \quad (10.1)$$

Here, $ToT_{\text{cal}}^{\text{max}}$ is the largest median within the calibration file, while $ToT_{\text{cal}}^{\text{Pixel}}$ is the median of ^{55}Fe for the pixel which is calibrated. ToT_{signal} is the ToT value of a hit. Note, that this method does retain the original signal shape and only *shifts* the ToT distribution of every pixel. After the calibration, the value of $ToT_{\text{cal}}^{\text{max}}$ equals 1615 electrons (see subsection 9.2) for all pixels on the sensor. However, this approach does not take into account the observed relationship between median and FWHM (see Figure 9.11). Hence, this method does not achieve the goal of equalizing the pixel responses for the sensor and is therefore discarded.

The second approach uses a factor to *scale* the ToT. Here, the calibration information is incorporated in the following way:

$$ToT_{\text{new}} = ToT_{\text{signal}} \cdot \left(\frac{ToT_{\text{cal}}^{\text{median}}}{ToT_{\text{cal}}^{\text{Pixel}}} \right) \quad (10.2)$$

Where $ToT_{\text{cal}}^{\text{median}}$ is the median value of the median distribution of all pixels in the calibration file. Here, the ToT of every pixel is scaled so that after calibration $ToT_{\text{cal}}^{\text{median}}$ equals 1615 electrons. Moreover, this approach also changes the signal width and hence also changes the FWHM of every pixel. Therefore, this linear scaling approach takes the amplifier behavior which is observed in Figure 9.11 better into account than the shift method. In subsection 10.2 the scaling calibration method will be cross-checked, to ensure its functionality.

However, there are several sources for uncertainty in the calibration procedure which have to be evaluated first. Generally, the emitted photon from ^{55}Fe interacts via the photoelectric effect. Here, the energy deposition is very localized, which makes the ^{55}Fe a perfect source for the calibration. Moreover, the penetration depth of a 6 keV photon in silicon is 30 μm [46]. Hence, especially in the low bias voltage case, where the depletion depth is only about 24 μm , the photon can deposit its energy in the undepleted substrate. If diffusion indeed plays a significant role in the signal creation, these charges could add to the signal of another photon and

therefore distort the signal towards larger depositions. However, the ^{55}Fe source has a rate of about 50 Hertz per pixel while the recombination time of a free charge carrier in the substrate is in the order of 100 μs [9]. Therefore, diffusion is negligible for the ^{55}Fe signal. Furthermore, the energy of the photon could be deposited on the border of a pixel, leading to a reduced charge collection in the individual pixels. However, the cluster size for ^{55}Fe is very close to 1 (only about 0.1% of hits with cluster size 2). Nevertheless, the small amount of cluster size 2 events are filtered out by the cluster size cut which is set to 1. Still, events where a portion of the energy of the photon is either deposited in the insensitive top layer or in a neighboring pixel without crossing the threshold are possible. These can not be filtered out and might introduce a shoulder towards small ToT values. Additionally, the ^{55}Fe source emits also photons with an energy of 6.4 keV. The probability for this process is about one order of magnitude smaller than the processes which emit the photons around 5.895 keV. Nevertheless, these entries skew the spectrum towards larger energy depositions. As outliers towards both sides of the spectrum are present, the median is the most stable measure to characterize the energy deposition of the photons around 5.895 keV. Another uncertainty arises from the dispersion of thresholds in the pixel. As every pixel has its own comparator, the threshold can vary slightly, which directly influences the ToT. In principle, it is possible to fix this issue for the Run2021v2 sensor on a hardware level by so-called tuning. However, it is not feasible within this study to perform a tuning of the sensors.

Finally, the probably largest uncertainty arises from the assumption of linearity between deposited energy and ToT. For a minimum ionizing electron an energy loss rate of 0.35 keV/ μm can be determined from the Berger-Seltzer formula in Figure 2.3. Therefore, for a depletion depth of 70 μm the average energy loss of a minimum ionizing electron is 24.5 keV, yielding approximately 6700 electron-hole pairs. This is a factor 4 more electrons than the ^{55}Fe source produces. One possibility to investigate the linearity would be a study using the injection circuit of the sensor. Therefore, the injection signal is characterized in subsection 10.2.2 and the linearity is investigated in section 11.

10.2 Quality Control of Calibration

For the quality control of the calibration a ^{55}Fe data set is used to create a calibration file. Then a second ^{55}Fe measurement is taken and evaluated with these calibration values. Both measurements are taken at the same bias voltage of -15 V . Subsequently, a short complementary study using the injection circuit is presented. Both of these measurements are performed with the unthinned sensor.

10.2.1 ^{55}Fe Calibrated

First, the calibrated and uncalibrated ToT distributions are compared. This is shown in Figure 10.1, where the calibrated ToT is shown in red and the uncalibrated in blue. To evaluate the improvement, the FWHM is compared for both distributions. Here, the uncalibrated distribution has a FWHM of 37 lsb, while the FWHM of the calibrated distribution is 16 lsb. As a comparison, the FWHM of the example pixel 10/10 is 13 lsb. The median of the median distribution is 50 lsb for the data set and hence all single pixel ToT distributions got scaled to this value. Moreover, the tail towards higher ToT values vanished, showing that at this low

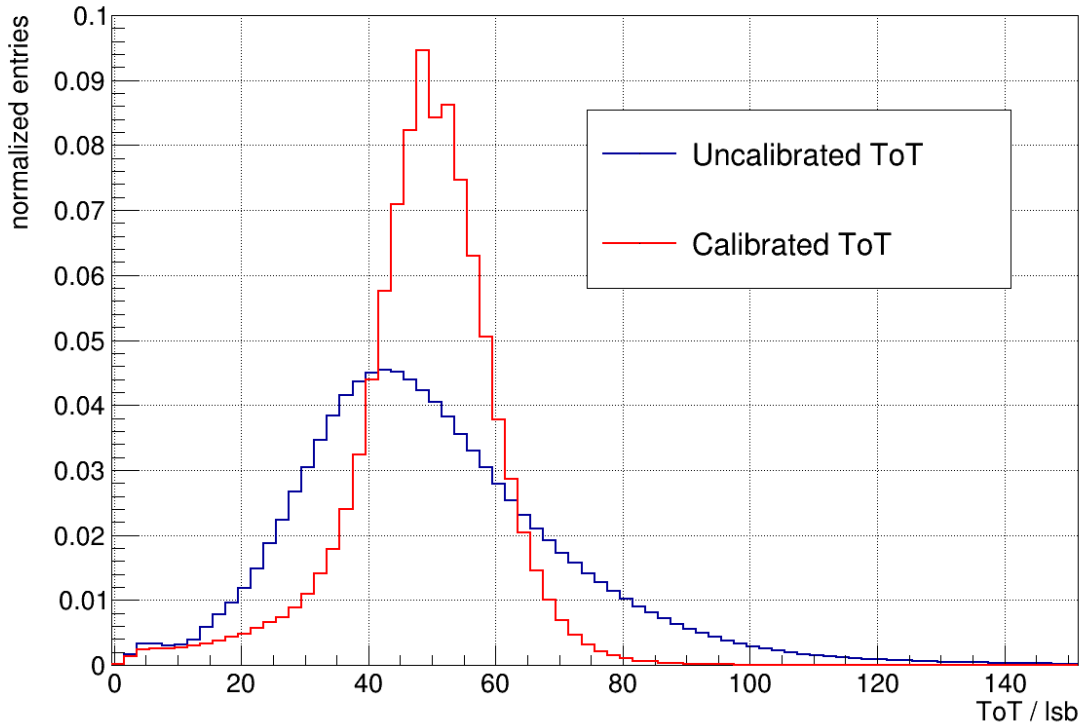


Figure 10.1: Normalized ToT distribution for ^{55}Fe before (blue) and after correction (red) for the full sensor. The applied bias voltage is -15 V .

bias value the tail towards larger ToT values is induced by pixel-to-pixel variations. The tail towards lower ToT values is still present although not as pronounced as in the uncalibrated spectrum. This is expected, as the calibration does not discard the charge sharing entries. However, an improvement is also visible on the left side of the distribution. In the uncalibrated case, the difference in pixel response broadens and distorts the distribution, while after calibration the response is well aligned, as the distribution has a comparable FWHM to the single pixel one. Furthermore, in the single pixel ToT in Figure 8.9, a small excess of entries is observed at the point where the photons from the K_β decay would be expected. In the calibrated spectrum, again a small excess of entries is visible at about 10% higher ToT.

Next, the correlation between FWHM and median is investigated. Figure 10.2 shows the correlation plot before (top) and after the calibration (bottom). The median is shown on the x-axis and the FWHM on the y-axis. With regard to the median, the calibration achieves a sizable compression. Almost all entries for the median are within (50 ± 2) lsb. This is a significant improvement in comparison to the uncalibrated data set. For the FWHM, a majority of the pixels has a FWHM of (18 ± 5) lsb. However, the scale for the FWHM is still large after the calibration and outliers are still present. This is expected, as the correlation before the calibration is not perfectly linear, leading to an over- or under correction of the FWHM in a linear scaling calibration.

In conclusion, the calibrated results for the ^{55}Fe source look promising. The overarching goal of equalizing the pixel response to a monochromatic source is achieved. The FWHM of the ToT distribution of the full sensor in Figure 10.1 is more than halved after the calibration and the response of the pixels is more uniformly. More-

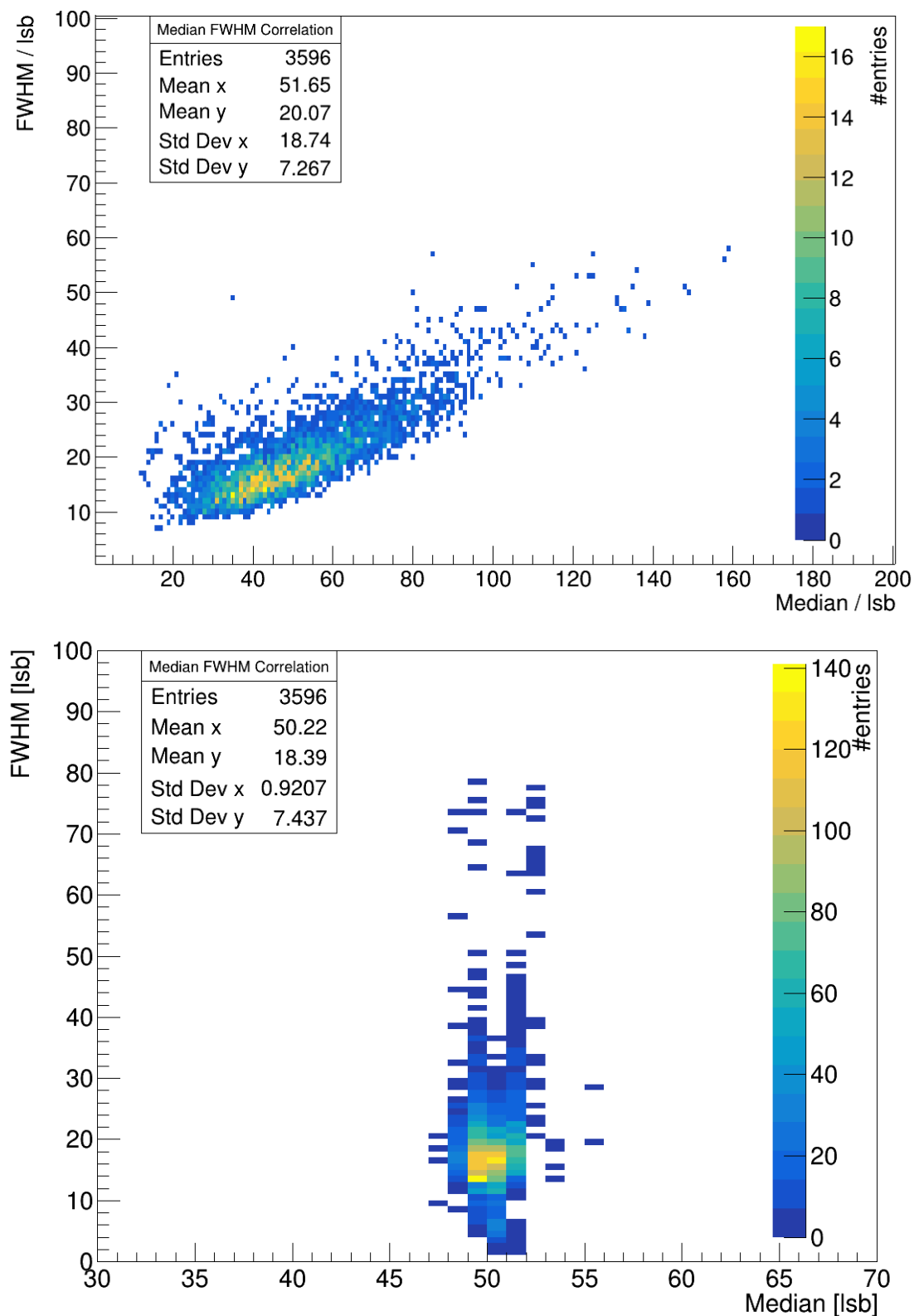


Figure 10.2: Correlation between the FWHM and the median of the ToT distribution for ^{55}Fe before (top) and after (bottom) calibration on a per pixel basis. The applied bias voltage is -15 V .

over, this is also visible in the median distribution on a per pixel basis in Figure 10.2, where the spread of the median is compressed. Moreover, the FWHM distribution is squeezed together by the calibration as well. However, outliers are still present over a large range. Hence, some of the pixels still have a broad ToT distribution even though their median is well aligned. Nevertheless, a significant improvement is visible in the calibrated ToT distribution in Figure 10.1.

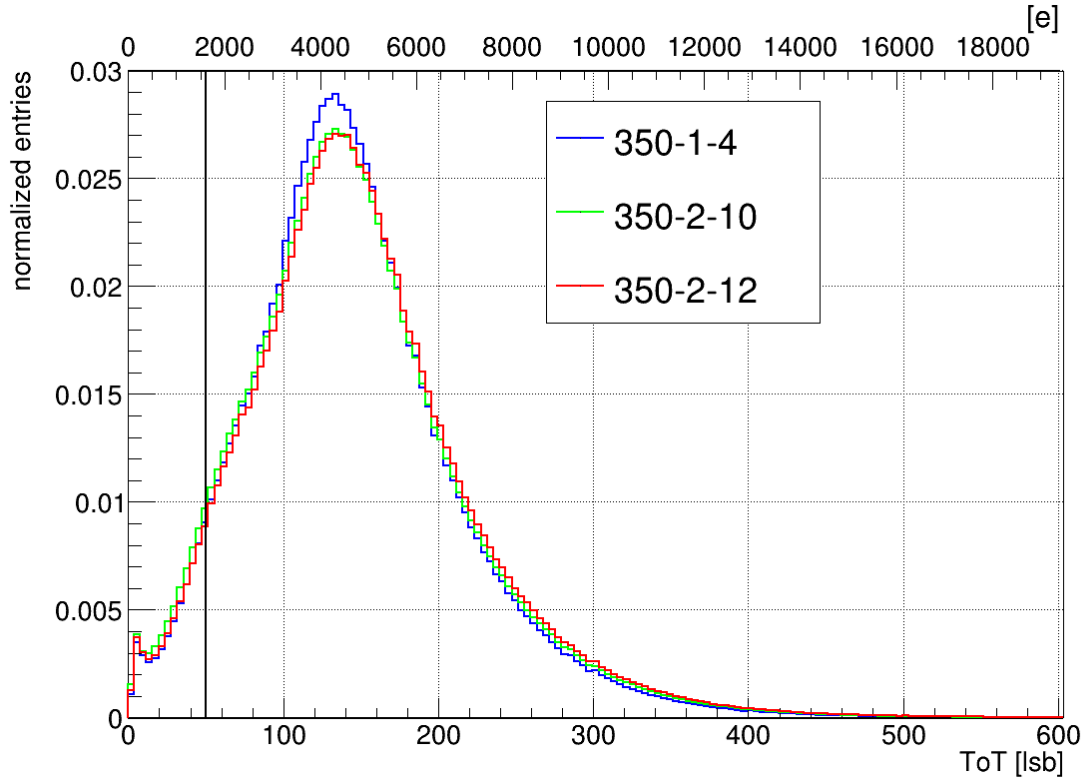


Figure 10.3: Calibrated ToT for the ^{90}Sr source for the three unthinned sensors with an applied bias voltage of -30 V . The vertical black line indicates the median of the ^{55}Fe signal after calibration.

Chip ID	MPV [lsb]	FWHM [lsb]
350-1-4	136	116
350-2-10	136	124
350-2-12	136	128

Table 5: Most probable value and FWHM for the three unthinned sensors after calibration at a bias voltage of -30 V . The signal source is ^{90}Sr .

Finally, the calibration method is used to investigate the ^{90}Sr spectrum for the three unthinned sensors, where the difference in response necessitated the calibration. The uncalibrated ToT distributions in Figure 8.8 show different most probable values and different widths, even though the applied bias voltage of -30 V , settings and signal source are the same. Figure 10.3 shows the resulting ToT distributions

after calibration for the same data set. For the comparison of different sensors, the calibration is slightly modified. Instead of using the median of the median of the calibration data set, a common, arbitrary number is used. The calibration formula used is:

$$ToT_{\text{new}} = ToT_{\text{signal}} \cdot \left(\frac{50}{ToT_{\text{cal}}^{\text{Pixel}}} \right) \quad (10.3)$$

Hence, after this calibration all sensors share a common axis where the median of the ^{55}Fe signal is at 50 lsb. This number is chosen, as it is close to the median of the median distribution for all investigated sensors. An identification of the ^{55}Fe source with 1615 electrons (see subsection 5.6) allows a conversion of lsb to collected electrons. This is indicated by the vertical line in Figure 10.3, representing the sensor response to ^{55}Fe after the calibration. It should be noted, that this axis assumes a perfect linear relationship between deposited energy and ToT. This is not the case at large charge depositions, as the amplifier saturates. Hence, the scale in electrons underestimates the collected electrons at a certain point. The ToT spectra of the three sensors are now very similar. Table 5 summarizes the most probable value and FWHM of the three sensors. All of them have their most probable value at the same point (about 4300 electrons). However, the FWHM still exhibits a slight variation. This is in agreement with the observation in Figure 10.2, where the FWHM is not calibrated as well as the median. Especially the sensor 350-1-4 has a smaller FWHM than the other two. A possible explanation could be, that this sensor has overall less noise. In conclusion, slight variations in the sharpness of the peak and the extend of the tail are still possible after the calibration. Nevertheless, the alignment of the most probable value is very exact after the calibration and allows for a quantification of diffusion in the next section.

10.2.2 Injection

In a complementary study, the injection circuit is characterized and used to test the calibration method as well. The injection circuit is an artificial signal source, where the generated charge depends on the injection capacity of the pixel and the injection voltage. The charge is released directly into the amplifier. For further information on the injection circuit see subsection 4.5. Therefore, in the following, a subset of 100 pixels arranged in a checkerboard pattern of the unthinned sensor is used. Due to power constraints of the injection, it is not possible to inject more pixels simultaneously. For the study an injection voltage of 300 mV is chosen, to imitate the signal of the ^{55}Fe source. These pulses are injected in each of these pixels with a frequency of 1000 Hz. The applied bias voltage is -130 V.

First, the uncalibrated data is investigated. Figure 10.4 shows the ToT distribution of a single pixel with a Gaussian fitted to the distribution. Here, it is evident, that the injection signal is of perfect Gaussian shape. The variations in the ToT signal which lead to the Gaussian shape, are a small variation of injection voltage for each injection and electronic noise of the pixel. The FWHM of the distribution is 11 lsb. Hence, the single pixel response of pixel 10/10 yields a sharper response for the injection than for the ^{55}Fe source, where the FWHM is 13 lsb. The larger FWHM of the ^{55}Fe source is probably caused by the higher energetic photon which is emitted in the K_{β} decay. The observed spectrum is a superposition of both decays and hence has an increased FWHM.

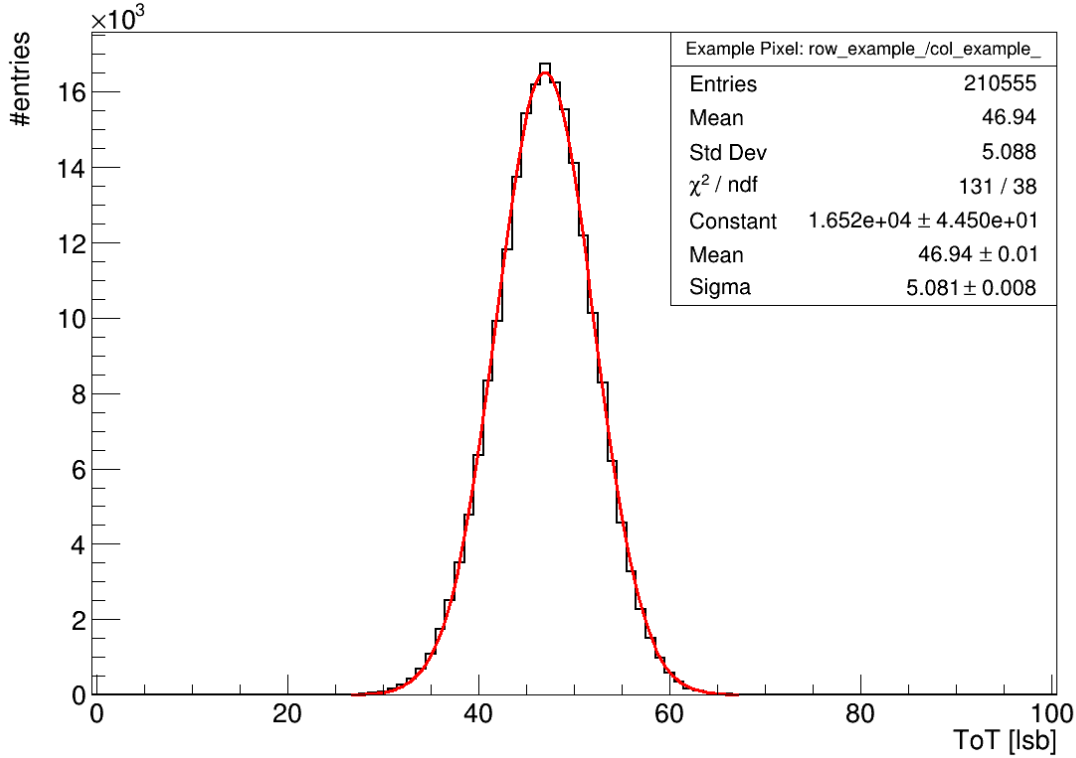


Figure 10.4: Injection signal in pixel 10/10 for an injection voltage of 0.3 V, with a Gaussian fitted to the distribution.

Figure 10.5 shows the ratio of FWHM to standard deviation (top), the skewness (middle) and excess kurtosis (bottom) for the 100 tested pixels. The ratio of FWHM to standard deviation is centered around the Gaussian value of 2.355 with only a few outliers to lower values. Moreover, the skewness is very close to 0 for almost all pixels, indicating symmetrical ToT distributions for each pixel. Furthermore, the excess kurtosis is centered around 0, indicating Gaussian tails. In conclusion all three measures show that the injection signal of the individual pixels is of Gaussian shape.

Finally, Figure 10.6 shows the uncalibrated and calibrated ToT distribution of the 100 injected pixels. Both distributions have exactly the same amount of entries and are therefore not normalized. In blue the uncalibrated spectrum is shown. Here, the spectrum has a peculiar shape, as the distribution is very broad with multiple peaks visible and an almost linear decline towards large ToT values. These multiple peaks are not localized as can be seen from the median map of the single pixel ToT distributions in Figure B.3 in Appendix B. Naively, there are two possible reasons for this strange shape of the distribution: First, a variation in injection capacitance from pixel-to-pixel could lead to a different amount of charge injected in each of the pixels. Second, the amplifier behavior which was already shown to have large variations in the previous section. One should also keep in mind that the amount of injected pixels is only about 100, which corresponds to less than 3% of the sensor. However, the calibrated spectrum (red) is again very close to a Gaussian shape. The calibrated distribution has a FWHM of 16 lsb, while the uncalibrated distribution has a FWHM of 42 lsb. As the calibration improves the distribution significantly, it is concluded that the spread in the uncalibrated

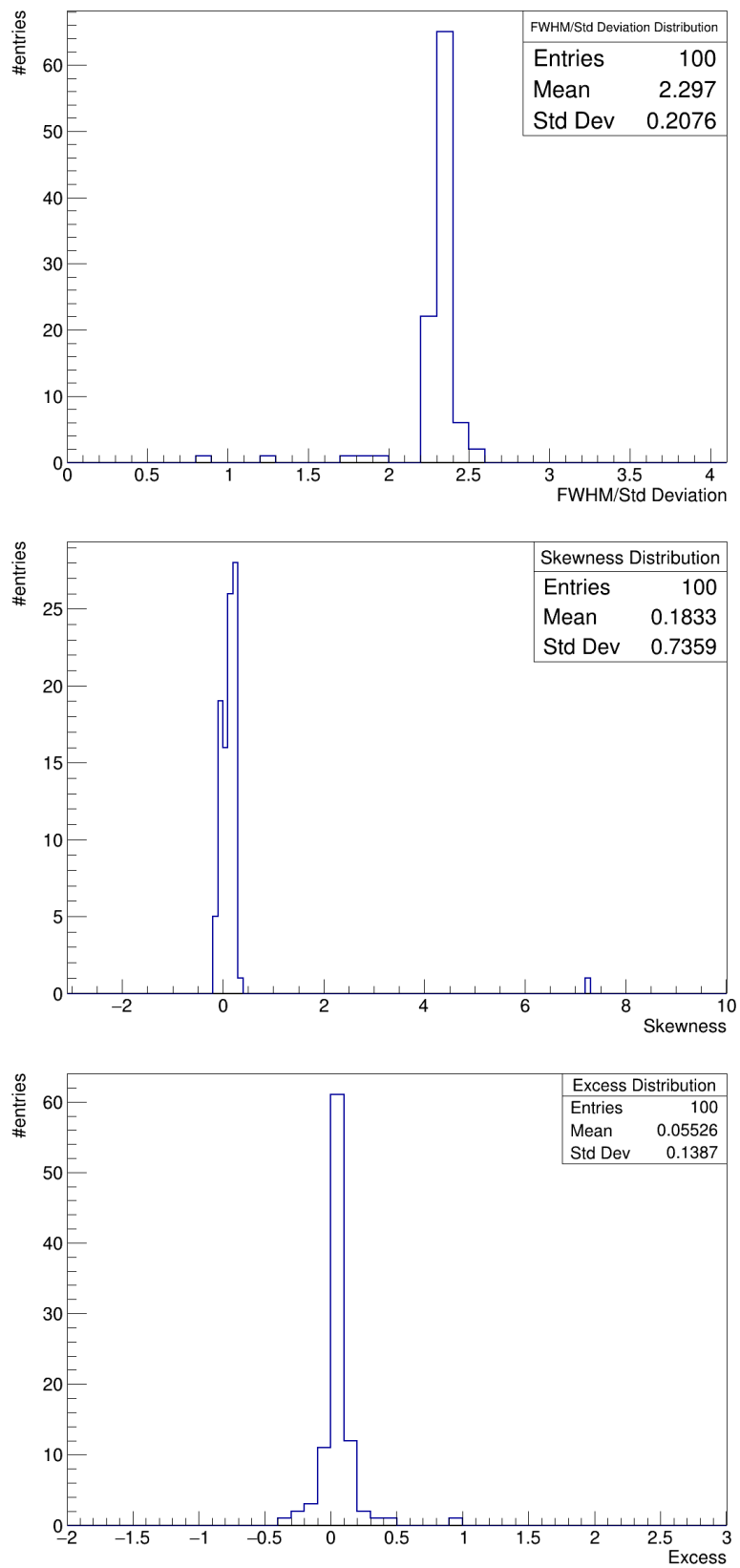


Figure 10.5: Ratio of FWHM to standard deviation (top), skewness (middle) and excess kurtosis (bottom) for the injection signal of 100 pixels.

distribution is dominated by the amplifier behavior, which is corrected by the ^{55}Fe signal. If a strong variation in injection capacitance would be present, the result of the calibration would deteriorate.

Nevertheless, a variation in pixel capacitance seems to be present. This is concluded, as the single pixel ToT of the injection has a smaller FWHM compared to the ^{55}Fe signal. After the calibration, the injection signal in 100 pixels and the spectrum of the ^{55}Fe signal in the entire sensor have the same FWHM of 16 lsb. Hence, an additional uncertainty is introduced in the injection measurement, which is the variation of injection capacitance.

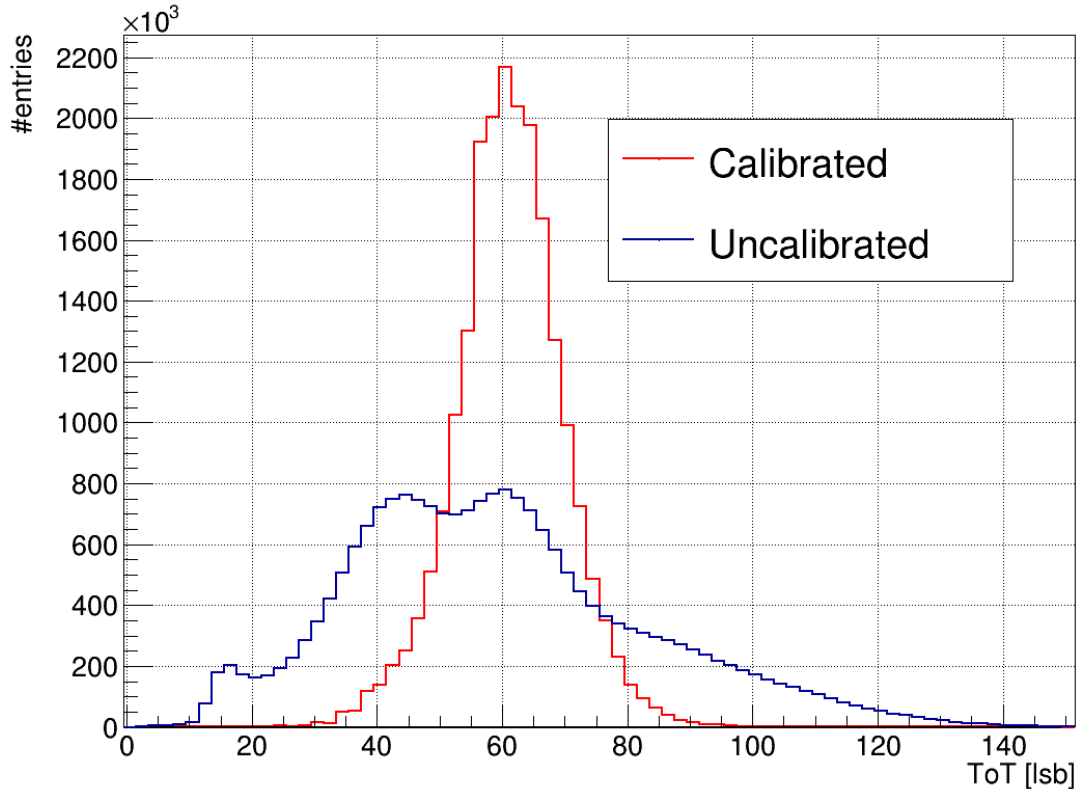


Figure 10.6: ToT distribution for the injection signal of 100 pixels. The blue distribution is the uncalibrated data set, while the red distribution is calibrated with the ^{55}Fe source.

In conclusion, the calibration using the ^{55}Fe source allows to remove a majority of the sensor-to-sensor variations. For both the ^{55}Fe and the injection as signal source a sizable improvement in comparison to the original uncalibrated data set is achieved. In both cases the resulting spectra are closer to a Gaussian shape and the FWHM is significantly reduced. In addition, the three different unthinned sensors have a very similar response to the ^{90}Sr signal after calibration. Nevertheless, a small variation in FWHM is still present after calibration. This is explainable by the outliers in the FWHM distribution which are not calibrated perfectly. Overall, the ^{55}Fe calibration is suitable to overcome the sensor-to-sensor variations and facilitate a more detailed study of diffusion.

11 Calibrated Diffusion Studies

In the previous two sections a framework to perform a sensor calibration is introduced. This framework is now used to overcome the sensor-to-sensor variation observed in section 8. In the following, a high statistic ^{55}Fe data set is taken for every sensor and every used setting. These data sets are evaluated with the ToT-Analyzer module and the median of the single pixel ToT distribution is written to a file for every pixel. This file is then used in the ToTCalibration module to scale the ToT of every single pixel with an individual factor (see section 10). Here, instead of the median of the median distribution, again a common factor is used to achieve comparable results for every sensor. Hence, after the calibration every sensor has the same response to the ^{55}Fe source. The common factor is chosen arbitrarily to be 50 lsb, so that this value can be identified for every sensor with the 1615 electrons generated by ^{55}Fe .

11.1 Test Beam

First, the results from the DESY test beam are calibrated. Figure 11.1 shows the normalized ToT spectra for both the 50 (blue) and 100 (red) μm sensor. Both the sensors have a bias voltage of -15 V , and should therefore have the same depletion depth. However, the 100 μm sensor has more undepleted substrate and therefore more diffusion volume. This is reflected in the ToT, where the 100 μm sensor is shifted towards higher ToT values. Again, a black vertical line is used to indicate

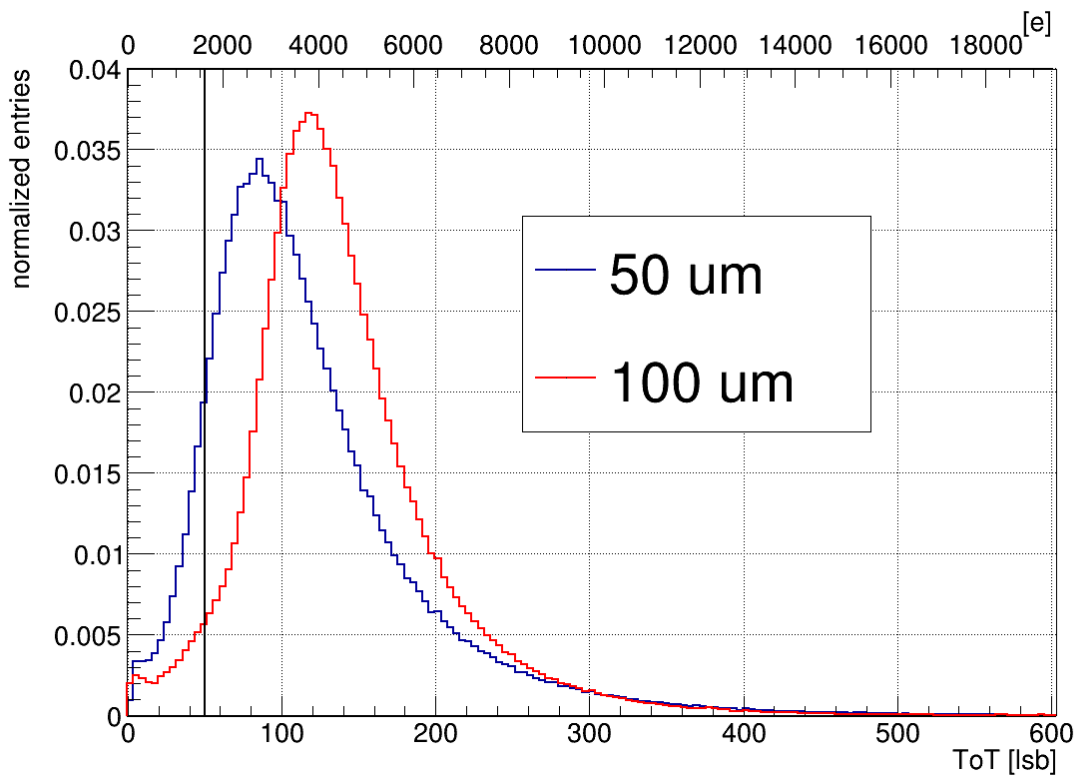


Figure 11.1: Calibrated ToT for an applied bias voltage of -15 V for the 50 (blue) and 100 μm (red) sensor. The signal source are perpendicularly impinging 4 GeV electrons.

the median response for ^{55}Fe of the calibrated sensors. In comparison with Figure 8.5 the ToT distributions after the calibration only differ slightly to the uncalibrated ones. However, this is expected as the response to ^{55}Fe is rather similar in Figure 8.9 for these two sensors.

The linear calibration to the ^{55}Fe source allows a gauging of the ToT to the collected electrons. Here, the most probable value of the 50 μm sensor is approximately 2600 electrons, while the 100 μm sensor is at about 3600 electrons. Therefore, the 100 μm sensor collects on average about 38 % more charge, due to diffusion in the approximately 55 μm of the undepleted substrate. This number might underestimate the actual collected electrons, if the amplifier is non-linear at these energy depositions.

The beam in the DESY test beam facility consists of electrons with an energy of 4 GeV. According to the Berger-Seltzer formula (see Figure 2.3), electrons at this energy lose approximately 5.2 keV in 10 μm of silicon. Therefore, one can calculate the electron-hole pairs created in the depleted volume. For the depletion depth of $(24.05 \pm 0.65) \mu\text{m}$ at a bias voltage of -15 V (see section 8), one would expect a deposited energy of $(12.5 \pm 0.3) \text{ keV}$ for electrons. The necessary average energy to create an electron-hole pair in silicon at room temperature is $(3.65 \pm 0.01) \text{ eV}$ (see subsection 9.2). Hence, the average amount of collected charge from the depleted volume can be calculated to be $(3426 \pm 93) \text{ e}^-$ for an electron traversing the sensor perpendicularly. This value can be compared to the mean of the distribution. For the determination of the mean, the part of the distribution which has below 0.4% entries is cut off, to avoid noise and crosstalk entries on the left side of the distribution and the long tail towards large entries to dominate the determination of the mean.

This yields a mean of 106 lsb for the 50 μm sensor, corresponding to approximately 3300 e^- which is in agreement with the calculated value for the depletion depth of $(24.05 \pm 0.65) \mu\text{m}$. The 100 μm sensor exhibits a mean of 132 lsb, corresponding to about 4000 e^- . This is 25% more charge collection than for the 50 μm sensor and significantly more than the amount of electrons expected from drift. Nevertheless, it is not clear at this point if a incipient saturation of the amplifier leads to an under estimation of the influence of diffusion.

The saturation effect can be investigated in the injection circuit. To do so, the injection voltage is scanned and plotted against the mean ToT for the pixel with address 10/10 of the unthinned sensor. In the previous section the pulse shape of the injection is observed to be Gaussian, allowing to use mean and standard deviation as a parametrization of the ToT distribution. As it is possible to inject about 5 times the charge of ^{55}Fe , it is well suited to investigate the amplifier behavior. Moreover, the injection can be gauged with the median of the ^{55}Fe source to calculate the injection capacitance and determine the amount of injected electrons. For the example pixel, ^{55}Fe can be identified with an injection voltage of $(0.290 \pm 0.005) \text{ V}$. Thus, following Equation 4.2, the injection capacitance is calculated to be $(0.892 \pm 0.017) \text{ fF}$. With the applied threshold, the range of injection voltage is 0.25 V to 1.5 V. Hence, using the calculated capacitance, the maximum injection charge is determined to be $(8352 \pm 159) \text{ e}^-$.

The measurement is shown in Figure 11.2, where the injection voltage and the injected charge are displayed on the y-axis, while the ToT in units of lsb is shown on the x-axis. The data points correspond to the mean of the ToT distribution for each evaluated injection voltage, while the uncertainties are the standard deviation

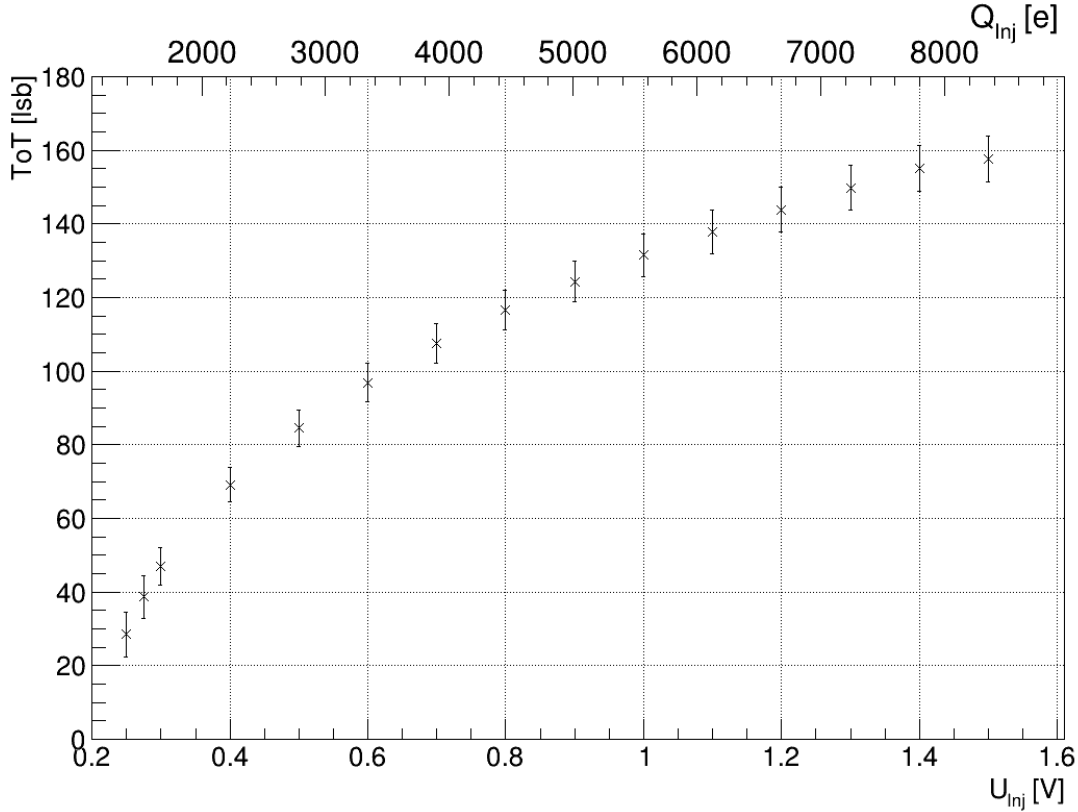


Figure 11.2: Scan of the injection voltage to investigate the amplifier behavior for pixel 10/10, where every data point corresponds to the mean of the ToT distribution. The mean ToT follows a logarithmic function, exhibiting a strong saturation for large charge depositions.

of the distribution. To avoid significant statistical uncertainties, the pulse is injected at least 100 000 times for each point. The data exhibits an approximately logarithmic behavior, indicating a starting amplifier saturation at about 2200 e^- . A strong saturation is reached for injection charges above 7000 e^- . Therefore, this measurement is supporting the observation in Figure 11.1, where a saturation is suspected. Hence, the linear calibration of the ToT is underestimating the additional charge collection via diffusion. It should be noted, that this is only the amplifier behavior of a single pixel. As large variations are observed before for the amplifier, it is possible that also the points where the saturation is reached, differ. Hence, a more detailed study of the amplifier behavior at large charge depositions for the entire sensor is necessary, to further improve the calibration.

Nevertheless, as the injection scan reveals a deviation from the linearity for charge collections of about 2200 e^- , it can be used to give an estimate of the actual number of collected electrons. As all sensors are calibrated to the same axis, especially the low and medium energy deposition regime of Figure 11.2 yields a valid estimate of the collected electrons, which takes the amplifier saturation into account. It should be noted, that the higher bias voltage in the injection measurement leads to an underestimation of the total collected charge for the ^{90}Sr measurement at a bias voltage of -15 V for both sensors. Again, the mean of both distributions can be used to approximate the number of collected electrons. Here, the mean ToT for the $50\ \mu\text{m}$ sensor corresponds to approximately 3700 e^- , while the mean of the $100\ \mu\text{m}$

sensor corresponds to about $5600 e^-$. While the amount of collected charge for the $50 \mu\text{m}$ is barely within the uncertainty of the expected amount for positrons, it is exceeding the uncertainty for electrons. The $3700 e^-$ would correspond to a charge collection in approximately $27 \mu\text{m}$ of silicon, in tension to the $(24.05 \pm 0.65) \mu\text{m}$ of depletion depth. This difference can be explained by the approximately $5 \mu\text{m}$ of undepleted substrate, which are still present in the $50 \mu\text{m}$, where diffusive charge can be collected. On the other hand, the calculation of the depletion depth might also underestimate the actual depletion depth. The $100 \mu\text{m}$ sensor collects an additional $1900 e^-$, yielding about 50% more charge collection, arising from diffusion.

Table 6 summarizes the results obtained with the 4 GeV electron beam. Here, "e⁻ from drift" denotes the calculated mean charge collection from drift for the depletion depth, "e⁻ (⁵⁵Fe Calibration)" is the number of electrons obtained for the mean of the ToT distribution from the ⁵⁵Fe calibration and "e⁻ (Injection Gauging)" is the estimation using the injection scan.

Thickness	e ⁻ from drift	e ⁻ (⁵⁵ Fe Cal.)	e ⁻ (Injection Gauging)
50 μm	(3295 ± 89)	3300	3700
100 μm	(3295 ± 89)	4000	5600

Table 6: Summary of the collected e⁻ for the 4 GeV electron source for a bias voltage of -15 V .

11.2 ⁹⁰Sr

Next, all three sensors are compared for the ⁹⁰Sr source in Figure 11.3, where all sensors are at -15 V bias voltage. For every ⁹⁰Sr measurement each pixel has about 10 000 entries to keep statistical uncertainties as small as possible. Again, the ToT distributions are each normalized with respect to their entries and the black vertical line indicates the calibration value which represents the sensor response to the ⁵⁵Fe source. Here, the $100 \mu\text{m}$ and the unthinned sensor show clearly a tendency to larger ToT values in their distribution, as the most probable value is shifted in comparison to the $50 \mu\text{m}$ sensor. The most probable values are determined to be 85 lsb ($50 \mu\text{m}$), 114 lsb ($100 \mu\text{m}$) and 117 lsb (unthinned). This corresponds to a charge collection of about $2750 e^-$, $3650 e^-$ and $3750 e^-$, respectively. Moreover, the $100 \mu\text{m}$ and the unthinned sensor are rather similar in their behavior. However, the most probable value of the unthinned sensor is at a higher ToT value. In Figure 10.3 it is shown that the calibration aligns the most probable value very well. Hence, this is an indicator for a slightly larger contribution of diffusion in comparison to the $100 \mu\text{m}$. This would be supported by the observation of the cluster size in Figure 8.2 where the unthinned sensor had a slightly larger cluster size than the $100 \mu\text{m}$ sensor as well. The Gaussian spread of a diffusing charged particle is calculated to be $(87 \pm 7) \mu\text{m}$ for a ToT of 1000 ns which is the most probable value for the ToT of the unthinned sensor. This indicates, that charge can diffuse into several neighboring pixels, as the pixel width in row direction is only $25 \mu\text{m}$. The $100 \mu\text{m}$ sensor has approximately $55 \mu\text{m}$ of undepleted substrate at this bias voltage. Therefore, it is possible that the

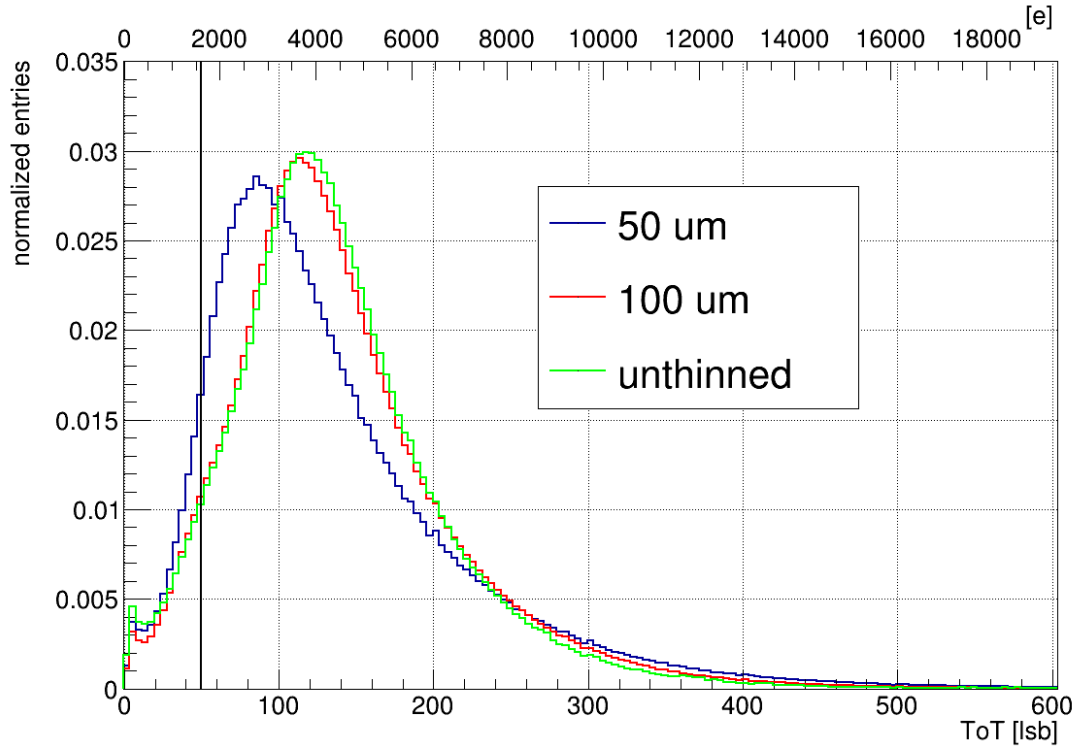


Figure 11.3: Calibrated ToT for the ^{90}Sr source for the 50 μm (blue), 100 μm (red) and unthinned (green) sensor with an applied bias voltage of -15 V .

unthinned sensor collects a bit more charge from the additional undepleted substrate in comparison.

In comparison to the uncalibrated ToT spectrum in Figure 8.6, both the 100 μm and the unthinned sensor seem to have more entries at lower ToT. These entries are caused by the calibration, where a linearity between ToT and collected charge is assumed. While this linearity is a good approximation at the energy of ^{55}Fe , it fails for larger charge collections as shown in the injection scan above. If the ToT underestimates the amount of collected charge for the ^{90}Sr source, the linear scaling can lead to an over correction towards low ToT entries. As an example, this is especially the case for pixels which have a large median above 100 lsb for the ^{55}Fe source and are therefore scaled with a small factor smaller than $\frac{1}{2}$ in the calibration. Hence, the emerging shoulder towards lower ToTs in these sensors is a sign of the limitations of the linear calibration.

Again, it is possible to use Figure 11.2 to get a second estimate of the amount of collected electrons. As it is anyway not possible to precisely determine the mean energy loss of the energy spectrum of the ^{90}Sr source, the most probable value is used to quantify the charge collection. The majority of electrons, which are detectable from the ^{90}Sr (see Figure 5.4) are in the minimum ionizing region of the Berger-Seltzer graph (see Figure 2.3). Hence, a mean energy loss of about 3.5 MeV is assumed to calculate the amount of created electrons in the depleted substrate, which then can be compared to the measurement. For the depletion depth of approximately 24 μm about 2300 e^- are expected. The measurement yields a most probable value of 85 lsb, 114 lsb, and 117 lsb for the 50 μm , 100 μm and the unthinned sensor, respectively. This corresponds to a charge collection of 2750 e^- ,

4300 e^- and 4450 e^- for the three sensors estimated from the injection measurement, respectively. Hence, the 100 μm sensor collects about 55% and the unthinned sensor approximately 60% more charge than the 50 μm sensor. For the 50 μm sensor a higher value of collected electrons is measured, compared to the calculation. Here, it is possible, that the assumption of a minimum ionizing electron for the most probable value is underestimating the actual most probable charge deposition of ^{90}Sr . The additional charge collection can be compared to the estimation in the test beam for the 100 μm sensor. There, about 50% more charge is collected in comparison to the 50 μm sensor. Hence, the estimation yields similar results for the additional charge collection via diffusion.

Finally, the high bias voltage case of -130 V is evaluated in Figure 11.4. It displays the normalized ToT distributions of the 100 μm (red) and the unthinned (green) sensor. Here, the shoulder towards lower ToT values is even more pronounced than in the low bias voltage case. In comparison to Figure 8.7 where the two distributions are almost identical, the calibration enables the distinction of the two distributions and allows to detect a slight shift towards a larger most probable value for the thicker sensor. This indicates only a small impact of diffusion on the signal in the region of large signals which are dominated by the charge collection via drift.

Overall, the unthinned sensor shows a broader distribution (FWHM: 160 lsb) than the 100 μm sensor (FWHM: 128 lsb), which is caused by diffusion as well. As the 100 μm sensor is almost completely depleted at this bias voltage, the influence of diffusion on the signal is negligible compared to the unthinned sensor. The total amount of collected charge via diffusion varies from hit to hit. Therefore, the unthinned sensor has more variation in the collected charge, leading to a broader distribution.

Furthermore, the most probable value of the high bias voltage measurement is shifted to higher values in comparison to the low bias voltage case. For the bias voltage of -130 V , the unthinned sensor has its most probable value at approximately 4800 e^- . For the -15 V bias voltage case, it collects about 3900 e^- . However, the depletion depth is calculated to be about 70 μm deep. For a minimum ionizing electron, about 6700 e^- are expected to be collected by drift. It is known from the scan of the injection voltage for pixel 10/10, that at these charge depositions the amplifier is saturating rather strongly. Hence, the assumption of linearity in the relationship of ToT to collected charge is wrong at this point. This confirms the observation in the previous plot, as the shoulder towards lower ToT values is even more pronounced in the high bias voltage case. Therefore, the influence of diffusion is probably larger than visible in the distribution, as it is squeezed together by the saturation of the amplifier.

Hence, a second estimation of the collected electrons by utilizing the injection scan in Figure 11.2 is performed. The measurement yields most probable values of 141 lsb (100 μm) and 173 lsb (unthinned). This yields about 6400 e^- , which is close to the expected value of 6700 e^- . For the unthinned sensor, the charge collection is too large to allow a reliable gauging with the injection measurement. At this point, higher energetic x-ray sources are needed for the calibration.

Table 6 and Table 7 summarize the results obtained with the ^{90}Sr source. Here, "e $^{-}$ from drift" denotes the calculated mean charge collection from drift for a minimum ionizing electron for the depletion depth, "e $^{-}$ (^{55}Fe Calibration)" is the number of electrons obtained for the most probable value from the ^{55}Fe calibration and "e $^{-}$ (Injection Gauging)" is the estimation using the injection scan.

Chip Thickness	e $^{-}$ from drift	e $^{-}$ (^{55}Fe Calibration)	e $^{-}$ (Injection Gauging)
50 μm	2300	2750	2750
100 μm	2300	3650	4300
unthinned	2300	3750	4450

Table 6: Summary of the collected e $^{-}$ for the ^{90}Sr source for a bias voltage of -15 V.

Chip Thickness	e $^{-}$ from drift	e $^{-}$ (^{55}Fe Calibration)	e $^{-}$ (Injection Gauging)
100 μm	6700	3900	6400
unthinned	6700	4800	-

Table 7: Summary of the collected e $^{-}$ for the ^{90}Sr source for a bias voltage of -130 V.

In conclusion, the calibration enables a more precise characterization of the sensors in the low charge deposition case. Here, the calibration allowed for a distinction of the 100 μm and the unthinned sensor, indicating a modest additional charge collection for the unthinned sensor. This is in agreement with the previous measurement of the cluster size and the estimate of the Gaussian spread of a diffusing charged particle. In summary, for a bias voltage of -15 V the influence of diffusion on the signal is significant. It should be noted, that the 50 μm sensor has a small contribution by diffusion as well, as it is not entirely depleted at a bias voltage of -15 V. Hence, the starting saturation of the amplifier and the contribution of diffusion present in the 50 μm sensor both lead to an underestimation of the actual influence of diffusion. Yet, the measured signal is about 38% larger for the unthinned sensor. The calibration validates the observed difference in the uncalibrated case and ensures that the difference is not emerging from the sensor-to-sensor variations.

Moreover, a saturation effect of the amplifier is observed in the test beam data, where the amount of collected electrons extrapolated from the ^{55}Fe source is significantly less than the calculated average amount expected for the depletion depth. This is validated by a scan of the injection voltage, where the ToT response displays an approximately logarithmic behavior.

The injection scan is used to give a second estimate of the amount of collected electrons, considering the non-linearity of the amplifier. Here, an even larger influence of diffusion on the signal generation is measured. For the 100 μm sensor about 50% more charge is collected for the ^{90}Sr source and 4 GeV, compared to the 50 μm

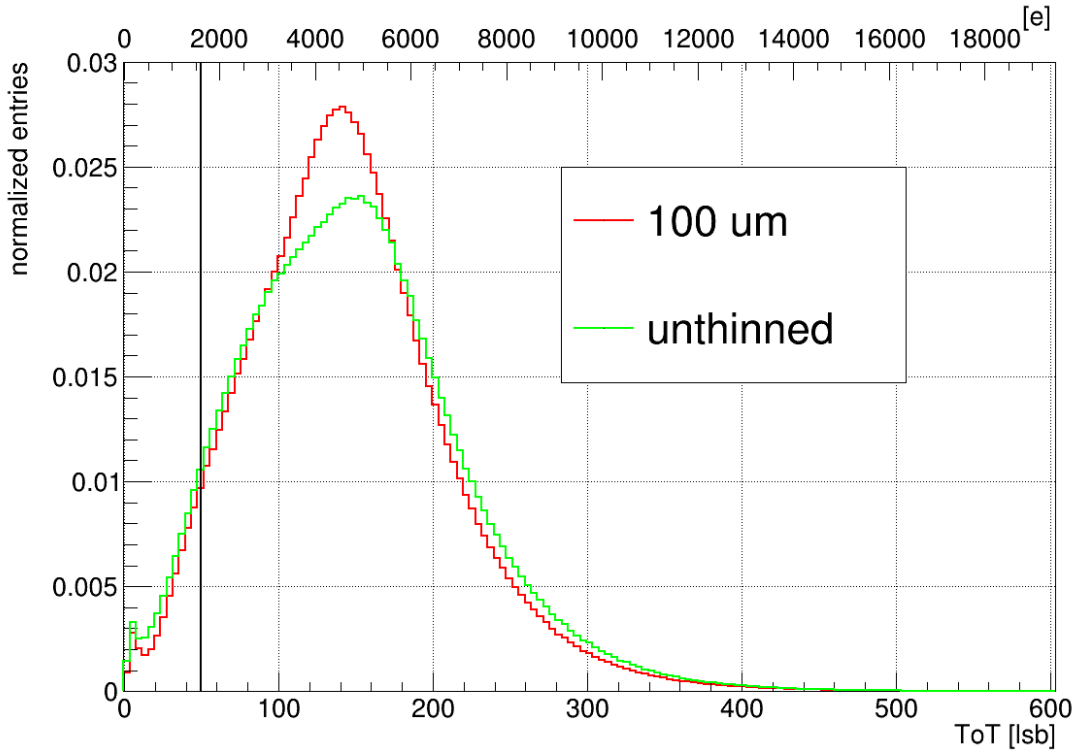


Figure 11.4: Calibrated ToT for the ^{90}Sr source for the $100\ \mu\text{m}$ (red) and the unthinned (green) sensor with an applied bias voltage of $-130\ \text{V}$.

sensor. For the unthinned sensor 60% more charge is collected, compared to the $50\ \mu\text{m}$ sensor.

Furthermore, for a bias voltage of $-130\ \text{V}$ the calibration indicates only a minor effect of diffusion on the overall signal. This is concluded, as the most probable value is slightly shifted and the distribution is broader for the unthinned sensor. However, the amplifier is heavily saturated in the high bias voltage case, as the expected number of electrons collected via drift for a minimum ionizing electron is about $6700\ e^-$. Hence the linearity between ToT and collected charge which is assumed in the calibration is broken. This also explains the shoulder towards lower ToT values which are introduced by an overcorrection of the ToT.

IV Discussion

12 Summary & Conclusion

Within this thesis, the impact of the collected charge on the signal generation of HV-MAPS is investigated. A crucial point is the differentiation of contributions from the depletion volume, where the charge is rapidly collected via drift, and contributions from the undepleted volume. For the latter, the charge is undergoing diffusion first and can then be collected in the depleted volume as well. The small scale R&D sensor Run2021v2 with in-pixel CMOS amplifier and comparator is chosen to investigate this phenomenon. To facilitate this study, several signal sources are used to study sensors of different thickness at the same configuration. Two different bias voltages are evaluated, -15 V and -130 V . For the former one, the undepleted substrate (and hence the diffusive component of the signal) is negligible in the $50\text{ }\mu\text{m}$ sensor, while for the latter it is negligible for the $100\text{ }\mu\text{m}$ sensor.

First, a study of the IV-curve of the guard rings is performed for a sensor with a substrate resistivity of $(370 \pm 20)\text{ }\Omega\text{ cm}$ in section 7. The chip guard ring shows a higher breakdown voltage for the diode, enabling a bias voltage of up to -143.6 V , while the breakdown for the pixel guard ring is reached at about -87.2 V on the investigated sensor. A measurement of the voltage on the pixel guard ring while applying the voltage on the chip guard ring, reveals a divergence of the two voltages. At the breakdown voltage of -143.6 V the voltage on the pixel guard ring is measured to be -88.5 V . Therefore, it is concluded that the breakdown still happens on the pixel guard ring. Furthermore, a study of the influence of the guard ring on the ToT distribution is performed. Here, the bias voltage is once applied through the pixel guard ring (-40 V) and once through the chip guard ring (-48.9 V), where in both cases the applied voltage on the pixel guard ring is -40 V . Here, the ToT distribution is shifted to larger entries for the biasing through the chip guard ring. Therefore, it is concluded that the higher bias voltage on the chip guard ring allows for a deeper depletion while having similar lateral depletion.

In section 8 the study of diffusion is performed. The cluster size and ToT are investigated for three sensors of different thickness at the same settings and applied bias voltage. Electrons from a ^{90}Sr source and 4 GeV electrons, obtained in a test beam at DESY, are used as a signal source. An increased average cluster size is observed for the thicker sensors for both signal sources. Here, for the ^{90}Sr source average cluster sizes of 1.21 ($50\text{ }\mu\text{m}$), 1.57 ($100\text{ }\mu\text{m}$) and 1.69 (unthinned) are measured for a bias voltage of -15 V . In the case of a high bias voltage of -130 V , an average cluster size of 1.95 ($100\text{ }\mu\text{m}$) and 2.42 (unthinned) is determined. This observation is explained by the additional charge collection via diffusion. Here, a diffusion of charge carriers in the undepleted substrate into neighboring pixels increases the cluster size. This effect is enhanced by the very small pixel pitch of only $25\text{ }\mu\text{m}$ in row direction for the Run2021v2 sensor. Moreover, for a cluster size of 2, the time difference between the seed pixel and the secondary hit in the cluster is evaluated for the test beam data. Here, more clusters occurred with a delay for the $100\text{ }\mu\text{m}$ sensor than for the $50\text{ }\mu\text{m}$ sensor. As the charge collection via diffusion is a comparable slow process, this supports the explanation.

For the study of the ToT values in subsection 8.2, the distribution of the $100\text{ }\mu\text{m}$ sensor (MPV for 4 GeV electrons: 115 lsb) is significantly shifted towards larger values compared to the $50\text{ }\mu\text{m}$ sensor (MPV for 4 GeV electrons: 69 lsb) for both signal sources. Moreover, no observable difference between the $100\text{ }\mu\text{m}$ and the unthinned

sensor is measured in all studied cases. However, sensor-to-sensor variations are observed in the ToT distributions of sensors of the same thickness. These variations add an uncertainty in the evaluation of the impact of diffusion on the signal generation, necessitating a calibration. The influence of the variations on the cluster size is evaluated as well. Here, only small variations are observed and it is concluded, that the cluster size is a reliable observable to quantify diffusion.

The calibration is implemented in the Corryvreckan framework [38]. A ToT analysis module, the so-called "ToTAnalyzer", is utilized for a detailed statistical analysis of the ToT distributions of the individual pixels (see section 9). This enables a new insight on the functionality of the sensor, as e.g. pixel-to-pixel variations can be quantified. In addition, a random pixel is chosen to calculate the single pixel energy resolution after the entire readout and analysis. Here, for a bias voltage of -15 V an energy resolution $\frac{\sigma_E}{E}$ of $(15.23 \pm 0.13)\%$ is calculated, while for the bias voltage of -130 V a resolution of $(13.09 \pm 0.12)\%$ is obtained. This resolution contains the contribution of noise, the uncertainty arising from the Fano factor [45] and the uncertainties from the readout elements.

Furthermore, the module is used to evaluate the correlation between FWHM and median of the ToT distribution of each pixel. Although most of the pixels have a comparable response, there is a significant number of outliers with very large FWHM and median in Figure 9.11. This observation confirmed the assumption, that the discrepancies between sensors arise from pixel-to-pixel variations.

By comparing the median distributions for -15 V and -130 V , a shift towards larger signals is observed for the high bias voltage case. This is caused by the diminishing capacitance of the diode in the high bias voltage case, which influences the pulse shaping. Consequently, the calibration has to be performed separately for each bias voltage and sensor.

Next, the ToTCalibration module is introduced and a quality control is conducted in section 10. The module uses a linear scaling approach to calibrate the ToT of a sensor. Here, an ^{55}Fe data set with about 10 000 entries per pixel is used to calibrate the median ToT response of each pixel to the same ToT value. The median and FWHM distribution after calibration are investigated in the correlation plot of these two quantities. An alignment of the median within (50 ± 2) lsb is observed, while for the FWHM a majority of the pixels have similar pulse widths of (18 ± 5) lsb. Nevertheless, the FWHM also has a sizable amount of outliers, which are corresponding to pixels with large pulse widths. This is expected from the shape of the correlation before calibration, as the FWHM and median are only limited linearly related.

For three unthinned sensors, an alignment of the most probable value to the same bin is achieved by the calibration. However, the FWHM is observed to be 116 lsb, 124 lsb and 128 lsb wide. Hence, for the further analysis it is concluded, that the most probable value can be used to precisely quantify diffusion, while **slight** deviations in the FWHM and tails of the distribution might still arise from sensor-to-sensor variations after calibration.

A brief study of the functionality of the injection circuit is presented. For this, a sample of 100 pixels is injected with a voltage of 300 mV, which is close to the signal of the ^{55}Fe source. The signal is again evaluated on a pixel-to-pixel basis, revealing a Gaussian form for a single pixel. However, the ToT spectrum of the combination of these pixels is observed to be very distorted with multiple peaks (see

Figure 10.6). After the calibration, using the ^{55}Fe signal, again a Gaussian shape with comparable FWHM to the single pixel one is obtained. It is concluded, that the variation visible in the uncalibrated spectrum is dominated by a variation of the amplifier and not by varying injection capacitances. Nevertheless, also a small variation of injection capacitances is observed, as the FWHM after the calibration deteriorates more from the single pixel one for the injection measurement, than for the ^{55}Fe measurement. This variation is caused by process variations in the manufacturing. In conclusion, the calibration is found to yield promising results in the small signal region.

In a next step, the diffusion studies are continued with the aid of the calibration. For a bias voltage of -15 V a significant influence of diffusion on the signal is measured for the 4 GeV electron beam as well as for the ^{90}Sr source. For the ^{90}Sr source a shoulder towards lower ToT values emerges in the spectra of the $100\text{ }\mu\text{m}$ and the unthinned sensor. It is concluded, that this excess in entries is caused by an over correction of the large energy depositions, where the ToT response saturates.

In an injection scan for a single pixel, a saturation effect for the amplifier is observed. The measurement indicates a deviation from linearity at about 2200 electrons. As the assumption of linearity for the ^{55}Fe calibration underestimates the amount of collected charge, the injection scan is utilized to give a more realistic estimate. Here, about 50% more charge is collected for the $100\text{ }\mu\text{m}$ sensor and about 60% more charge is collected for the unthinned sensor in comparison to the $50\text{ }\mu\text{m}$ sensor, respectively.

Finally, for the bias voltage of -130 V a slight shift of the most probable value towards larger ToT values is observed for the unthinned sensor compared to the $100\text{ }\mu\text{m}$ sensor. Additionally, the unthinned sensor exhibited a 25% broader FWHM. These two observations are related to diffusion. However, the strong saturation of the amplifier for the example pixel in the injection scan, suggests that the linear calibration approach is not valid for these substantial charge collections. This is also visible in the pronounced shoulders towards lower ToT, which are caused by an over correction of the saturating ToT. At this bias voltage, the charge collection via drift is immense, as approximately 6700 e^- are collected for a minimum ionizing electron. Hence, a smaller impact of diffusion on the signal is expected, which is in line with the observation.

In conclusion, for a bias voltage of -15 V , a significant impact of diffusion on the signal generation is measured. Both observables, the cluster size and the ToT distribution, are about 30% larger in case of the ^{90}Sr source for the unthinned sensor compared to the $50\text{ }\mu\text{m}$ sensor. For the calibration with the injection scan, which takes the saturation of the amplifier into account, even about 50% more collected charge is observed. The experimental data shows, that diffusion is not negligible in these small signal regions, if undepleted substrate is present. Furthermore, for a bias voltage of -130 V , only a small amount of additional charge is measured in the ToT distribution of the unthinned sensor compared to the $100\text{ }\mu\text{m}$ sensor after calibration. Nevertheless, for the cluster size a sizable difference is observed for this bias voltage. Hence, diffusion also impacts the signal formation at these high bias voltages in a measurable manner.

13 Outlook

Within this thesis, compelling experimental proof for the significance of diffusion on the signal generation of an HV-MAPS is given. These results should be complemented by a simulation, e.g. in Allpix Squared [47]. This is be a valuable input to understand if the measured difference is arising solely by diffusion or if other, currently unknown, phenomena play a role as well.

The detailed analysis and calibration on a per pixel basis is so far only performed for the small scale Run2021v2 sensor. It would be interesting to apply the calibration to a full scale sensor like the MuPix11 and investigate if a comparable improvement of the ToT dispersion can be achieved for a sensor with approximately a factor 20 more pixels.

At a bias voltage of -130 V a limitation of the calibration is observed, as the amplifier starts to saturate and a non-linearity between ToT and energy arises. A solution to this issue is a calibration using a more energetic x-ray source. Here, the approximately logarithmic behavior observed in Figure 11.2 has to be fitted for every pixel. The parameters of the fit function are then used to calibrate the non-linearity of the pixel for large signals. Combined with the information of the ^{55}Fe source, a precise calibration of the deposited energy can be achieved by this method. Moreover, this task can be carried out in the framework presented in this thesis. The only missing step is the fitting of the functions on a per pixel basis.

In addition, the analysis on the pixel level reveals a new phenomenon. Here, a tail which emerges towards large ToT values for bias voltages above -100 V in the ^{55}Fe signal is measured. This is interpreted to be caused by regions of very high electric field, where secondary ionization is possible. This phenomenon is only treated peripherally, yet deserves a dedicated investigation and characterization.

V Appendix

A DAC Values

DAC	Value [hex]	DAC	Value [hex]
VNPix	14	VPDelDclMux	20
VNFBPix	14	VNDelDclMux	20
VNFollPix	2	VPDelDcl	20
VNPix2	0	VNDelDcl	20
VNBiasPix	0	VPDelPreEmp	20
VPLoadPix	2	VNDelPreEm	20
VNCompPix	a	VPDcl	18
VNCompFine	a	VNDcl	c
VNDel	d	VNLVDS	2f
VPBigFine	8	VNLVDSDel	0
VPDAC	0	VPPump	14
VPSmallFine	13	ckdivend (2)	0
VNDAC	0	timerend	1
VPBiasRec	6	slowdownend	7
VNBiasRec	5	maxcycend	f
invert	0	resetckdivend	f
selEx	0	sendcounter	0
selSlow	0	ckdivend3	0
enPLL	1	count sheep	0
selFast	0	Bandgap on	0
VPVCO	14	BiasBlock on	5
VNVCO	20	VPFoll	14
VNVCO	20	VPFoll	14

Table 9: DAC settings.

B ToTAnalyzer Maps

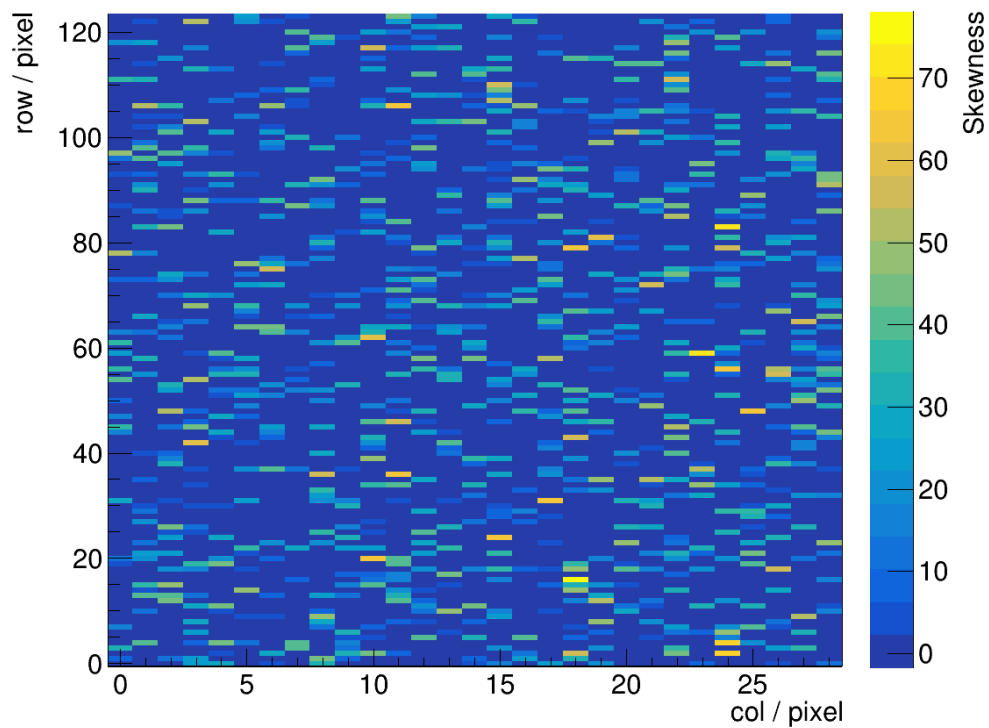


Figure B.1: Map of the single pixel ToT skewness for ^{55}Fe at a bias voltage of -15 V .

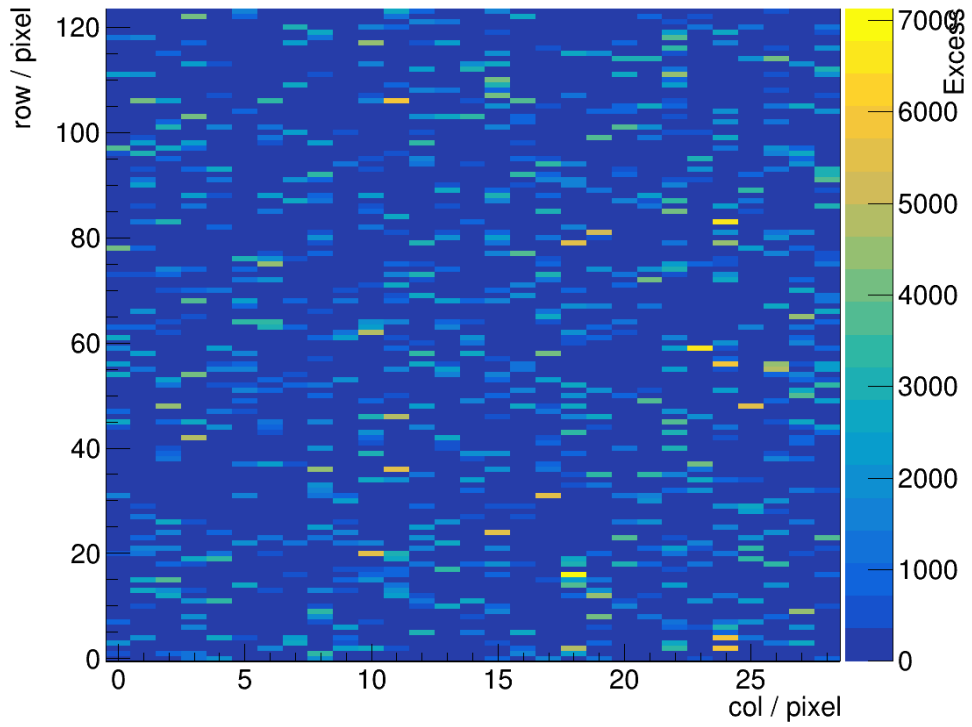


Figure B.2: Map of the single pixel ToT excess kurtosis for ^{55}Fe at a bias voltage of -15 V .

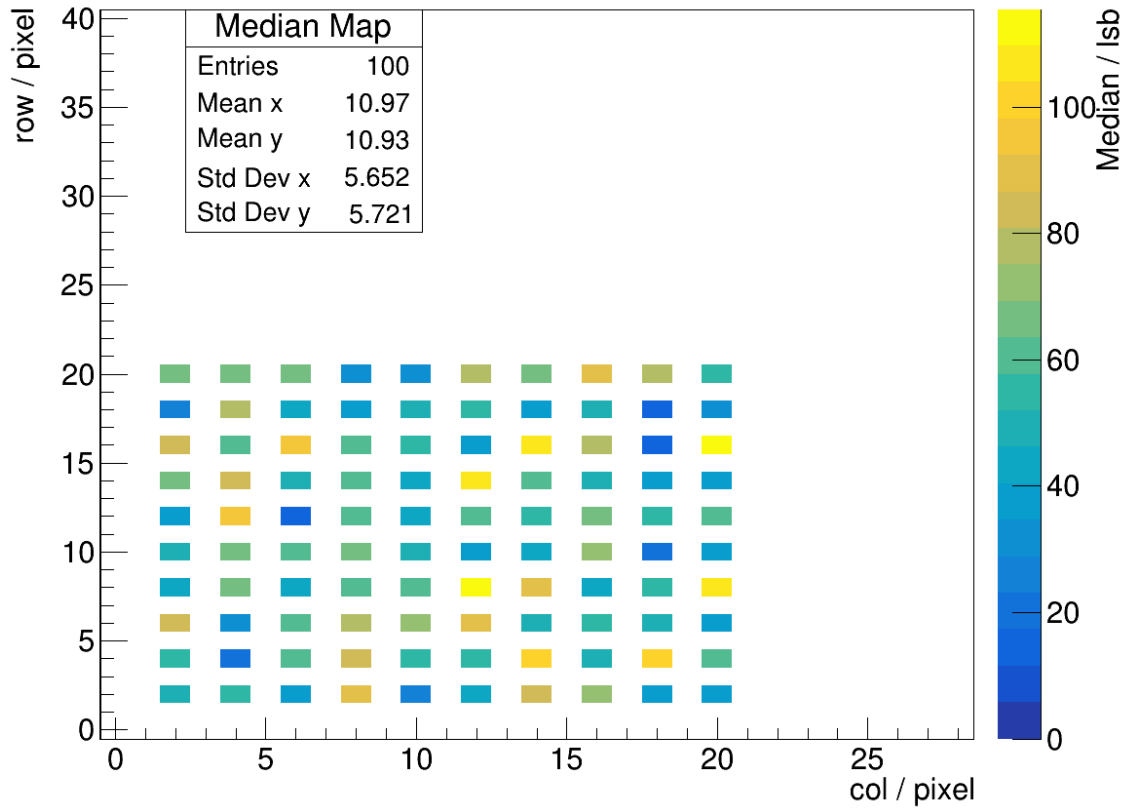


Figure B.3: Map of the single pixel ToT median for an Injection voltage of 300 mV .

A Bibliography

- [1] W. Bertl et al. “Search for the decay $\mu^+ \rightarrow e^+ + e^+ + e^-$ ”. In: *Nuclear Physics B* 260.1 (1985), pp. 1–31. ISSN: 0550-3213. DOI: [https://doi.org/10.1016/0550-3213\(85\)90308-6](https://doi.org/10.1016/0550-3213(85)90308-6). URL: <https://www.sciencedirect.com/science/article/pii/0550321385903086>.
- [2] Patrick Blackstone, Matteo Fael, and Emilie Passemar. “ $\tau \rightarrow \mu\mu\mu$ at a rate of one out of 10^{14} tau decays?” In: *The European Physical Journal C* 80.6 (June 2020). DOI: 10.1140/epjc/s10052-020-8059-7. URL: <https://doi.org/10.1140/epjc/s10052-020-8059-7>.
- [3] Heiko Augustin et al. “TelePix – A fast region of interest trigger and timing layer for the EUDET Telescopes”. In: *Nuclear Instruments and Methods in Physics Research Section A: Accelerators, Spectrometers, Detectors and Associated Equipment* 1048 (Mar. 2023), p. 167947. DOI: 10.1016/j.nima.2022.167947. URL: <https://doi.org/10.1016/j.nima.2022.167947>.
- [4] Hermann Kolanoski and Norbert Wermes. *Teilchendetektoren. Grundlagen und Anwendungen*. ger. 1. Aufl. 2016. Springer eBook Collection. Berlin ; Heidelberg: Springer Spektrum, 2016, Online-Ressource (XVI, 921 S. 550 Abb., 429 Abb. in Farbe, online resource). ISBN: 978-3-662-45350-6. DOI: 10.1007/978-3-662-45350-6. URL: <http://dx.doi.org/10.1007/978-3-662-45350-6>.
- [5] M. Tanabashi et al. “Review of Particle Physics”. In: *Phys. Rev. D* 98 (3 Aug. 2018), p. 030001. DOI: 10.1103/PhysRevD.98.030001. URL: <https://link.aps.org/doi/10.1103/PhysRevD.98.030001>.
- [6] Stephen M. Seltzer and Martin J. Berger. “Improved procedure for calculating the collision stopping power of elements and compounds for electrons and positrons”. In: *The International Journal of Applied Radiation and Isotopes* 35.7 (1984), pp. 665–676. ISSN: 0020-708X. DOI: [https://doi.org/10.1016/0020-708X\(84\)90113-3](https://doi.org/10.1016/0020-708X(84)90113-3). URL: <https://www.sciencedirect.com/science/article/pii/0020708X84901133>.
- [7] Heiko Augustin. “Development of a novel slow control interface and suppression of signal line crosstalk enabling HV-MAPS as sensor technology for Mu3e”. PhD thesis. University of Heidelberg, 2021.
- [8] E. J. Schioppa et al. “Study of Charge Diffusion in a Silicon Detector Using an Energy Sensitive Pixel Readout Chip”. In: *IEEE Transactions on Nuclear Science* 62.5 (2015), pp. 2349–2359. DOI: 10.1109/TNS.2015.2475124.
- [9] E. Gaubas and Jan Vanhellemont. “Comparative Study of Carrier Lifetime Dependence on Dopant Concentration in Silicon and Germanium”. In: *Journal of the Electrochemical Society* 154 (Jan. 2007), H231–H238. DOI: 10.1149/1.2429031.

- [10] Jakob Sticker. “Testing of a Method for the Sensor Thickness Determination and a Cluster Size Study for the MuPix10”. Bachelor Thesis. University of Heidelberg, 2021.
- [11] Simon Ramo. “Currents induced by electron motion”. In: *Proc. Ire.* 27 (1939), pp. 584–585. DOI: 10.1109/JRPROC.1939.228757.
- [12] C. Canali et al. “Electron and hole drift velocity measurements in silicon and their empirical relation to electric field and temperature”. In: *IEEE Transactions on Electron Devices* 22.11 (1975), pp. 1045–1047. DOI: 10.1109/T-ED.1975.18267.
- [13] Annie Meneses Gonzales. “TCAD Simulations and Characterization of High-Voltage Monolithic Active Pixel Sensors”. PhD thesis. University of Heidelberg, 2023.
- [14] George Domingo. *Semiconductor Basics*. eng. 1st edition. Online resource; Title from title page (viewed September 8, 2020). [Erscheinungsort nicht ermittelbar]: Wiley, 2020, 1 online resource (320 pages). ISBN: 978-1-119-70230-6. URL: <https://learning.oreilly.com/library/view/-/9781119702306/?ar>.
- [15] Phillip E. Allen and Douglas R. Holberg. *CMOS analog circuit design*. eng. International third edition. New York ; Oxford: Oxford University Press, 2012, xv, 590 Seiten. ISBN: 978-0-19-993742-4.
- [16] Arjuna Marzuki. *CMOS analog and mixed-signal circuit design. practices and innovations*. eng. First edition. Includes bibliographical references and index. - Online resource; title from digital title page (viewed on June 24, 2020). Boca Raton, FL: CRC Press, 2020, 1 online resource (xv, 270 pages). URL: <https://learning.oreilly.com/library/view/-/9781000071511/?ar>.
- [17] Jorgen Christiansen. “RD53B users guide: Introduction to RD53B pixel chip architecture, features and recommendations for use in pixel detector systems.” In: (May 2021).
- [18] M. Mager. “ALPIDE, the Monolithic Active Pixel Sensor for the ALICE ITS upgrade”. In: *Nuclear Instruments and Methods in Physics Research Section A: Accelerators, Spectrometers, Detectors and Associated Equipment* 824 (2016). Frontier Detectors for Frontier Physics: Proceedings of the 13th Pisa Meeting on Advanced Detectors, pp. 434–438. ISSN: 0168-9002. DOI: <https://doi.org/10.1016/j.nima.2015.09.057>. URL: <https://www.sciencedirect.com/science/article/pii/S0168900215011122>.
- [19] Chenfei Yang et al. “A Prototype Readout System for the ALPIDE Pixel Sensor”. In: *IEEE Transactions on Nuclear Science* 66.7 (2019), pp. 1088–1094. DOI: 10.1109/TNS.2019.2913335.
- [20] Heiko Augustin et al. *MuPix10: First Results from the Final Design*. 2020. arXiv: 2012.05868 [physics.ins-det].
- [21] Luigi Vigani. *Mupix: Monolithic sensors for the Mu3e experiment*. Proceedings in preparation.
- [22] Ivan Perić. “A novel monolithic pixelated particle detector implemented in high-voltage CMOS technology”. In: *Nuclear Instruments and Methods in Physics Research Section A: Accelerators, Spectrometers, Detectors and Associated Equipment* 582.3 (2007), pp. 876–885.

- [23] K. Arndt et al. “Technical design of the phase I Mu3e experiment”. In: *Nuclear Instruments and Methods in Physics Research Section A: Accelerators, Spectrometers, Detectors and Associated Equipment* 1014 (Oct. 2021), p. 165679. DOI: 10.1016/j.nima.2021.165679. URL: <https://doi.org/10.1016%2Fj.nima.2021.165679>.
- [24] Ivan Peric. “TSI engineering run HVMAPS”. unpublished.
- [25] R. Diener et al. “The DESY II test beam facility”. In: *Nuclear Instruments and Methods in Physics Research Section A: Accelerators, Spectrometers, Detectors and Associated Equipment* 922 (2019), pp. 265–286. ISSN: 0168-9002. DOI: <https://doi.org/10.1016/j.nima.2018.11.133>. URL: <https://www.sciencedirect.com/science/article/pii/S0168900218317868>.
- [26] Dirk Wiedner. *The Mupix8 PCB*. Mu3e Internal Note 42.
- [27] Altera Corporation. *Stratix® IV Device Handbook*. Jan. 2016. URL: <https://www.intel.com/content/www/us/en/content-details/654799/stratix-iv-device-handbook.html>.
- [28] Adrian Herkert. “Characterization of a Monolithic Pixel Sensor Prototype in HV-CMOS Technology for the High-Luminosity LHC”. PhD thesis. U. Heidelberg (main), 2020. DOI: 10.11588/heidok.00027893.
- [29] David M. Immig. “The Very Large HV-MAPS Tracking Telescope”. BTTB 9. 2021. URL: https://indico.cern.ch/event/945675/contributions/4184873/attachments/2186614/3694678/bttb9_immig.pdf.
- [30] Yi Liu et al. *ADENIUM – A demonstrator for a next-generation beam telescope at DESY*. Jan. 2023. DOI: 10.48550/arXiv.2301.05909.
- [31] H. Augustin et al. “Upgrading the beam telescopes at the DESY II Test Beam Facility”. In: *Nuclear Instruments and Methods in Physics Research Section A: Accelerators, Spectrometers, Detectors and Associated Equipment* 1040 (Oct. 2022), p. 167183. DOI: 10.1016/j.nima.2022.167183. URL: <https://doi.org/10.1016%2Fj.nima.2022.167183>.
- [32] G. Audi et al. “The Nubase evaluation of nuclear and decay properties”. In: *Nuclear Physics A* 729.1 (2003). The 2003 NUBASE and Atomic Mass Evaluations, p. 39. ISSN: 0375-9474. DOI: <https://doi.org/10.1016/j.nuclphysa.2003.11.001>. URL: <https://www.sciencedirect.com/science/article/pii/S0375947403018074>.
- [33] From ENSDF database as of Juni 18, 2023. Version available at <http://www.nndc.bnl.gov/ensarchivals/>. URL: <https://www.nndc.bnl.gov/nudat3/DecayRadiationServlet?nuc=90Sr&unc=NDS>.
- [34] From ENSDF database as of Juni 18, 2023. Version available at <http://www.nndc.bnl.gov/ensarchivals/>. URL: <https://www.nndc.bnl.gov/nudat3/DecayRadiationServlet?nuc=90Y&unc=NDS>.
- [35] Jefferson Dixon et al. “Evaluation of a silicon 90Sr betavoltaic power source”. In: *Scientific reports* 6.1 (2016), p. 38182.
- [36] From ENSDF database as of Juni 18, 2023. Version available at <http://www.nndc.bnl.gov/ensarchivals/>. URL: <https://www.nndc.bnl.gov/nudat3/DecayRadiationServlet?nuc=55Fe&unc=NDS>.

- [37] Inc. Virginia Semiconductor. *Resistivity and Carrier Transport Parameters in Silicon*. URL: <https://www.virginiasemi.com/pdf/ResistivityCarrierTransportinSilicon.pdf>.
- [38] D. Dannheim et al. “Corryvreckan: a modular 4D track reconstruction and analysis software for test beam data”. In: *Journal of Instrumentation* 16.03 (Mar. 2021), P03008. DOI: 10.1088/1748-0221/16/03/P03008. URL: <https://dx.doi.org/10.1088/1748-0221/16/03/P03008>.
- [39] Heiko Augustin. personal communication.
- [40] Wikimedia Commons. *Mean*. [Online; accessed 25-June, 2023]. URL: https://en.wikipedia.org/wiki/Mean#/media/File:Comparison_mean_median_mode.svg.
- [41] G. Bohm and G. Zech. *Introduction to statistics and data analysis for physicists*. DESY, 2010. ISBN: 9783935702416. URL: http://www-library.desy.de/preparch/books/vstatmp_engl.pdf.
- [42] Rene Brun and Fons Rademakers. *ROOT - An Object Oriented Data Analysis Framework*. Version 6.27/01. 1997.
- [43] B.G. Lowe and R.A. Sareen. “A measurement of the electron–hole pair creation energy and the Fano factor in silicon for 5.9keV X-rays and their temperature dependence in the range 80–270K”. In: *Nuclear Instruments and Methods in Physics Research Section A: Accelerators, Spectrometers, Detectors and Associated Equipment* 576.2 (2007), pp. 367–370. ISSN: 0168-9002. DOI: <https://doi.org/10.1016/j.nima.2007.03.020>. URL: <https://www.sciencedirect.com/science/article/pii/S016890020700527X>.
- [44] M.N. Mazziotta. “Electron–hole pair creation energy and Fano factor temperature dependence in silicon”. In: *Nuclear Instruments and Methods in Physics Research Section A: Accelerators, Spectrometers, Detectors and Associated Equipment* 584.2 (2008), pp. 436–439. ISSN: 0168-9002. DOI: <https://doi.org/10.1016/j.nima.2007.10.043>. URL: <https://www.sciencedirect.com/science/article/pii/S0168900207022668>.
- [45] U. Fano. “Ionization Yield of Radiations. II. The Fluctuations of the Number of Ions”. In: *Phys. Rev.* 72 (1 July 1947), pp. 26–29. DOI: 10.1103/PhysRev.72.26. URL: <https://link.aps.org/doi/10.1103/PhysRev.72.26>.
- [46] L M P Fernandes et al. “Characterization of large area avalanche photodiodes in X-ray and VUV-light detection”. In: *Journal of Instrumentation* 2.08 (Aug. 2007), P08005–P08005. DOI: 10.1088/1748-0221/2/08/p08005. URL: <https://doi.org/10.1088/1748-0221/2/08/p08005>.
- [47] S. Spannagel et al. “Allpix2: A modular simulation framework for silicon detectors”. In: *Nuclear Instruments and Methods in Physics Research Section A: Accelerators, Spectrometers, Detectors and Associated Equipment* 901 (2018), pp. 164–172. ISSN: 0168-9002. DOI: <https://doi.org/10.1016/j.nima.2018.06.020>. URL: <https://www.sciencedirect.com/science/article/pii/S0168900218307411>.

Erklärung:

Ich versichere, dass ich diese Arbeit selbstständig verfasst habe und keine anderen als die angegebenen Quellen und Hilfsmittel benutzt habe.

Heidelberg, den 24.07.2023

A handwritten signature in black ink, appearing to read 'R. Kolb', written in a cursive style. The signature is positioned above a horizontal dotted line.

Acknowledgements

First of all, I would like to thank Prof. André Schöning, who gave me the opportunity to work on this interesting topic.

I would also like to thank Prof. Norbert Herrmann for his quick commitment as my second examiner on short notice.

Big thanks to Heiko Augustin, for supervising me, patiently answering all my questions and the guidance during this thesis.

Thanks to David for explaining the hardware and software and for insisting on proper coding.

I am deeply grateful to all proof readers of my thesis: Benni, David, Heiko, Lukas, Sebastian, Tamasi and Thomas.

Many thanks to all of the Mu3e and Atlas group members for the pleasant working environment and enjoyable lunch breaks.

Lastly I would like to thank my family and girlfriend, who encouraged me to start my study and supported me throughout the years.